

Die approbierte Originalversion dieser Dissertation ist an der Hauptbibliothek der Technischen Universität Wien aufgestellt (<http://www.ub.tuwien.ac.at>).

The approved original version of this thesis is available at the main library of the Vienna University of Technology (<http://www.ub.tuwien.ac.at/englweb/>).

DISSERTATION

Deterministic Numerical Solution of the Boltzmann Transport Equation

ausgeführt zum Zwecke der Erlangung des akademischen Grades
eines Doktors der technischen Wissenschaften

eingereicht an der Technischen Universität Wien
Fakultät für Elektrotechnik und Informationstechnik
von

KARL RUPP

Linke Bahnzeile 7/6
A-2486 Pottendorf-Landegg, Österreich

Matr. Nr. 0325941
geboren am 12. Juni 1984 in Bad Radkersburg

Wien, im Dezember 2011

*To Antonia, Thomas, Hubert and Dieter.
Rest in peace.*

Kurzfassung

Die kleinen Abmessungen moderner Halbleiterbauelemente machen eine direkte Messung von Ladungstransportdetails unmöglich. Eine präzise Simulation des Ladungsträgertransports im Inneren des Bauelements ist daher für das Verstehen der physikalischen Vorgänge und für weitere Effizienzsteigerungen unerlässlich. Für diesen Zweck ist das Drift-Diffusionsmodell lange das Zugpferd der Halbleitersimulation gewesen, allerdings verliert es durch die voranschreitende Miniaturisierung und der einhergehenden Reduktion der Streuung von Ladungsträgern am Kristallgitter oder anderen Ladungsträgern seine Gültigkeit.

Der genannte Genauigkeitsverlust kann durch eine Lösung der Boltzmannschen Transportgleichung anstelle der von ihr abgeleiteten vereinfachten Transportmodelle kompensiert werden, solange Quanteneffekte hinreichend klein sind. Die Hochdimensionalität der Boltzmannschen Transportgleichung macht eine direkte numerische Lösung jedoch sehr diffizil. Aus diesem Grund hat sich die stochastische Monte Carlo Methode etabliert, die die Berücksichtigung vieler Details erlaubt, aber zu langen Rechenzeiten führt und andere Nachteile mit sich bringt, welche in dieser Form bei makroskopischen Transportmodellen nicht auftreten. Der im Rahmen dieser Arbeit behandelte deterministische numerische Lösungsansatz mittels einer Entwicklung in harmonische Kugelflächenfunktionen leidet nicht unter den Nachteilen der Monte Carlo Methode, gleichzeitig kann aber eine praktisch gleiche Genauigkeit erreicht werden.

Im Laufe dieser Arbeit werden weitere Verbesserungen der Methode der Entwicklung in harmonische Kugelflächenfunktionen vorgeschlagen. Zuerst wird eine Erweiterung auf Streuungen zwischen Ladungsträgern präsentiert, die auch für höhere Entwicklungsgrade arbeitet. Danach wird die Struktur der resultierenden Gleichungen untersucht und eine Methode zur effizienten Speicherung der Systemmatrix vorgestellt. Im Anschluss werden Erweiterungen auf unstrukturierte Gitter unter der Verwendung beliebiger Entwicklungsgrade vorgeschlagen. Um den Rechenaufwand klein zu halten, werden variable Entwicklungsgrade und adaptive Kontrollstrategien eingeführt. Dem Trend hin zu parallelen Rechenarchitekturen wird durch die Vorstellung eines Schemas für das parallele Vorkonditionieren der Systemmatrix Rechnung getragen. Die Kombination der vorgestellten Techniken ermöglicht die erstmalige dreidimensionale Simulation eines Feldeffekttransistors mit Hilfe der Methode der Entwicklung in harmonische Kugelflächenfunktionen. Summa summarum erlauben die vorgeschlagenen Verbesserungen eine Reduktion des Speicherbedarfs um eine Größenordnung und der Ausführzeiten um zwei Größenordnungen.

Abstract

A direct measurement of the details of charge transport in semiconductor devices is impossible due to the small characteristic lengths of semiconductor devices. Therefore, accurate simulations are essential for understanding the physical effects inside the device and for further improvements of device performance. While the drift-diffusion model has long been the workhorse of semiconductor device simulation, the ongoing miniaturization implies that carrier transport through the device is no longer dominated by scattering with the crystal lattice or other carriers, which invalidates the model.

The loss in accuracy can be compensated by a numerical solution of the Boltzmann transport equation instead of simplified transport models derived from its moments, provided that quantum mechanical effects are sufficiently small. However, the high dimensionality of the Boltzmann transport equation makes direct numerical solutions very difficult. Consequently, the most commonly used method is the stochastic Monte Carlo method, which allows for the inclusion of many details. However, the method leads to excessive execution times and other problems, which are absent in macroscopic transport models. The deterministic numerical solution approach based on spherical harmonics expansions considered throughout this thesis does not suffer from the disadvantages of the Monte Carlo method, yet it provides virtually the same accuracy.

Further improvements of the spherical harmonics expansion methods are proposed in this work. First, a method for the inclusion of carrier-carrier scattering at arbitrary expansion orders is proposed. Then, the structure of the resulting equations is analyzed and a scheme for the efficient storage of the resulting system matrix is proposed. The method is then extended to unstructured grids at arbitrary expansion order. Variable-order expansions and adaptive schemes are proposed in order to keep computational costs under control. Moreover, the trend towards parallel computing architectures is addressed by the development of a parallel preconditioner scheme. With the combination of the presented schemes it is shown for the first time that the simulation of truly three-dimensional field-effect transistors using the spherical harmonics expansion method is feasible. Overall, the improvements suggested in this thesis lead to a reduction of memory requirements by one order of magnitude and execution times by two orders of magnitude.

Preface and Acknowledgement

This thesis summarizes my contributions to the enhancement of the spherical harmonics expansion (SHE) method developed during my doctoral studies. While microelectronics is at the heart of this thesis, it also touches on a number of related scientific fields: On the one hand, the ubiquitous solid-state physics provides the framework for all investigations of carrier transport in semiconductors, while on the other hand rather pure mathematics provides approximation results for the expansion of a function into spherical harmonics. In between, a considerable amount of scientific computing is also covered using the toolbox of modern programming paradigms. The latter is beyond the scope of this work and not further discussed, even though I consider it as one of the keys for extending the SHE method to three spatial dimensions.

The last three years consisted of a number of key events. I wish to reflect them in the following in order to also document the timeline that has led to the hard scientific facts discussed in the remainder of this work. A discussion of whether luck, fate or something else was the main trigger for each of these events is beyond the scope of this thesis and thus left to the interpretation of the reader.

It all started in late 2008 with Prof. Tibor Grasser sending me a paper of Prof. Christoph Jungemann. Prof. Grasser was convinced that the SHE method is the ideal topic for a microelectronics-mathematics hybrid like myself. In retrospective, I am very glad that he has not mentioned at that time that other students had failed to achieve notable progress while working on the method. Consequently, the year 2009 was mostly devoted to making myself familiar with the existing literature and to summarizing my gained knowledge in a master's thesis supervised by Prof. Ansgar Jüngel. Even though only one-dimensional n^+nn^+ -diodes were investigated numerically, first experiences with the peculiarities of the Boltzmann transport equation could already be gathered. Also, the mathematical focus led to first results on the coupling structure of the SHE equations.

In February 2010 I was given the chance to visit the group of Prof. Jungemann at the Bundeswehr University in Neubiberg, Munich. The first results on the coupling structure could be refined, yet my personal aim for the stay was to have a first implementation of a spatially two-dimensional SHE simulator ready when heading back to Vienna. This essentially required to restart from scratch and to come up with a two-dimensional drift-diffusion implementation in order to have a reasonable initial guess for the electrostatic potential. Moreover, an incomplete LU factorization preconditioner for the convergence of the iterative solvers had to be implemented. As a huge fan of winter sports, it required a lot of discipline to keep myself on coding in the evenings rather than watching the Olympic Winter Games, which were held in Vancouver during that time and thus broadcasted in Europe during the evening. The fruits of spending my time with my laptop and C++ instead of the television became visible on the last day of my stay, where the spatially two-

dimensional simulation of a simple n^+nn^+ -diode was completed. This paved the way for improvements on the SHE method in the months to come. I wish to thank Prof. Jungemann, Mr. Hong, Mr. Kovarik, Mr. Kraus, Mr. Matz, Mr. Thao and Mr. Dinh for hosting me in such a productive atmosphere.

It soon became apparent that a parallel preconditioner for SHE should be the next step. I could convince my colleague and friend Florian Rudolf (*‘kleiner Meister’*), who shares a lot of interest in programming graphics adapters with me, to work on a master’s thesis investigating the usefulness of **OpenCL** for general purpose computations on graphics adapters and multi-core central processing units. We spent two intensive weeks of implementing linear algebra, which after some final polishing resulted in the first release of **ViennaCL**. While the iterative solvers showed a speed-up of up to one order of magnitude compared to conventional single-threaded implementations, the incomplete LU factorization could not be accelerated properly due to its serial nature, thus prolongating the hunt for a parallel preconditioner for SHE.

During that time Josef Weinbub joined the development of **ViennaCL**. I could benefit a lot from his advanced knowledge of generic programming, which has entered **ViennaCL** on the one hand, and which also allowed me to reconsider the internals of the SHE simulator. Even though he had no direct contact with the SHE simulator and still considers it ‘evil witchcraft’, always leading to a smile on my face, he had a high influence on the coding style and design. I am deeply indebted for his indirect contributions, of which he may not be fully aware of.

Former experiences with finite element implementations and the now increased generic programming skills paired with experiences from subsequent **ViennaCL** releases led to the decision of a rigorous orthogonalization of software components in order to cope with the complexities of numerical methods in general and the SHE method in particular. It was clear to me that this decision required additional implementation effort at the beginning, but will pay off in the long run. At the end of 2010, **ViennaData** was essentially finished, and **ViennaGrid** reached a functional state in January 2011.

In February 2011, the combination of the individual software components **ViennaCL** for linear algebra, **ViennaGrid** for mesh management and **ViennaData** for the storage of quantities on mesh elements have all of a sudden lead to an enormous pace in the development of the SHE simulator **ViennaSHE**. Since the former three libraries have been tested and verified within other applications as well, **ViennaSHE** could be kept lightweight and with a focus on the algorithms specific to the SHE method only. This has reduced the time required for debugging to a bare minimum, simply because the amount of code in which a particular bug may show up was always very small and expressive. By the beginning of March, adaptive variable-order SHE as well as a parallel preconditioner were implemented and verified for a one-dimensional n^+nn^+ -diode.

A little later in April, Prof. Grasser challenged me by asking for the possibility to extend **ViennaSHE** to unstructured grids and to extend the still brand-new adaptive variable orders and parallelization. Since this question was not new to me at that time, I replied that I expected the results from the one-dimensional evaluation to be transferable to spatially two-dimensional device simulations, hence it should work out. However, when he added that we should submit results for fully three-dimensional devices, I was very doubtful about this being possible given the other obligations I had until the deadline at the end of June. Instead of finding reasons why it definitely cannot be possible, I started with the required implementations. Without giving details about a race against time which ended 24 min-

utes before the extended deadline, I succeeded in submitting the results – and finally got accepted. Therefore, I wish to thank Prof. Grasser for continuously directing me in the right directions, and for being a positive example of a person who lives passion for science and his family.

I also wish to thank Prof. Ansgar Jüngel for his support and excitement whenever I reported new functionalities of **ViennaSHE**. In particular, he had been eagerly looking forward to full three-dimensional device simulations using the SHE method from the very beginning, hence I am very glad that it indeed all worked out. My thanks also go to Prof. Siegfried Selberherr, whose wide range of scientific sight and advise as well as his desire for highest quality I highly appreciate. Even though he is not my doctoral advisor, he always provided helpful guidance and plenty of valuable suggestions throughout my studies. I am also indebted to Prof. Erasmus Langer, who does a great job as head of the Institute for Microelectronics and cared for a fruitful environment especially during the financial crisis. I highly enjoyed sharing a room with Dr. Hajdin Ceric and Dr. Roberto Lacerda de Orio during the first half of my doctoral studies and wish to thank them for many interesting discussions. Markus Bina has been highly motivated and interested in joining the development of **ViennaSHE** from the day he joined the institute, but due to other obligations he had to restrict to verbally sharing his experiences with **MinimosNT** and giving advice on potential user requirements for **ViennaSHE**. I highly appreciate his input and look forward to the near future, which will finally allow him to actively join the development. In order to keep a reasonable scope of this preface, I collectively thank my co-workers at the Institute for Microelectronics and the Institute for Analysis and Scientific Computing for a respectful working environment.

A large amount of this thesis has been written at the Gasthof Schlagobersbauer in Alpl, Styria, home town of the Styrian poet Peter Rosegger. I express my gratitude to Fam. Leitner, who ensured that I can fully focus on my writing. Nonetheless, the subsequent pages cannot compete with the literary excellence of Rosegger's work.

The high level of motivation during my work on and around **ViennaSHE** would have been impossible without the deliberate and highly enjoyable distractions in the form of various gatherings and events with my friends, such as *Neujahrs-LAN*, birthday parties or evenings spent with cooking and/or sufficiently large amounts of exotic food. Thank you very much.

As a first quantum of return for unconditional support during my studies, I hope that my whole family can enjoy the completion of this thesis with me. In particular, and most importantly, I wish to thank Doris for her love and the tremendous amount of patience she offered throughout my studies.

Karl Rupp
November 2011

Contents

1	Introduction	1
1.1	Semiclassical Carrier Transport	1
1.2	Requirements of Modern TCAD	7
1.3	Outline	8
2	The SHE Equations	10
2.1	Historical Overview	10
2.2	Derivation of the SHE Equations	12
2.3	H -Transform and MEDS	16
2.4	Self-Consistency with Poisson's Equation	20
2.5	Compatibility with Modern TCAD	23
3	Physical Modeling	25
3.1	Spherically Symmetric Energy Band Models	25
3.2	Incorporation of Full-Band Effects	27
3.3	Linear Scattering Operators	30
3.4	Nonlinear Scattering Operators	33
4	Structural Properties	38
4.1	Sparse Coupling for Spherical Energy Bands	38
4.2	Coupling for Nonspherical Energy Bands	42
4.3	Stabilization Schemes	43
4.4	Boundary Conditions	44
4.5	Solution of the Linear System	45
4.6	Results	47
5	SHE on Unstructured Grids	51
5.1	The Box Integration Scheme	51
5.2	Construction of Boxes	52
5.3	Box Integration for SHE	57
5.4	Results	61
6	Adaptive Variable-Order SHE	63
6.1	Variable-Order SHE	64
6.2	Adaptive Control of the SHE Order	67
6.3	Results	72

7	Parallelization	80
7.1	Energy Couplings Revisited	81
7.2	Symmetrization of the System Matrix	82
7.3	A Parallel Preconditioning Scheme	85
7.4	Results	87
8	Numerical Results	90
8.1	MOSFET	90
8.2	FinFET	93
9	Outlook and Conclusion	101
9.1	Possible Further Improvements of the SHE Method	101
9.2	Conclusion	104
A	Mathematical Tools	106
A.1	The Kronecker Product	106
A.2	Wigner 3jm Symbols	107
	Bibliography	108

Notation

Symbols

Symbol	Meaning
\mathbb{R}	set of real numbers
$\ \cdot \ $	norm of the argument
$ \cdot $	modulus of the argument
$\mathcal{O}(\cdot)$	Landau symbol
Ω	unit sphere
θ	colatitude (polar angle)
φ	longitude (azimuth)
$d\Omega$	unit sphere surface element, $\sin \theta d\theta d\varphi$
$\mathbf{e}_\theta, \mathbf{e}_\varphi$	unit vectors w.r.t. θ and φ
∇	Nabla operator
Δ	Laplace operator
\mathbf{A}, \mathbf{B}	matrices (capital letters, bold)
\mathbf{v}, \mathbf{w}	vectors (lowercase, bold)
$Y^{l,m}$	real valued spherical harmonic of major index l and minor index m
$X_{l,m}$	spherical harmonics expansion coefficient to $Y^{l,m}$ of the quantity X
$\delta_{i,j}$	Kronecker delta
$\delta(\cdot)$	delta distribution
\mathcal{T}	triangulation of the simulation domain
\mathcal{B}	Voronoi box grid of \mathcal{T}
B_i	a box from the adjoint box grid \mathcal{B}
$\tilde{\mathcal{B}}$	dual box grid of \mathcal{B}
$\tilde{B}_{i,j}$	a box from the box grid \mathcal{B} overlapping B_i and B_j
$A_{i,j}$	interface area between boxes B_i and B_j
$V_{i,j}$	volume fraction of the boxes B_i and B_j associated with $A_{i,j}$
$\mathbf{n}_{i,j}$	surface unit normal vector of box B_i pointing into B_j
N	number of degrees of freedom in (\mathbf{x}, H) -space
$N_{\mathbf{x}}$	number of degrees of freedom in \mathbf{x} -space
N_H	number of discrete total energies H_i
L	spherical harmonics expansion order

Symbol	Meaning
\hbar	Planck constant divided by 2π
k_B	Boltzmann constant
ϵ	permittivity (not to be confused with kinetic energy ϵ)
ρ	space charge
$ q $	elementary charge
q	charge of a carrier (negative for electrons, positive for holes)
m^*	effective mass
ϵ	kinetic energy (not to be confused with permittivity ϵ)
H	total energy
t	time
\mathbf{x}	spatial coordinate within the device
\mathbf{k}	wave vector
\mathbf{p}	momentum vector
\mathbf{v}	(group) velocity
\mathbf{F}	force
\mathbf{E}	electric field
ψ	quasi-electrostatic potential
$Q\{\cdot\}$	scattering operator
$Q^{\text{in}}\{\cdot\}$	in-scattering operator
$Q^{\text{out}}\{\cdot\}$	out-scattering operator
$Q^{\text{VR}}\{\cdot\}$	velocity-randomizing scattering operator
η	index of the scattering process
$s(\mathbf{x}, \mathbf{k}, \mathbf{k}')$	scattering coefficient
$\sigma(\mathbf{x}, \mathbf{k}, \mathbf{k}')$	symmetric scattering coefficient
$n(\mathbf{x}, t)$	particle density (electron density)
$Z(\epsilon, \theta, \varphi)$	generalized density of states
$\langle \cdot \rangle$	moment of the BTE with respect to the argument
$f(\mathbf{x}, \mathbf{k}, t)$	distribution function
$g(\mathbf{x}, \mathbf{k}, t)$	generalized energy distribution function
$\mathbf{j}_{l,m}$	generalized current density term
$\mathbf{\Gamma}_{l,m}$	spherical harmonics coupling term
V_T	thermal voltage

Abbreviations

BTE	Boltzmann transport equation
CPU	central processing unit
GPU	graphics processing unit
FET	field effect transistor
MEDS	maximum entropy dissipation scheme
MOSFET	metal-oxide-semiconductor field effect transistor
SHE	spherical harmonics expansion
TCAD	technology computer aided design

Chapter 1

Introduction

With the continued shrinking of semiconductor devices, a deeper understanding of the underlying physical processes is required in order to further improve device performance. Since it is impossible to measure all details of carrier transport on the nanometer scale, the availability of accurate theoretical descriptions is essential in order to gain insight into the physical processes by means of numerical simulations. This so-called Technology Computer Aided Design (TCAD) has become an indispensable ingredient for the development of faster, smaller and more power-efficient devices.

Quantum effects have long been negligible for charge transport, but they gain importance with each technology generation. Nevertheless, quantum effects are not considered further within this thesis, even though the theory of carrier scattering is based on a quantum mechanical foundation [67].

1.1 Semiclassical Carrier Transport

The Boltzmann Transport Equation (BTE) is commonly considered to provide the best semiclassical description of carrier transport. Carriers are described in a classical fashion by a continuous distribution function f , which depends on the spatial location \mathbf{x} , momentum \mathbf{p} and time t . The carrier momentum \mathbf{p} is related to a quantum-mechanical wave number \mathbf{k} by the relation $\mathbf{p} = \hbar\mathbf{k}$, where \hbar is the modified Planck constant. Without going into the details of various derivations (see e.g. [50, 67, 68]), the BTE is given by

$$\frac{\partial f}{\partial t} + \mathbf{v} \cdot \nabla_{\mathbf{x}} f + \mathbf{F} \cdot \nabla_{\mathbf{p}} f = Q\{f\}, \quad (1.1)$$

where function arguments are omitted. Here, \mathbf{v} denotes the carrier velocity in dependence of the carrier momentum, \mathbf{F} refers to the electrostatic force, and Q is the scattering operator. A formulation based on the wavevector \mathbf{k} rather than momentum \mathbf{p} transforms the gradient as $\nabla_{\mathbf{p}} \mapsto \nabla_{\mathbf{k}}/\hbar$.

The description of carries by means of a distribution function with respect to the spatial variable \mathbf{x} , the momentum \mathbf{p} and time t leads to a seven-dimensional problem space, which makes the direct solution of the BTE very demanding. As a consequence, simpler macroscopic models have been derived from moments of the BTE. Most noteworthy in this regard are the drift-diffusion equations presented in Sec. 1.1.1, which are obtained from the zeroth and first moment of the BTE.

While the drift-diffusion equations have been successfully employed throughout the 20th century for TCAD, the characteristic lengths of modern devices are well outside the range of validity of the model. Hence, even though variants of the drift-diffusion equations are still in use for the simulation of recent device generations, their accuracy is highly questionable and leads to poor results already in the linear regime [51]. More accurate macroscopic transport models have been derived based on higher moments of the Boltzmann Transport Equation (BTE). The energy transport model and the hydrodynamic model are derived from the first four moments of the BTE and presented in Sec. 1.1.3 and Sec. 1.1.2 respectively. In Sec. 1.1.4 a transport model based on the first six moments of the BTE is discussed.

Despite the good results obtained from macroscopic models, which are derived from moments of the BTE in the micron and sub-micron regime, the necessary approximations cease to hold in the deca-nanometer regime. As a consequence, a full solution of the BTE is desired. Since direct numerical methods are typically limited by memory constraints which stem from the resolution of the high-dimensional simulation domain, the method of choice is usually the stochastic Monte Carlo method, which is presented in Sec. 1.1.5.

It should be noted that each of the transport models presented in the following has to be solved self-consistently with the Poisson equation. To this end, nonlinear iteration schemes such as those detailed in Sec. 2.4 are typically employed. For the sake of brevity, self-consistency is not further addressed in the following subsections.

1.1.1 The Drift-Diffusion Model

Taking the zeroth-order moment of the BTE (1.1) leads to

$$\frac{\partial n}{\partial t} = \frac{1}{|q|} \nabla \cdot \mathbf{J}_n - R_n, \quad (1.2)$$

$$\frac{\partial p}{\partial t} = -\frac{1}{|q|} \nabla \cdot \mathbf{J}_p - R_p, \quad (1.3)$$

where n and p denote electron and hole densities and $|q|$ is the elementary charge¹. The recombination rates R_n and R_p refer to Auger, radiative, and Shockley-Read-Hall [34, 95] processes and can be expressed in terms of n and p . Multiplication of the BTE with the wave vector \mathbf{k} and integration over the \mathbf{k} -space leads to equations for the current densities \mathbf{J}_n and \mathbf{J}_p :

$$\mathbf{J}_n = -n|q|\mu_n \nabla \psi + |q|D_n \nabla n \quad (1.4)$$

$$\mathbf{J}_p = -p|q|\mu_p \nabla \psi - |q|D_p \nabla p \quad (1.5)$$

Carrier mobilities are denoted by μ_n and μ_p , while D_n and D_p are diffusion coefficients. Substitution of (1.4) and (1.5) into (1.2) and (1.3) leads to a system of two partial differential equations for the densities n and p . Equipped with suitable boundary conditions, these equations completely specify the electron and hole densities. This so-called *drift-diffusion* model was first derived by Van Roosbroeck in 1950 [103].

As a prelude to numerical stabilization schemes discussed in Sec. 4.3, a direct discretization of the drift-diffusion model by simple methods such as finite differences usually fails

¹In the literature, q (or e) sometimes refers to the signed charge, and sometimes to the unsigned elementary charge. To avoid confusion, the $|q|$ is used in this work to refer to the elementary charge, while q is the signed charge of an electron or hole.

due to large forces inside the device. Numerical stability for the drift-diffusion equations is increased substantially by the use of upwind schemes in general, and the Scharfetter-Gummel scheme [90] in particular. Additionally, a discretization is usually required to conserve current, hence box integration schemes are commonly employed [93].

1.1.2 The Hydrodynamic Model

The consequence of taking the zeroth and the first moment of the BTE for the derivation of the drift-diffusion model only is that a spatial dependence of average carrier energies are ignored. To overcome these deficiencies, Bløtkjær derived conservation equations by taking the zeroth, the first and the second moments of the BTE [5]. As closure condition for the heat flux density $n\mathbf{S}_n$, Fourier's law is applied, which leads for electrons to the system

$$\frac{\partial n}{\partial t} = \frac{1}{|q|} \nabla \cdot \mathbf{J}_n, \quad (1.6)$$

$$\mathbf{J}_n - \frac{\tau_1}{|q|} \left(\mathbf{J}_n \otimes \frac{\mathbf{J}_n}{n} \right) = \mu k_B \nabla (n T_n) + |q| n \mu \mathbf{E} - \tau_1 \frac{\partial \mathbf{J}_n}{\partial t}, \quad (1.7)$$

$$\nabla \cdot (n \mathbf{S}_n) = -\frac{\partial n w}{\partial t} + \mathbf{E} \cdot \mathbf{J}_n - n \frac{w - w_0}{\tau_2}, \quad (1.8)$$

$$n \mathbf{S}_n = -\frac{1}{|q|} (w + k_B T_n) \mathbf{J}_n - \kappa(T_n) \nabla T_n. \quad (1.9)$$

The model needs to be solved for the unknown electron density n , the electron temperature T_n and the average energy w . The contribution of the drift velocity to the carrier energy is often neglected, resulting in $w \approx 3k_B T_n/2$. The parameters τ_1 and τ_2 stem from the first and the second moment of the scattering operator in the relaxation time approximation, κ refers to the thermal conductivity and is given by the Wiedemann-Franz law

$$\kappa(T_n) = \left(\frac{5}{2} - r \right) \left(\frac{k_B}{q} \right)^2 |q| \mu n T_n \quad (1.10)$$

with w_0 denoting the average energy at equilibrium. The correction factor r stems from the fact that thermal and electrical conductivity do not exclusively involve the same carriers. A similar set of equations is obtained for holes.

Equations (1.6) to (1.9) describe the *full hydrodynamic model* for parabolic band structures. The name stems from the similarity to the Euler equations of fluid dynamics with the addition of a heat conduction term and the collision terms. Due to its hyperbolic nature at high electron flows, the hydrodynamic model can lead to shock waves inside the device, which shows up in short-length devices or low temperatures. This leads to additional effort required for stable numerical schemes compared to the parabolic convection-diffusion type of the drift-diffusion equations.

1.1.3 The Energy Transport Model

A frequent approximation to the hydrodynamic equations (1.6) to (1.9) is to neglect the convective term

$$\frac{\tau_1}{|q|} \left(\mathbf{J}_n \otimes \frac{\mathbf{J}_n}{n} \right) \quad (1.11)$$

in (1.7), and to neglect the contribution of velocity to the carrier energy, thus

$$w \approx \frac{3}{2}k_B T_n. \quad (1.12)$$

This leads to a parabolic system of equations and is a very common approximation in today's device simulators [30]. The two assumptions (1.11) and (1.12) can also be justified from a mathematical point of view by a scaling argument for vanishing Knudsen number [84], which in addition shows that the time derivatives in the flux equations vanish. This leads to the *energy transport model*

$$\frac{\partial n}{\partial t} = \frac{1}{|q|} \nabla \cdot \mathbf{J}_n, \quad (1.13)$$

$$\mathbf{J}_n = \mu k_B \nabla(n T_n) + |q| n \mu \mathbf{E}, \quad (1.14)$$

$$\nabla \cdot (n \mathbf{S}_n) = -\frac{\partial n w}{\partial t} + \mathbf{E} \cdot \mathbf{J}_n - n \frac{w - w_0}{\tau_2}, \quad (1.15)$$

$$n \mathbf{S}_n = -\frac{5k_B T_n}{2|q|} \mathbf{J}_n - \left(\frac{5}{2} - r\right) \left(\frac{k_B}{q}\right)^2 |q| \mu n T_n \nabla T_n, \quad (1.16)$$

where (1.10) has been used. As the model consists of two conservation equations and two constitutive equations, the name is slightly misleading.

The closure based on Fourier's law can be improved by taking the third moment of the BTE into account [63]. A closure condition for the fourth-order tensor is obtained by assuming a heated Maxwellian distribution, leading to

$$n \mathbf{S}_n = -\frac{\mu_S}{\mu} \frac{5k_B T_n}{2|q|} \mathbf{J}_n - \frac{\mu_S}{\mu} \frac{5}{2} \left(\frac{k_B}{q}\right)^2 |q| \mu n T_n \nabla T_n \quad (1.17)$$

instead of (1.16). This improved model based on four moments of the BTE is referred to as the *four moments energy transport model*. A comparison of (1.16) and (1.17) reveals an inconsistency of the energy transport model based on three moments, because the scalar prefactors in (1.16) are given by $5/2$ and $5/2 - r$, which means that the heat flux can be adjusted independently [30].

1.1.4 The Six-Moments Model

With the drift-diffusion model based on two moments of the BTE, the hydrodynamic model based on three moments and the energy transport model in modified form based on four moments of the BTE, it is tempting to construct more accurate models based on higher moments. However, the selection of suitable closure conditions becomes increasingly difficult. A model loosely based on six moments of the BTE has been proposed by Sonoda *et al.* [98]. A rigorous derivation of a model based on six moments has been carried out by

Grasser *et al.* [29] in the diffusion limit of vanishing Knudson number:

$$\frac{\partial n}{\partial t} = \frac{1}{|q|} \nabla \cdot \mathbf{J}_n, \quad (1.18)$$

$$\mathbf{J}_n = \mu k_B \nabla(nT_n) + |q|n\mu\mathbf{E}, \quad (1.19)$$

$$\nabla \cdot (n\mathbf{S}_n) = -\frac{\partial nw}{\partial t} + \mathbf{E} \cdot \mathbf{J}_n - n\frac{w-w_0}{\tau_2}, \quad (1.20)$$

$$n\mathbf{S}_n = -\frac{\mu_S}{\mu} \frac{5k_B T_n}{2|q|} \mathbf{J}_n - \frac{\mu_S}{\mu} \frac{5}{2} \left(\frac{k_B}{q}\right)^2 |q| \mu n T_n \nabla T_n, \quad (1.21)$$

$$\nabla \cdot (n\mathbf{K}_n) = -\frac{15}{4} k_B^2 \frac{\partial(nT_n\Theta_n)}{\partial t} - 2|q| \mathbf{E} \cdot \mathbf{S}_n - \frac{15}{4} n \frac{T_n\Theta_n - T_L^2}{\tau_4}, \quad (1.22)$$

$$n\mathbf{K}_n = \frac{35}{4} \frac{k_B^3}{|q|} \frac{\mu_k}{\mu_n} \mu_n \left[\nabla(nM_6) + \frac{|q|}{k_B} \mathbf{E} n T_n \Theta_n \right]. \quad (1.23)$$

The additional unknown variables are the second order temperature Θ_n and the kurtosis flux \mathbf{K}_n . The parameter μ_k can be related to a mobility for kurtosis and τ_4 is a macroscopic relaxation time for the fourth moment of the scattering operator. A closure condition for the sixth moment M_6 is obtained via the empirical relation

$$M_6 = T_n^3 \left(\frac{\Theta_n}{T_n}\right)^c, \quad c \in [0, 3]. \quad (1.24)$$

A value of 2.7 for the parameter c proved to provide highest accuracy when compared to Monte Carlo results and further shows higher numerical stability than other choices. Particularly, the Newton procedure for the choice $c = 1$ has been reported to result in failure of convergence in most cases.

1.1.5 The Monte Carlo Method

The macroscopic transport models presented so far are specified by a system of partial differential equations which approximate certain features of the BTE, for which suitable deterministic numerical solutions are sought. A stochastic approach for the solution of the full BTE is the Monte Carlo method, where the dynamics are simulated at the particle level [47, 52] and which was already used in the 1960s for semiconductor device simulations (e.g. [61]). The free streaming operator of the BTE is obtained from Newton's laws of motion

$$\hbar \frac{\partial \mathbf{k}}{\partial t} = \mathbf{F}, \quad \frac{\partial \mathbf{x}}{\partial t} = \mathbf{v}, \quad (1.25)$$

while the scattering operator models instantaneous changes of the momentum of each particle in the device. Denote with $p(\mathbf{x}, \mathbf{k}, t | \mathbf{x}_0, \mathbf{k}_0, t_0)$ the conditional probability of finding a particle at location \mathbf{x} with wave vector \mathbf{k} at time t given that the particle was at location \mathbf{x}_0 with wave vector \mathbf{k}_0 at time t_0 . Since not only the distribution function $f(\mathbf{x}, \mathbf{k}, t)$, but also $p(\mathbf{x}, \mathbf{k}, t | \mathbf{x}_0, \mathbf{k}_0, t_0)$ satisfies the BTE, a formal integration of the BTE after merging

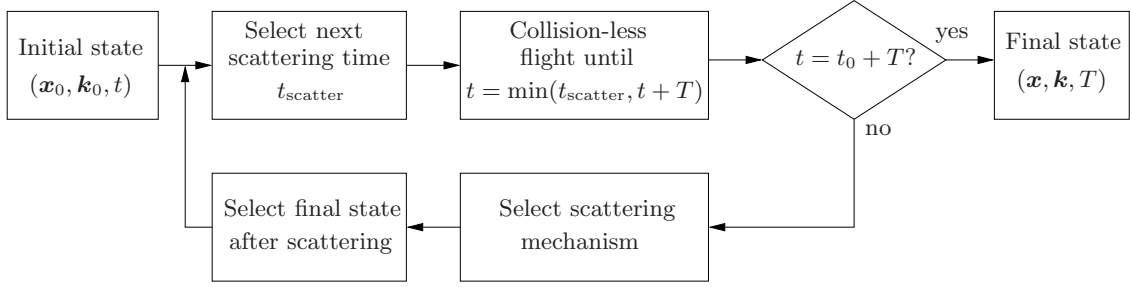


Figure 1.1: Flowchart for the Monte Carlo method for a simulation from time t to $t + T$.

the gradients with respect to \mathbf{x} and \mathbf{k} into a joint gradient for the variable $\zeta = (\mathbf{x}, \mathbf{k})$ yields

$$\begin{aligned}
 p(\mathbf{x}, \mathbf{k}, t | \mathbf{x}_0, \mathbf{k}_0, t_0) &= p_0(\mathbf{x}, \mathbf{k}, t | \mathbf{x}_0, \mathbf{k}_0, t_0) \\
 &+ \int_{t_0}^t \int_{\mathbb{R}^3 \times \mathbb{B} \times \mathbb{R}^3 \times \mathbb{B}} p(\mathbf{x}_1, \mathbf{k}_1, t_1 | \mathbf{x}_0, \mathbf{k}_0, t_0) s(\mathbf{k}_1, \mathbf{k}'_1) \\
 &\quad \times p_0(\mathbf{x}, \mathbf{k}, t | \mathbf{x}'_1, \mathbf{k}'_1, t_1) d\mathbf{x}'_1 d\mathbf{k}'_1 d\mathbf{x} d\mathbf{k} dt_1,
 \end{aligned} \tag{1.26}$$

where \mathbb{B} denotes the Brillouin zone and

$$p_0(\mathbf{x}, \mathbf{k}, t | \mathbf{x}_0, \mathbf{k}_0, t_0) = \begin{cases} \exp(-\int_{t_0}^t s(\mathbf{x}^*(\tau | \mathbf{x}_0, \mathbf{k}_0, t), \mathbf{k}^*(\tau | \mathbf{x}_0, \mathbf{k}_0, t)) d\tau), & (\mathbf{x}, \mathbf{k}) = (\mathbf{x}^*, \mathbf{k}^*) \\ 0, & \text{otherwise} \end{cases} \tag{1.27}$$

is the conditional probability of finding a particle in state (\mathbf{x}, \mathbf{k}) at time t given that the particle was located at \mathbf{x}_0 with wave vector \mathbf{k}_0 at time t_0 without being scattered. \mathbf{x}^* and \mathbf{k}^* are shorthand notations for the location of the particle at a given instance in time for a given initial position. Eq. (1.26) is an integral equation for $p(\mathbf{x}, \mathbf{k}, t | \mathbf{x}_0, \mathbf{k}_0, t_0)$, and the conjugate form

$$\begin{aligned}
 p(\mathbf{x}, \mathbf{k}, t | \mathbf{x}_0, \mathbf{k}_0, t_0) &= p_0(\mathbf{x}, \mathbf{k}, t | \mathbf{x}_0, \mathbf{k}_0, t_0) \\
 &+ \int_{t_0}^t \int_{\mathbb{R}^3 \times \mathbb{B} \times \mathbb{R}^3 \times \mathbb{B}} p_0(\mathbf{x}_1, \mathbf{k}_1, t_1 | \mathbf{x}_0, \mathbf{k}_0, t_0) s(\mathbf{k}_1, \mathbf{k}'_1) \\
 &\quad \times p(\mathbf{x}, \mathbf{k}, t | \mathbf{x}'_1, \mathbf{k}'_1, t_1) d\mathbf{x}'_1 d\mathbf{k}'_1 d\mathbf{x} d\mathbf{k} dt_1,
 \end{aligned} \tag{1.28}$$

is the basis for the usual Monte Carlo algorithm.

The Monte Carlo procedure uses a large sample of particles and simulates their dynamic behavior based on the integral formulation (1.28). To this end, the time intervals between the scattering events of each particle are chosen randomly based on the scattering operator, and particles propagate in collision-less flight according to (1.25) between scattering events. Macroscopic quantities such as average carrier energies are computed by suitable averages over the particle ensemble. In order to keep stochastic fluctuations reasonably small, a large number of particles is required, where the accuracy is asymptotically proportional to the square-root of the execution time unless special enhancement techniques for selected target quantities are applied [52]. While the Monte Carlo method provides a very high accuracy due to the simulation of particle kinetics and high flexibility with respect to the inclusion of additional physical details, it is computationally extremely expensive.

1.2 Requirements of Modern TCAD

The various transport models and solution approaches to the BTE discussed in the previous section represent only a selection of the most popular methods for the simulation of charge transport in semiconductors. Regarding their accuracy and computational cost, these models typically range from the computationally cheap drift-diffusion model, which fails to reflect physics properly in the deca-nanometer regime, to the accurate Monte Carlo method, which has the drawback of extremely high computational costs. In the following, a discussion of the requirements of a state-of-the-art semiconductor device simulator is given. The individual requirements slightly overlap, but they should aid the reader in judging the importance of the proposed extensions of the deterministic Boltzmann solution method given in the remainder of this thesis.

1.2.1 Accuracy

The need for a better reflection of the underlying physical processes compared to the drift-diffusion model has led to the development of higher-order transport models such as the hydrodynamic model. As device dimensions decrease, ballistic effects become significant, which cannot be captured in the diffusion-limited regime of higher-order transport models [30, 51]. As a consequence, it is desirable to have numerical methods which are computationally less expensive than the Monte Carlo method, but are able to resolve ballistic transport effects. Even though not covered by the semiclassical approach, quantum effects become increasingly important and should be reflected in the model.

1.2.2 Charge Conservation

Kirchhoff's current law states the conservation of charge. Consequently, charge conservation has to be ensured during the simulation of a single semiconductor device as well. The use of the box integration scheme for the drift-diffusion model guarantees charge conservation at the algebraic level. Similarly, charge conservation is provided for other moment-based methods. Moreover, the particle approach of the Monte Carlo method allows for charge conservation without difficulties. As a consequence, new simulation approaches need to ensure charge conservation in order to be competitive with existing methods.

1.2.3 Self-Consistency

The electrostatic potential and the space charge are linked by the Poisson equation, which is a direct implication of Gauss' Law. Since it is in general neither possible to explicitly express the potential as a function of the carrier densities, nor to express the carrier densities as an explicit function of the electrostatic potential only, any transport model used for charge transport is required to be solved self-consistently with the Poisson equation.

1.2.4 Resolution of Complicated Domains

With the on-going miniaturization of semiconductor devices, inherent small variations in the fabrication process become significant with respect to the characteristic device lengths. Consequently, device geometries are no longer simple compositions of geometric primitives,

but should be taken from topography simulations. Therein, complicated device geometries show up in a natural way, particularly for fully three-dimensional device layouts.

1.2.5 Computational Feasibility

The incredible pace of semiconductor device technology requires that simulation results are available within a short time frame. In particular, simulation times in the range of weeks or even months are clearly not acceptable, because during that time technology has progressed and simulation results may be deprecated already before they are available. This is the main reason why Monte Carlo methods are – despite their high accuracy – not commonly used for every-day TCAD purposes.

1.2.6 Extendibility

As devices are scaled down, formerly negligible physical effects become relevant and need to be considered in the simulation. Thus, it is desirable to use numerical methods which allow for such an inclusion without a large redesign of the whole simulator. For instance, boundary element methods based on the knowledge of the Green's function of the underlying partial differential equations become invalid and eventually infeasible as soon as details such as e.g. space-dependent diffusion coefficients are demanded.

1.3 Outline

The remainder of this thesis focuses on a rather new approach based on a spherical harmonics expansion of the distribution function. The method is expected to yield the accuracy of Monte Carlo methods without the inherent disadvantages of stochastic models. Other approaches for the deterministic numerical solution of the BTE have been proposed, but they are considered to be limited to at most two-dimensional device geometries either because the full momentum space needs to be discretized [14, 19], or because the discretization method leads to nonlocal couplings resulting in huge memory requirements for the resulting linear system of equations [72].

In Chap. 2 an introduction to the SHE method is given and the state-of-the-art for the method is presented, excluding the extensions proposed in this work. The chapter closes with a discussion of the compatibility of the SHE method with respect to modern TCAD.

Chap. 3 details the underlying physical processes and their consideration within the SHE method. A method for the inclusion of carrier-carrier scattering is proposed at the end of the chapter.

The mathematical structure of the SHE equations is investigated in detail in Chap. 4. A sparse coupling property of the SHE equations is shown for spherical energy bands. These coupling investigations then lead to a system matrix compression scheme, which allows for a memory efficient representation of the system matrix at high expansion orders.

Chap. 5 presents the extension of the SHE method to unstructured grids. All the required implementation details for the construction of suitable meshes are given.

In order to obtain the accuracy of higher-order expansions at lower computational effort, adaptive variable-order expansions are proposed and evaluated in Chap. 6. The possible savings mostly stem from the fact that on the one hand the distribution function is still close to equilibrium in inactive device regions, and on the other hand from the asymptotically

exponential decay of the distribution function with respect to kinetic energy, hence lower resolution at higher energies is sufficient.

Recent developments in computing architecture are addressed in Chap. 7, where a parallel scheme for the convergence enhancement of the iterative solvers by means of preconditioners is suggested. It enables the full utilization of multi-core central processing units as well as the efficient use with massively parallel architectures such as graphics processing units.

The suggestions from Chaps. 4 to 7 are combined for the simulation of a MOSFET and a FinFET in Chap. 8. It is demonstrated that the proposed techniques blend well with each other and render the SHE method very attractive for modern TCAD.

An outlook to further possible improvements of the SHE method is presented in Chap. 9. A conclusion finally closes this thesis.

Chapter 2

The SHE Equations

This chapter gives a brief introduction to the spherical harmonics expansion (SHE) method for the deterministic numerical solution of the BTE. First, the developments since the introduction of the method in the early 1990s are discussed. Connections with the new contributions presented in this work are established as much as possible. Then, the formulation of the SHE equations as proposed by Jungemann *et al.* [53] and later refined by Hong *et al.* [42] is presented, which is also the foundation for the contributions in subsequent chapters. The chapter closes with a comparison of the requirements on modern TCAD given in Sec. 1.2 and the current state-of-the-art of the SHE method.

2.1 Historical Overview

First journal publications on the SHE method date back to Gnudi *et al.* [21] as well as Goldsman *et al.* [25] in 1991. However, a precursor of the method has already been used in the PhD thesis of Goldsman in 1989 [24]. Even though the method formally relies on an expansion of the distribution function $f(\mathbf{x}, \mathbf{k}, t)$ with spatial location \mathbf{x} , wave vector \mathbf{k} and time t into spherical harmonics $Y^{l,m}$ of the form

$$f(\mathbf{x}, \mathbf{k}, t) = \sum_{l=0}^{\infty} \sum_{m=-l}^l f_{l,m}(\mathbf{x}, \varepsilon, t) Y^{l,m}(\theta, \varphi) , \quad (2.1)$$

where the three-dimensional wave vector \mathbf{k} is written in spherical coordinates ε , θ and φ on equi-energy surfaces, the derivation of equations for the expansion coefficients was rather based on perturbations of the ground state at $l = 0$ than on a clean mathematical approach such as a Galerkin scheme. Consequently, the derivation of the equations required a lot of bookkeeping. Nevertheless, the first-order expansion was extended to the two- and multi-dimensional case soon after [23, 110]. It is worthwhile to mention the H -transform, which has been proposed already at a very early stage in the development of the SHE method [23].

In the mid-1990s a large number of publications dealt with the SHE method. Lin *et al.* derived a Scharfetter-Gummel-type stabilization [65] for the first-order SHE method, and coupled the SHE method for electrons with the Poisson equation and the hole continuity equation [66]. Hennacy *et al.* [37, 38] extended the method to arbitrary order expansions. A comparison of different boundary conditions has been carried out by Schroeder *et al.* [92]. Vecchi *et al.* [105] proposed an efficient solution scheme based on a multigrid-like refinement of the grid near the conduction band edge. Moreover, a decoupling of the

system of linear equations after discretization is discussed for the case that only one inelastic scattering mechanism with constant energy transfer is considered. Even though the techniques presented therein differ substantially from those discussed in Chap. 6 and Chap. 7, the crucial role of inelastic scattering for the coupling structure and methods for the resolution enhancement near the band edge have been discussed already. The same group proposed a scheme for incorporating full-band effects for both the conduction and the valence band [106,107]. The publication by Rahmat *et al.* [78] observed that the spatial terms of the SHE equations can be handled separately from the angular coupling, which is the key observation used throughout Chap. 4. However, this separation was given as an implementation hint for the assembly of the Jacobian matrix only, while in Chap. 4 the system matrix is kept in a compressed form and is never set up explicitly. The same publication also covers aspects of numerical stability and proposes an unwinding scheme based on trial and error. The attractiveness of the SHE method for the investigation of hot-carrier effects is reflected in publications on the inclusion of electron-electron scattering for first-order SHE [108,109], and by investigations of impact ionization [22] as well as hot-electron injections [77]. Singh [97] discussed the advantage of using inelastic scattering in order to avoid spurious oscillations in the distribution function and proved that the resulting system matrix for first-order SHE is an M -matrix, which ensures the positivity of the distribution function at the discrete level.

The number of publications on the SHE method by the engineering community declined towards the end of the 20th century. Instead, publications from mathematicians increased. Ben Abdallah [2] put the first-order SHE method in context with established moment-based methods and derived high-field approximations [3]. Ringhofer proposed various expansion approaches for the BTE based on entropy functionals [81–83] and proposed an expansion of the energy coordinate into Hermite polynomials [80]. Hansen *et al.* [36] analyzed the SHE method for plasma physics.

In the early 2000s, Goldsman *et al.* [26,35] applied a first-order SHE method to the modified Boltzmann equation taking contributions from the Wigner equation into account. The publication of Jungemann *et al.* [53] in 2006 applied the maximum entropy dissipation scheme developed by Ringhofer to a discretization in $(\mathbf{x}, \varepsilon)$ -space, where ε denotes kinetic energy, and put arbitrary order expansions on solid grounds by using a Galerkin scheme for the angular components. Furthermore, higher-order expansions were shown to be required for devices in the nanometer regime, a box-integration scheme suitable also for a certain class of unstructured grids was proposed, and the need for good preconditioners in order to obtain convergence of iterative solvers was discussed. Hong *et al.* [44] presented the first arbitrary-order implementation of the SHE method in two spatial dimensions in 2008, refined the numerical scheme in 2009 to cover magnetic fields, and re-introduced the H -transform in order to preserve numerical stability in the deca-nanometer regime [42]. A full-band SHE of the valence band was presented by Pham *et al.* [73]. Recently, Matz *et al.* [45,69] presented a fitted band structure for the conduction band for use with the SHE method, which further increases the accuracy of the SHE method, but at the expense of considerably increased computational costs. In 2011, Jin *et al.* [48] proposed a simplified method for the inclusion of full-band effects, which preserves the accuracy of the fitted band structure without notably increasing the computational effort. Hong *et al.* [43] also extended the SHE method to obey Pauli's exclusion principle, while Pham *et al.* [74–76] coupled the Schrödinger equation with a SHE method of reduced dimensionality for multi-subband solutions of PMOSFETs.

2.2 Derivation of the SHE Equations

The SHE equations are derived in the following. The calculations mostly follow those given by Jungemann *et al.* [53]. For reasons of clarity, function arguments are omitted whenever appropriate. Furthermore, the explicit inclusion of the Herring-Vogt transform as well as the inclusion of a magnetic field, which are detailed by Hong *et al.* [42], are avoided. For details on spherical harmonics the reader is referred to the literature [18, 20, 41], and for the particular phase factors used within this thesis to [86].

The derivation is carried out for an expansion of the distribution function $f(\mathbf{x}, \mathbf{k}, t)$ into spherical harmonics as in (2.1) on equi-energy surfaces, which requires that the mapping $(\varepsilon, \theta, \varphi) \mapsto \mathbf{k}$ is a bijection. For a given distribution function f , the expansion coefficients are obtained from projections:

$$\begin{aligned} f_{l,m}(\mathbf{x}, \varepsilon, t) &= \frac{2}{(2\pi)^3} \int_{\mathbb{B}} Y^{l,m}(\theta(\mathbf{k}), \varphi(\mathbf{k})) f(\mathbf{x}, \mathbf{k}, t) \delta(\varepsilon - \varepsilon(\mathbf{k})) d\mathbf{k}^3 \\ &= \int_{\Omega} Y^{l,m}(\theta, \varphi) f(\mathbf{x}, \mathbf{k}(\varepsilon, \theta, \varphi), t) Z(\varepsilon, \theta, \varphi) d\Omega \end{aligned} \quad (2.2)$$

Here, Ω denotes the unit sphere, and the generalized density of states including spin degeneracy in the absence of magnetic fields is given by

$$Z(\varepsilon, \theta, \varphi) = \frac{|\mathbf{k}|^2}{4\pi^3} \frac{\partial |\mathbf{k}|}{\partial \varepsilon}, \quad (2.3)$$

where a possible spatial dependence due to the use of different materials is ignored for the sake of conciseness. One should be careful when comparing generalized densities of states from different authors, because additional prefactors are in use.

It is important to keep in mind that the spherical harmonics are not orthogonal with respect to the bilinear form

$$(f, g)_e := \int_{\Omega} f g Z d\Omega, \quad (2.4)$$

unless the generalized density of states Z does not depend on the angles. For this reason, one may alternatively expand the generalized distribution function $g := fZ$ and use the standard inner product on the unit sphere, which is the approach taken by Jungemann *et al.* [53]. In the following, however, an expansion of f is carried out, but differences to an expansion with respect to g are pointed out on a regular basis.

One pitfall in the derivation of the SHE equations for an expansion of f is related to the representation (2.2) for a given distribution function f . The BTE is to be solved for an unknown distribution function f , hence $f_{l,m}$ is not obtained directly from a given function. Instead, the unknown distribution function f is expanded into spherical harmonics, which ultimately results in equations for the expansion coefficients $f_{l,m}$. Keeping in mind that the spherical harmonics are not necessarily orthogonal with respect to the bilinear form (2.4), there holds

$$\int_{\Omega} Y^{l,m} f Z d\Omega \simeq \int_{\Omega} Y^{l,m} \sum_{l',m'} f_{l',m'} Y^{l',m'} Z d\Omega = \sum_{l',m'} f_{l',m'} \int_{\Omega} Y^{l,m} Y^{l',m'} Z d\Omega, \quad (2.5)$$

which results in the expansion coefficient $f_{l,m}$ only in the case of a generalized density of states independent of the angles, i.e. $Z = Z(\varepsilon)$, but not for the general case of an angular dependency.

In order to derive a set of equations for the expansion coefficients $f_{l,m}$ for an unknown function f known to fulfill the BTE (1.1), one can proceed in two ways. The first possibility is to insert the expansion into the BTE and then project the resulting equation onto spherical harmonics, while the second possibility is to first project the BTE and then insert the expansion of f . Both operations are linear and the BTE itself is linear when using linear scattering operators only, thus both methods yield the same result provided that all required exchanges of summation and integration are valid. Since the latter method leads to less notational clutter, first a projection of the BTE onto each of the spherical harmonics $Y^{l,m}$ of the form

$$X \mapsto \frac{2}{(2\pi)^3} \int_{\mathbb{B}} XY^{l,m} \delta(\varepsilon - \varepsilon(\mathbf{k})) d\mathbf{k}^3 \quad (2.6)$$

is carried out. These projections onto $Y^{l,m}$ are detailed in the following term-by-term. Function arguments are usually suppressed to increase the legibility of the expressions.

- Term $\partial f / \partial t$: Since the time derivative can be pulled in front of the projection integral, one immediately obtains $\partial[f]_{l,m} / \partial t$, where

$$[f]_{l,m} := \int_{\Omega} Y^{l,m} f Z d\Omega \quad (2.7)$$

is in general different from the expansion coefficient $f_{l,m}$ as outlined above.

- Term $\mathbf{v} \cdot \nabla_{\mathbf{x}} f$: Similar to the previous term, the gradient with respect to the spatial coordinate \mathbf{x} can be pulled in front of the integral, thus leading to

$$\nabla_{\mathbf{x}} \cdot \int_{\Omega} Y^{l,m} \mathbf{v} f Z d\Omega . \quad (2.8)$$

It is convenient to associate the integral with the generalized current density

$$\mathbf{j}_{l,m}(\mathbf{x}, \varepsilon, t) = \int_{\Omega} Y^{l,m} \mathbf{v} f Z d\Omega . \quad (2.9)$$

- Term $\mathbf{F} / \hbar \cdot \nabla_{\mathbf{k}} f$: In contrast to the other terms, the derivative cannot be pulled out of the projection integral. Since the gradient with respect to the wavevector \mathbf{k} of the distribution function f would lead to problems for a separation of $f_{l',m'}$ and $Y^{l',m'}$ after inserting the expansion (2.1), an integration by parts is carried out. To avoid formal difficulties with the delta distribution, the projection is in addition first multiplied with a smooth test function $\psi(\varepsilon)$ and integrated over energy:

$$\begin{aligned} & \int_0^\infty \psi(\varepsilon) \frac{2}{(2\pi)^3} \int_{\mathbb{B}} \delta(\varepsilon - \varepsilon(\mathbf{k})) Y^{l,m} \frac{\mathbf{F}}{\hbar} \cdot \nabla_{\mathbf{k}} f d\mathbf{k} d\varepsilon \\ &= \frac{2\mathbf{F}}{(2\pi)^3 \hbar} \cdot \int_{\mathbb{B}} \psi(\varepsilon(\mathbf{k})) Y^{l,m} \nabla_{\mathbf{k}} f d\mathbf{k} \\ &= -\frac{2\mathbf{F}}{(2\pi)^3 \hbar} \cdot \int_{\mathbb{B}} \nabla_{\mathbf{k}} (\psi(\varepsilon(\mathbf{k})) Y^{l,m}) f d\mathbf{k} \\ &= -\frac{2\mathbf{F}}{(2\pi)^3 \hbar} \cdot \int_{\mathbb{B}} \left[\frac{\partial \psi}{\partial \varepsilon} \nabla_{\mathbf{k}} \varepsilon(\mathbf{k}) Y^{l,m} + \psi(\varepsilon(\mathbf{k})) \nabla_{\mathbf{k}} Y^{l,m} \right] f d\mathbf{k} \end{aligned}$$

The gradient in spherical coordinates $(|\mathbf{k}|, \theta, \varphi)$ in \mathbf{k} -space is given by

$$\nabla_{\mathbf{k}} Y_{l,m} = \frac{\partial Y_{l,m}}{\partial |\mathbf{k}|} \mathbf{e}_{|\mathbf{k}|} + \frac{1}{|\mathbf{k}|} \frac{\partial Y_{l,m}}{\partial \theta} \mathbf{e}_{\theta} + \frac{1}{|\mathbf{k}| \sin \theta} \frac{\partial Y_{l,m}}{\partial \varphi} \mathbf{e}_{\varphi}, \quad (2.10)$$

where $\mathbf{e}_{|\mathbf{k}|}$, \mathbf{e}_{θ} and \mathbf{e}_{φ} denote the unit vectors in $|\mathbf{k}|$, θ and φ -direction, respectively. The invariance of spherical harmonics with respect to the radial direction and the relation $\mathbf{v} = \nabla_{\mathbf{k}} \varepsilon / \hbar$ leads to

$$\begin{aligned} & \int_0^{\infty} \psi(\varepsilon) \frac{2}{(2\pi)^3} \int_{\mathbb{B}} \delta(\varepsilon - \varepsilon(\mathbf{k})) Y_{l,m} \frac{\mathbf{F}}{\hbar} \cdot \nabla_{\mathbf{x}} f \, d\mathbf{k} \, d\varepsilon \\ &= -\mathbf{F} \cdot \int_0^{\infty} \frac{\partial \psi}{\partial \varepsilon} \int_{\Omega} Y_{l,m} \mathbf{v} f Z \, d\Omega \, d\varepsilon \\ &\quad - \mathbf{F} \cdot \int_0^{\infty} \psi(\varepsilon) \int_{\Omega} \frac{1}{\hbar |\mathbf{k}|} \left(\frac{\partial Y_{l,m}}{\partial \theta} \mathbf{e}_{\theta} + \frac{1}{\sin \theta} \frac{\partial Y_{l,m}}{\partial \varphi} \mathbf{e}_{\varphi} \right) f Z \, d\Omega \, d\varepsilon \\ &= -\mathbf{F} \cdot \int_0^{\infty} \frac{\partial \psi}{\partial \varepsilon} \mathbf{j}_{l,m} + \psi \mathbf{\Gamma}_{l,m} \, d\varepsilon \\ &= \mathbf{F} \cdot \int_0^{\infty} \psi \left(\frac{\partial \mathbf{j}_{l,m}}{\partial \varepsilon} - \mathbf{\Gamma}_{l,m} \right) \, d\varepsilon, \end{aligned}$$

where the angular coupling term is given by

$$\mathbf{\Gamma}_{l,m} = \int_{\Omega} \frac{1}{\hbar |\mathbf{k}|} \left(\frac{\partial Y_{l,m}}{\partial \theta} \mathbf{e}_{\theta} + \frac{1}{\sin \theta} \frac{\partial Y_{l,m}}{\partial \varphi} \mathbf{e}_{\varphi} \right) f Z \, d\Omega. \quad (2.11)$$

Since the test function ψ can be taken ‘arbitrarily’, one obtains

$$\frac{2}{(2\pi)^3} \int_{\mathbb{B}} \delta(\varepsilon - \varepsilon(\mathbf{k})) Y_{l,m} \frac{\mathbf{F}}{\hbar} \cdot \nabla_{\mathbf{x}} f \, d\mathbf{k} = \mathbf{F} \cdot \left(\frac{\partial \mathbf{j}_{l,m}}{\partial \varepsilon} - \mathbf{\Gamma}_{l,m} \right). \quad (2.12)$$

- Term $Q\{f\}$: The scattering operator in the low-density approximation is considered, which neglects the nonlinearity introduced by Pauli’s exclusion principle:

$$Q\{f\} = \frac{1}{(2\pi)^3} \int_{\mathbb{B}} s(\mathbf{x}, \mathbf{k}', \mathbf{k}) f(\mathbf{x}, \mathbf{k}', t) - s(\mathbf{x}, \mathbf{k}, \mathbf{k}') f(\mathbf{x}, \mathbf{k}, t) \, d\mathbf{k}'. \quad (2.13)$$

Note that it is common to multiply the integral with a small sample volume V_s in front, which is then included in the denominator of the scattering rates. In this work, the sample volume V_s is not written explicitly. To allow for several different scattering processes like acoustical and optical phonon scattering, the index η is used for writing the scattering rate as

$$s(\mathbf{x}, \mathbf{k}, \mathbf{k}') = \sum_{\eta} \sigma_{\eta}(\mathbf{x}, \mathbf{k}, \mathbf{k}') \delta(\varepsilon(\mathbf{k}) - \varepsilon(\mathbf{k}') \pm \hbar \omega_{\eta}), \quad (2.14)$$

where the second and third arguments of s denote the initial and the final state respectively. The minus sign stands for emission of energy and the plus sign for absorption. In the case of multiple energy bands, summation over all energy bands has to be added to (2.14), cf. [53]. In the following only a single band is considered,

a generalization to multiple bands mainly consists of a summation over all energy bands involved.

The scattering integral is split into an in-scattering term

$$Q^{\text{in}}\{f\} = \frac{1}{(2\pi)^3} \int_{\mathbb{B}} s(\mathbf{x}, \mathbf{k}', \mathbf{k}) f(\mathbf{x}, \mathbf{k}', t) d\mathbf{k}' \quad (2.15)$$

and an out-scattering term

$$Q^{\text{out}}\{f\} = \frac{1}{(2\pi)^3} f(\mathbf{x}, \mathbf{k}, t) \int_{\mathbb{B}} s(\mathbf{x}, \mathbf{k}, \mathbf{k}') d\mathbf{k}' , \quad (2.16)$$

which are projected onto spherical harmonics one after another. Projection of the in-scattering term (2.15) yields

$$Q_{l,m}^{\text{in}}\{f\} = \frac{2}{(2\pi)^3} \int_{\mathbb{B}} \delta(\varepsilon - \varepsilon(\mathbf{k})) Y^{l,m} Q^{\text{in}}\{f\} d\mathbf{k} =: \sum_{\eta} Q_{\eta,l,m}^{\text{in}}\{f\} , \quad (2.17)$$

where

$$Q_{\eta,l,m}^{\text{in}}\{f\} = \int_{\Omega} Y^{l,m} Z \int_{\Omega} \sigma_{\eta}(\mathbf{x}, \mathbf{k}(\varepsilon \pm \hbar\omega_{\eta}, \theta', \varphi'), \mathbf{k}(\varepsilon, \theta, \varphi)) \times f(\mathbf{x}, \varepsilon \pm \hbar\omega_{\eta}, t) Z(\varepsilon \pm \hbar\omega_{\eta}, \theta', \varphi') d\Omega' d\Omega . \quad (2.18)$$

Similarly, the out-scattering term is evaluated as

$$Q_{l,m}^{\text{out}}\{f\} = \sum_{\eta} Q_{\eta,l,m}^{\text{out}}\{f\} , \quad (2.19)$$

where

$$Q_{\eta,l,m}^{\text{out}}\{f\} = \int_{\Omega} Y^{l,m} f Z \int_{\Omega} Z(\varepsilon \pm \hbar\omega_{\eta}, \theta', \varphi') \times \sigma_{\eta}(\mathbf{x}, \mathbf{k}(\varepsilon, \theta, \varphi), \mathbf{k}(\varepsilon \pm \hbar\omega_{\eta}, \theta', \varphi')) d\Omega' d\Omega . \quad (2.20)$$

A considerable simplification can be achieved if the transition rate is assumed to be *velocity randomizing*, i.e. the coefficient σ_{η} in (2.14) depends only on the initial and final energy, but not on the angles. This allows for rewriting (2.18) as

$$\begin{aligned} Q_{\eta,l,m}^{\text{in,VR}}\{f\} &= \sigma_{\eta}(\mathbf{x}, \varepsilon \pm \hbar\omega_{\eta}, \varepsilon) \int_{\Omega} Y^{l,m} Z d\Omega \int_{\Omega} f(\mathbf{x}, \varepsilon \pm \hbar\omega_{\eta}, t) Z(\varepsilon \pm \hbar\omega_{\eta}, \theta', \varphi') d\Omega' \\ &= \sigma_{\eta}(\mathbf{x}, \varepsilon \pm \hbar\omega_{\eta}, \varepsilon) Z_{l,m}(\varepsilon) \frac{[f(\mathbf{x}, \varepsilon \pm \hbar\omega_{\eta})]_{0,0}}{Y^{0,0}} , \end{aligned} \quad (2.21)$$

where (2.7) was used and $Z_{l,m}(\varepsilon)$ denotes the orthonormal projection of the generalized density of states onto the spherical harmonic $Y^{l,m}$ using the standard inner product on the sphere. In the case of spherical bands, $[f]_{0,0} = f_{0,0}Z$ and thus only $f_{0,0}$ is coupled into the balance equation for $l = m = 0$.

With the assumption of velocity-randomization, the out-scattering term can be simplified to

$$\begin{aligned} Q_{\eta,l,m}^{\text{out,VR}}\{f\} &= \sigma_{\eta}(\mathbf{x}, \varepsilon, \varepsilon \pm \hbar\omega_{\eta}) \times \int_{\Omega} Y^{l,m} f Z \, d\Omega \times \int_{\Omega} Z(\varepsilon \pm \hbar\omega_{\eta}, \theta, \varphi) \, d\Omega' \\ &= \sum_{\eta} \sigma_{\eta}(\mathbf{x}, \varepsilon, \varepsilon \pm \hbar\omega_{\eta}) [f]_{l,m} \frac{Z_{0,0}(\varepsilon \pm \hbar\omega_{\eta})}{Y^{0,0}}. \end{aligned} \quad (2.22)$$

Thus, the out-scattering term is proportional to $f_{l,m}$ in the case of a spherically symmetric density of states Z . If an expansion of the generalized distribution function $g = fZ$ is carried out instead of an expansion of f , then the out-scattering term is proportional to $g_{l,m}$ irrespective of any spherical symmetry of Z .

Summing up, the full projected scattering operator using velocity randomization (VR) is thus given by

$$\begin{aligned} Q_{l,m}^{\text{VR}}\{f\} &= \frac{1}{Y^{0,0}} \sum_{\eta} \left[Z_{l,m}(\varepsilon) \sigma_{\eta}(\mathbf{x}, \varepsilon \pm \hbar\omega_{\eta}, \varepsilon) [f(\mathbf{x}, \varepsilon \pm \hbar\omega_{\eta}, t)]_{0,0} \right. \\ &\quad \left. - [f]_{l,m}(\mathbf{x}, \varepsilon, t) \sigma_{\eta}(\mathbf{x}, \varepsilon, \varepsilon \mp \hbar\omega_{\eta}) Z_{0,0}(\varepsilon \mp \hbar\omega_{\eta}) \right]. \end{aligned} \quad (2.23)$$

Even though the scattering operator after projection is not an integral operator any longer, shifted arguments on the right hand side show up whenever inelastic collisions characterized by $\hbar\omega_{\eta} \neq 0$ are considered.

Collecting all individual terms, we obtain the system of equations for the BTE upon projection onto spherical harmonics on equi-energy surfaces under the assumption of velocity randomization:

$$\begin{aligned} \frac{\partial [f]_{l,m}}{\partial t} + \nabla_{\mathbf{x}} \cdot \mathbf{j}_{l,m}(\mathbf{x}, \varepsilon, t) + \mathbf{F} \cdot \left(\frac{\partial \mathbf{j}_{l,m}}{\partial \varepsilon} - \mathbf{\Gamma}_{l,m} \right) &= \\ = \frac{1}{Y^{0,0}} \sum_{\eta} \left[Z_{l,m}(\varepsilon) \sigma_{\eta}(\mathbf{x}, \varepsilon \pm \hbar\omega_{\eta}, \varepsilon) [f]_{0,0}(\mathbf{x}, \varepsilon \pm \hbar\omega_{\eta}, t) \right. \\ &\quad \left. - [f]_{l,m}(\mathbf{x}, \varepsilon, t) \sigma_{\eta}(\mathbf{x}, \varepsilon, \varepsilon \mp \hbar\omega_{\eta}) Z_{0,0}(\varepsilon \mp \hbar\omega_{\eta}) \right] \end{aligned} \quad (2.24)$$

It is worthwhile to note that an expansion of $g = fZ$ instead of f leads to the same system of equations when replacing $[f]$ with g .

2.3 *H-Transform and MEDS*

A discretization of the system (2.24) in $(\mathbf{x}, \varepsilon)$ -space leads to spurious oscillations for very small devices, because the grid is not aligned with the trajectories of carriers in free flight. The numerical stability can be improved substantially by a transformation from kinetic energy ε to total energy H , because trajectories are then given by $H = \text{const}$. The price to pay for the increased numerical stability is the additional effort for handling the band-edge given by $\varepsilon = 0$, because the simulation domain needs to be adjusted with every update of the electrostatic potential.

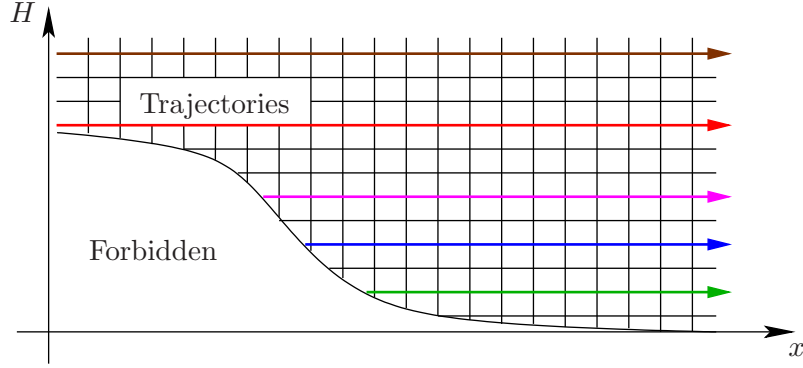


Figure 2.1: Trajectories of carriers in free flight within the device are given by constant total energy H .

The H -transform was suggested already soon after the SHE method had been introduced [23]. In the following, the application of the H -transform to (2.24) in the way proposed by [42] is shown. Consider a variable transformation from $(\mathbf{x}, \varepsilon)$ to $(\tilde{\mathbf{x}}, H)$ by

$$\tilde{\mathbf{x}} = \mathbf{x} , \quad H = \varepsilon + q\Psi(\mathbf{x}) , \quad (2.25)$$

where $\Psi(\mathbf{x})$ can be an arbitrary function of \mathbf{x} and q is the signed charge of the carrier. The system (2.24) is then transformed to

$$\begin{aligned} \frac{\partial [f]_{l,m}}{\partial t} + \nabla_{\tilde{\mathbf{x}}} \cdot \mathbf{j}_{l,m} + [\mathbf{F} + \nabla_{\mathbf{x}} H] \cdot \frac{\partial \mathbf{j}_{l,m}}{\partial H} - \mathbf{F} \cdot \boldsymbol{\Gamma}_{l,m} \\ = \frac{1}{Y_{0,0}} \sum_{\eta} \left[Z_{l,m} \sigma_{\eta}(\tilde{\mathbf{x}}, H \pm \hbar\omega_{\eta}, H) [f]_{0,0}(\tilde{\mathbf{x}}, H \pm \hbar\omega_{\eta}, t) \right. \\ \left. - [f]_{l,m} \sigma_{\eta}(\tilde{\mathbf{x}}, H, H \mp \hbar\omega_{\eta}) Z_{0,0}(H \mp \hbar\omega_{\eta}) \right] . \end{aligned} \quad (2.26)$$

Since the force term is given by

$$\mathbf{F} = -\nabla_{\mathbf{x}} [E_c(\mathbf{x}) + q\psi(\mathbf{x})] , \quad (2.27)$$

where E_c is the position-dependent valley minimum and ψ the electrostatic potential, the derivative of $\mathbf{j}_{l,m}$ with respect to H is eliminated by the choice

$$\Psi(\mathbf{x}) = \psi(\mathbf{x}) + \frac{E_c(\mathbf{x})}{q} . \quad (2.28)$$

This particular choice of Ψ implies that H refers to the total energy. The H -transformed system is thus given by

$$\begin{aligned} \frac{\partial [f]_{l,m}}{\partial t} + \nabla_{\mathbf{x}} \cdot \mathbf{j}_{l,m} - \mathbf{F} \cdot \boldsymbol{\Gamma}_{l,m} = \frac{1}{Y_{0,0}} \sum_{\eta} \left[Z_{l,m} \sigma_{\eta}(\mathbf{x}, H \pm \hbar\omega_{\eta}, H) [f]_{0,0}(\mathbf{x}, H \pm \hbar\omega_{\eta}, t) \right. \\ \left. - [f]_{l,m} \sigma_{\eta}(\mathbf{x}, H, H \mp \hbar\omega_{\eta}) Z_{0,0}(H \mp \hbar\omega_{\eta}) \right] , \end{aligned} \quad (2.29)$$

where \mathbf{x} is written instead of $\tilde{\mathbf{x}}$.

Inserting the expansion (2.1) into (2.29) yields

$$\begin{aligned} [Y^{l',m'}]_{l,m} \frac{\partial f_{l',m'}}{\partial t} + \nabla_{\mathbf{x}} \cdot \mathbf{j}_{l,m}^{l',m'} f_{l',m'} - \mathbf{F} \cdot \mathbf{\Gamma}_{l,m}^{l',m'} f_{l',m'} \\ = \frac{1}{Y_{0,0}} \sum_{\eta} \left[Z_{l,m} \sigma_{\eta}(\mathbf{x}, H \pm \hbar\omega_{\eta}, H) [Y^{l',m'}]_{0,0} f_{l',m'}(\mathbf{x}, H \pm \hbar\omega_{\eta}, t) \right. \\ \left. - [Y^{l',m'}]_{l,m} f_{l',m'} \sigma_{\eta}(\mathbf{x}, H, H \mp \hbar\omega_{\eta}) Z_{0,0}(H \mp \hbar\omega_{\eta}) \right], \end{aligned} \quad (2.30)$$

where Einstein's summation convention over pairs of upper and lower indices is employed. The coefficients

$$[Y^{l',m'}]_{l,m} := \int_{\Omega} Y^{l,m} Y^{l',m'} Z \, d\Omega, \quad (2.31)$$

$$\mathbf{j}_{l,m}^{l',m'} := \int_{\Omega} Y^{l,m} \mathbf{v} Y^{l',m'} Z \, d\Omega, \quad (2.32)$$

$$\mathbf{\Gamma}_{l,m}^{l',m'} := \int_{\Omega} \frac{1}{\hbar|\mathbf{k}|} \left(\frac{\partial Y^{l,m}}{\partial \theta} \mathbf{e}_{\theta} + \frac{1}{\sin \theta} \frac{\partial Y^{l,m}}{\partial \varphi} \mathbf{e}_{\varphi} \right) Y^{l',m'} Z \, d\Omega \quad (2.33)$$

determine the coupling between the different equations and will be thoroughly investigated in Chap. 4.

The even part of the carrier distribution function can be associated with densities like the carrier density or the energy density, while the odd part of the carrier distribution function is viewed as fluxes. To improve numerical stability, these fluxes need to be stabilized [82]. Based on entropy dissipation principles, Ringhofer proposed to multiply the projected SHE equations with the entropy function $\exp(H/(k_{\text{B}}T_{\text{L}}))$, where k_{B} is the Boltzmann constant and T_{L} denotes lattice temperature, and to take the negative adjoint form of the projected equations for odd l [82]. While the multiplication with the entropy function is crucial for a formulation based on kinetic energy as in (2.24) and [53], it is just a constant factor in a formulation based on total energy such as (2.30). Therefore, it is sufficient to simply take the negative adjoint operator [42]:

$$\begin{aligned} l \text{ even: } [Y^{l',m'}]_{l,m} \frac{\partial f_{l',m'}}{\partial t} + \nabla_{\mathbf{x}} \cdot (\mathbf{j}_{l,m}^{l',m'} f_{l',m'}) - \mathbf{F} \cdot \mathbf{\Gamma}_{l,m}^{l',m'} f_{l',m'} \\ = \frac{1}{Y_{0,0}} \sum_{\eta} \left[Z_{l,m} \sigma_{\eta}(\mathbf{x}, H \pm \hbar\omega_{\eta}, H) [Y^{l',m'}]_{0,0} f_{l',m'}(\mathbf{x}, H \pm \hbar\omega_{\eta}, t) \right. \\ \left. - [Y^{l',m'}]_{l,m} f_{l',m'} \sigma_{\eta}(\mathbf{x}, H, H \mp \hbar\omega_{\eta}) Z_{0,0}(H \mp \hbar\omega_{\eta}) \right], \end{aligned} \quad (2.34)$$

$$\begin{aligned} l \text{ odd: } [Y^{l',m'}]_{l,m} \frac{\partial f_{l',m'}}{\partial t} + \mathbf{j}_{l,m}^{l',m'} \cdot \nabla_{\mathbf{x}} f_{l',m'} + \mathbf{F} \cdot \hat{\mathbf{\Gamma}}_{l,m}^{l',m'} f_{l',m'} \\ = \frac{1}{Y_{0,0}} \sum_{\eta} \left[Z_{l,m} \sigma_{\eta}(\mathbf{x}, H \pm \hbar\omega_{\eta}, H) [Y^{l',m'}]_{0,0} f_{l',m'}(\mathbf{x}, H \pm \hbar\omega_{\eta}, t) \right. \\ \left. - [Y^{l',m'}]_{l,m} f_{l',m'} \sigma_{\eta}(\mathbf{x}, H, H \mp \hbar\omega_{\eta}) Z_{0,0}(H \mp \hbar\omega_{\eta}) \right], \end{aligned} \quad (2.35)$$

where Einstein's summation convention over pairs of upper and lower indices is employed. The coupling coefficients $[Y^{l',m'}]_{l,m}$ and $\tilde{\mathbf{j}}_{l,m}^{l',m'}$ are self-adjoint and thus unchanged, while $\hat{\Gamma}_{l,m}^{l',m'}$ is given by

$$\hat{\Gamma}_{l,m}^{l',m'} := \Gamma_{l',m'}^{l,m} = \int_{\Omega} \frac{1}{\hbar|\mathbf{k}|} \left(\frac{\partial Y^{l',m'}}{\partial \theta} \mathbf{e}_{\theta} + \frac{1}{\sin \theta} \frac{\partial Y^{l',m'}}{\partial \varphi} \mathbf{e}_{\varphi} \right) Y^{l,m} Z \, d\Omega . \quad (2.36)$$

This stabilization scheme is commonly referred to as *maximum entropy dissipation scheme* (MEDS) [42, 53].

It is worthwhile to compare (2.34) and (2.35) with the system obtained from an expansion of

$$g(\mathbf{x}, \mathbf{k}, t) = f(\mathbf{x}, \mathbf{k}, t) Z(\mathbf{k}) = \sum_{l=0}^{\infty} \sum_{m=-l}^l g_{l,m}(\mathbf{x}, H, t) Y^{l,m}(\theta, \varphi) , \quad (2.37)$$

which is obtained for even l after repeating the previous steps as

$$\begin{aligned} \frac{\partial g_{l,m}}{\partial t} + \nabla_{\mathbf{x}} \cdot \tilde{\mathbf{j}}_{l,m}^{l',m'} g_{l',m'} - \mathbf{F} \cdot \tilde{\Gamma}_{l,m}^{l',m'} g_{l',m'} \\ = \frac{1}{Y_{0,0}} \sum_{\eta} \left[Z_{l,m} \sigma_{\eta}(\mathbf{x}, H \pm \hbar\omega_{\eta}, H) g_{0,0}(\mathbf{x}, H \pm \hbar\omega_{\eta}, t) \right. \\ \left. - g_{l,m} \sigma_{\eta}(\mathbf{x}, H, H \mp \hbar\omega_{\eta}) Z_{0,0}(H \mp \hbar\omega_{\eta}) \right] \end{aligned} \quad (2.38)$$

with coupling coefficients

$$\tilde{\mathbf{j}}_{l,m}^{l',m'} = \int_{\Omega} Y^{l,m} \mathbf{v} Y^{l',m'} \, d\Omega , \quad (2.39)$$

$$\tilde{\Gamma}_{l,m}^{l',m'} = \int_{\Omega} \frac{1}{\hbar|\mathbf{k}|} \left(\frac{\partial Y^{l,m}}{\partial \theta} \mathbf{e}_{\theta} + \frac{1}{\sin \theta} \frac{\partial Y^{l,m}}{\partial \varphi} \mathbf{e}_{\varphi} \right) Y^{l',m'} \, d\Omega . \quad (2.40)$$

The equations for odd l are obtained in the same way by taking the negative adjoint form. If the density of states Z does not show an angular dependence, the two approaches are equivalent, otherwise the truncated expansions will yield different results in general. To the knowledge of the author, a systematic comparison of the formulations (2.34) and (2.35) with (2.38) for nonspherical energy bands has not been carried out yet.

The system (2.34) and (2.35) consists of an infinite number of equations due to an expansion of f of the form (2.1). The conforming Galerkin procedure for obtaining a finite set of equations is to consider a truncated expansion

$$f(\mathbf{x}, \mathbf{k}, t) = \sum_{l=0}^L \sum_{m=-l}^l f_{l,m}(\mathbf{x}, H, t) Y^{l,m}(\theta, \varphi) , \quad (2.41)$$

for a reasonable maximum (finite) expansion order L , and to consider only a finite subset of the projected equations. The typical choice $l = 0, \dots, L$ and $m = -l, \dots, l$ for the projected equations is used in the remainder of this thesis, hence the number of unknown expansion coefficients and the number of equations agree. Otherwise, approximations in the least-squares sense for the over- or under-determined system would have to be considered. However, least-squares problems lead to additional computational effort compared to the solution of a linear system, thus no investigations have been carried out in that direction yet.

2.4 Self-Consistency with Poisson's Equation

So far, the force term \mathbf{F} has been considered to be a given quantity. In a homogeneous material it is linked to the electrostatic potential ψ by $\mathbf{F} = q\mathbf{E} = -q\nabla_{\mathbf{x}}\psi$, where q denotes the signed charge of the particle and \mathbf{E} the electric field. With Gauss' Law, a scalar permittivity ϵ and the charge density $|q|(p - n + C)$, where p and n denote the density of holes and electrons respectively, and C refers to the density of fixed charges in the material, the Poisson equation

$$-\Delta_{\mathbf{x}}\psi = \frac{|q|}{\epsilon}(p - n + C) \quad (2.42)$$

is obtained.

Since the carrier density depends on the solution of the BTE, which in turn depends on the solution of the Poisson equation, a self-consistent solution of both equations has to be found. Even though both equations are linear in their unknowns, the coupling is nonlinear due to the inner product of the force \mathbf{F} with the gradient $\nabla_{\mathbf{k}}f$ of the distribution function with respect to the wave vector \mathbf{k} . Consequently, a nonlinear iteration scheme has to be employed for the solution of the coupled system

$$-\Delta_{\mathbf{x}}\psi = \frac{|q|}{\epsilon}(p - n + C) , \quad (2.43)$$

$$L_{l,m}\{f\} = Q_{l,m}\{f\} , \quad l = 0, \dots, L, m = -l, \dots, l , \quad (2.44)$$

$$\nabla_{\mathbf{x}} \cdot (-D_p \nabla_{\mathbf{x}} p + p\mu_p \nabla_{\mathbf{x}} \psi) = 0 , \quad (2.45)$$

where electrons are treated by the SHE method, and holes are considered by a continuity equation without recombination. For the simulation of devices based on unipolar operation, the hole continuity equation is often neglected. A similar system is obtained if the SHE method is employed for holes and a continuity equation is used for electrons. Note that in the cases where a unipolar simulation is sufficient, the continuity equation is often neglected.

2.4.1 Gummel Iteration

Given the iterates $\psi^{(k)}$, $n^{(k)}$ and $p^{(k)}$ for the potential, electron and hole density respectively, updates can be obtained by solving the equations (2.43), (2.44), and (2.45) sequentially in a Gauss-Seidel-type manner [32]:

Algorithm 1 (Simplest Form of Gummel Iteration). *Input: Initial guesses $\psi^{(0)}$, $n^{(0)}$ and $p^{(0)}$, $k = 0$.*

(i) *Solve the Poisson equation (2.43) for $\psi^{(k+1)}$ using $n^{(k)}$ and $p^{(k)}$.*

(ii) *Solve the SHE equations (2.44) for $n^{(k+1)}$ using $\psi^{(k+1)}$.*

(iii) *Solve the hole continuity equation (2.45) for $p^{(k+1)}$ using $\psi^{(k+1)}$.*

(iv) *Stop if $(\psi^{(k+1)}, n^{(k+1)}, p^{(k+1)})$ is sufficiently accurate.*

(v) *Set $k \leftarrow k + 1$ and repeat.*

In its simplest form, the Gummel iteration diverges in most cases due to the exponential dependence of the carrier concentrations on the potential.

The convergence behavior can be improved substantially by considering the dependencies $n = n(\psi) = n_i \exp((\psi - \varphi_n)/V_T)$ and $p = p(\psi) = n_i \exp(-(\psi - \varphi_p)/V_T)$, where φ_n and φ_p denote the quasi-Fermi potentials of electrons and holes respectively and $V_T = |q|/(k_B T)$ is the thermal voltage. A linearization leads to the damped Poisson equation for $\delta\psi^{(k)} = \psi^{(k+1)} - \psi^{(k)}$:

$$-\Delta\delta\psi^{(k)} + \frac{n+p}{V_T}\delta\psi^{(k)} = \Delta\psi^{(k)} + \frac{|q|}{\epsilon}(p-n+C). \quad (2.46)$$

Consequently, the modified Gummel iteration is obtained as follows:

Algorithm 2 (Modified Gummel Iteration). *Input: Initial guesses $\psi^{(0)}$, $n^{(0)}$ and $p^{(0)}$, $k = 0$, $\alpha > 0$*

- (i) Solve (2.46) for $\delta\psi^{(k)}$ using $n^{(k)}$ and $p^{(k)}$.
- (ii) Set $\psi^{(k+1)} = \psi^{(k)} + \alpha\delta\psi^{(k)}$
- (iii) Solve the SHE equations (2.44) for $n^{(k+1)}$ using $\psi^{(k+1)}$.
- (iv) Solve the hole continuity equation (2.45) for $p^{(k+1)}$ using $\psi^{(k+1)}$.
- (v) Stop if $(\psi^{(k+1)}, n^{(k+1)}, p^{(k+1)})$ is sufficiently accurate.
- (vi) Set $k \leftarrow k + 1$ and repeat.

The damping parameter α allows for additional control of the damping. Typical values are about 0.5 and may be chosen differently for each iteration. In order to ensure a reduction of the residual, an additional control of α can be employed, where e.g. subsequent trials $\alpha_i = 2^{-i}$ for $i = 1, 2, \dots$ are chosen until the residual in the current step is reduced [16].

A typical convergence plot for an undamped modified Gummel iteration ($\alpha = 1$) is depicted in Fig. 2.2. Typical features are the almost constant potential update during the first iterations, and the nonuniform reduction of the potential correction in later iteration steps. These features are more pronounced for more complicated devices under higher bias.

2.4.2 Newton's Method

The standard method for the solution of nonlinear systems of equation is Newton's method. The big advantage over many other methods is the quadratic convergence sufficiently close to the true solution. For a system of equations of the form

$$\mathbf{G}(\mathbf{x}) = \begin{pmatrix} g_1(x_1, x_2, \dots, x_N) \\ g_2(x_1, x_2, \dots, x_N) \\ \vdots \\ g_N(x_1, x_2, \dots, x_N) \end{pmatrix} = \mathbf{0}, \quad (2.47)$$

the update of a guess $\mathbf{x}^{(k)}$ to the true solution is determined by

$$\mathbf{x}^{(k+1)} = \mathbf{x}^{(k)} - \mathbf{J}_{\mathbf{G}}^{-1}\mathbf{G}(\mathbf{x}^{(k)}). \quad (2.48)$$

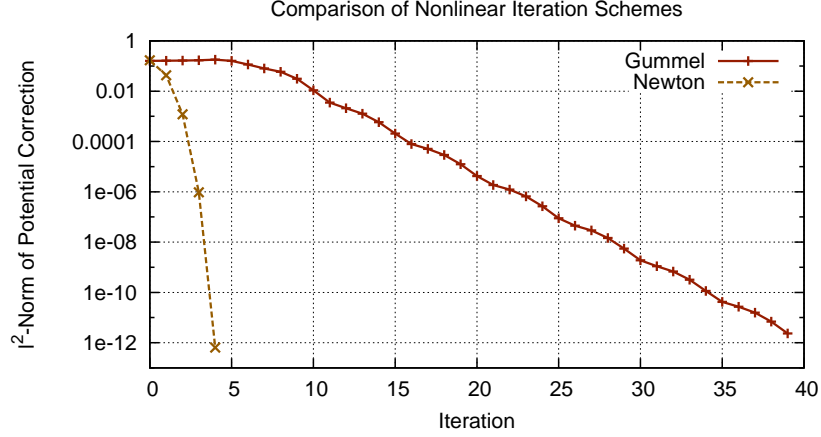


Figure 2.2: Comparison of the typical convergence of an undamped modified Gummel scheme and an undamped Newton scheme for the simulation of a one-dimensional n^+nm^+ -diode.

The Jacobian matrix $\mathbf{J}_{\mathbf{G}}$ of \mathbf{G} is given by

$$\mathbf{J}_{\mathbf{G}} = \begin{pmatrix} \frac{\partial g_1}{\partial x_1} & \frac{\partial g_1}{\partial x_2} & \cdots & \frac{\partial g_1}{\partial x_N} \\ \frac{\partial g_2}{\partial x_1} & \frac{\partial g_2}{\partial x_2} & \cdots & \frac{\partial g_2}{\partial x_N} \\ \vdots & \vdots & \ddots & \vdots \\ \frac{\partial g_N}{\partial x_1} & \frac{\partial g_N}{\partial x_2} & \cdots & \frac{\partial g_N}{\partial x_N} \end{pmatrix}. \quad (2.49)$$

Consequently, every Newton step requires the solution of a system of linear equations and the evaluation of the residual $\mathbf{G}(\mathbf{x}^{(k)})$. The method fails if the Jacobian matrix does not have full rank, which is, however, unlikely in practice due to the regularizing effect of round-off errors.

A Newton method for the system (2.43)-(2.45) can be derived by writing the system in the form

$$-\Delta_{\mathbf{x}}\psi - \frac{|q|}{\epsilon}(p - n + C) = 0 =: g_1(\psi, \mathbf{f}, p), \quad (2.50)$$

$$L_{l,m}\{f\} - Q_{l,m}\{f\} = 0 =: g_2(\psi, \mathbf{f}, p), \quad l = 0, \dots, L, m = -l, \dots, l, \quad (2.51)$$

$$\nabla_{\mathbf{x}} \cdot (-D_p \nabla_{\mathbf{x}} p + p \mu_p \nabla_{\mathbf{x}} \psi) = 0 =: g_3(\psi, \mathbf{f}, p), \quad (2.52)$$

with $\mathbf{f} = (f_{0,0}, f_{1,-1}, f_{1,0}, \dots, f_{L,L})^T$ for some maximum expansion order L . The Jacobian matrix is then obtained as

$$\begin{pmatrix} -\Delta_{\mathbf{x}} & (1/V_T + |q|/\epsilon)\partial n/\partial \mathbf{f} & 1/V_T - |q|/\epsilon \\ \partial(L_{l,m} - Q_{l,m})/\partial \psi & L_{l,m}\{\cdot\} - Q_{l,m}\{\cdot\} & 0 \\ \nabla_{\mathbf{x}} \cdot p \nabla_{\mathbf{x}} & 0 & \nabla_{\mathbf{x}} \cdot (-D_p \nabla_{\mathbf{x}} + \mu_p \nabla_{\mathbf{x}} \psi) \end{pmatrix}. \quad (2.53)$$

Here, two terms need additional considerations:

- $\partial n/\partial \mathbf{f}$: The electron density is obtained from the distribution function as

$$n = \int_0^\infty \int_{\Omega} f Z \, d\Omega \, d\varepsilon, \quad (2.54)$$

hence the derivatives with respect to the expansion coefficients are given by

$$\frac{\partial n}{\partial f_{l,m}} = \int_0^\infty \int_\Omega Y^{l,m} Z \, d\Omega \, d\varepsilon . \quad (2.55)$$

In the case that Z does not show an angular dependence, a nonzero derivative is obtained for $f_{0,0}$ only.

- $\partial(L_{l,m} - Q_{l,m})/\partial\psi$: Here, the derivative of the SHE equations (2.34) and (2.35) with respect to the potential ψ need to be taken. Since most terms depend on the kinetic energy ε , which for a fixed total energy H depends on the potential ψ , the derivative is very elaborate. For the sake of brevity, only the derivative of the generalized current density term $\mathbf{j}_{l,m}$ is outlined explicitly:

$$\frac{\partial \mathbf{j}_{l,m}(\varepsilon)}{\partial \psi} = \frac{\partial \mathbf{j}_{l,m}}{\partial \varepsilon} \frac{\partial \varepsilon}{\partial \psi} = -q \frac{\partial \mathbf{j}_{l,m}}{\partial \varepsilon} , \quad (2.56)$$

where it should be noted that q refers to the signed charge of the carrier. In the same way derivatives of the terms $f_{l,m}$, $\mathbf{\Gamma}_{l,m}$ and Z are computed. The force term is handled in the same way as for the hole continuity equation. For the case that no analytical expression for $\mathbf{j}_{l,m}$, $\mathbf{\Gamma}_{l,m}$ or Z is available, a discrete differential quotient is taken.

In practice, the Newton scheme will be used together with a damping scheme similar to the one discussed for the Gummel iteration. The existence of a damping parameter α_i leading to a reduction of the overall residual norm is ensured under reasonable assumptions about the system of equations.

An exemplary convergence plot for the Newton method is given in Fig. 2.2. The quadratic convergence is readily visible and leads to a much smaller number of iterations compared to the modified Gummel method.

2.5 Compatibility with Modern TCAD

Now as the SHE equations are derived, the state-of-the-art for the SHE method – excluding the author’s own contributions presented in the remainder of this thesis – is compared to the requirements for modern TCAD established in Sec. 1.2.

- **Accuracy:** The main rationale for the introduction of the deterministic SHE method was the ability to compute solutions of the full BTE instead of simpler macroscopic equations obtained from moments of the BTE. Moreover, the SHE method has been shown e.g. by Hennacy *et al.* [37] or Jungemann *et al.* [53] to yield results in agreement with those obtained from the Monte Carlo method, which is commonly considered to be the reference for all macroscopic models. Therefore, SHE easily fulfills the requirement for accuracy in modern TCAD.
- **Charge Conservation:** The box integration scheme proposed by Jungemann *et al.* [53] and later refined by Hong *et al.* [42] ensures current conservation by construction.
- **Self-Consistency:** As discussed in Sec. 2.4, the SHE equations are solved self-consistently with the Poisson equation. The convergence behavior is similar to that of the drift-diffusion model.

- **Resolution of Complicated Domains:** Except for the use of spatially triangular grids for first-order SHE [105], publications on the SHE method have relied on structured grids so far. For one-dimensional simulations, this is clearly not a concern. However, the first two-dimensional higher-order SHE simulations have been reported just recently in 2008 by Hong *et al.* [44] on structured grids. Even though the discretization scheme is in principle suitable for unstructured grids, no results have been reported by then. Nevertheless, a commercial implementation of a SHE simulator using triangular grids became available from Synopsys Inc. in 2011.
- **Computational Resources:** The SHE method imposes high memory requirements due to the additional energy coordinate. Memory consumptions in the range of 25 Gigabytes were reported for a third-order SHE simulation of a spatially two-dimensional simulation of a SiGe HBT [42], leading to single-threaded execution times of several hours. While execution times are still well below those of the Monte Carlo method, they prohibit parametric studies within a reasonable amount of time, as well as time-dependent simulations. Moreover, the parallelization of the SHE method has not been investigated so far, while fully parallel Monte Carlo simulators are already available [114]. Consequently, improvements from the numerics point of view as well as from the scientific computing point of view are required to make the SHE method attractive of modern TCAD.
- **Extendibility:** Due to the formulation by means for partial differential equations, the SHE method can be extended in a similar way as the drift-diffusion method. For example, the inclusion of magnetic fields has been proposed by Hong *et al.* [42]. Except for carrier-carrier scattering, for which a scheme is proposed in Sec. 3.4, the different scattering operators used with the Monte Carlo method have also been employed for the SHE method [46]. Thus, the SHE method fully complies to the requirements of modern TCAD in terms of extendibility.

The issues raised in terms of the resolution of complicated domains as well as in the use of computational resources will be addressed in the remainder of this thesis. Chap. 5 discusses the use of unstructured triangular and tetrahedral meshes for the SHE method. Chap. 6 addresses the quadratically increasing computational costs of the SHE method with the expansion order L . In Chap. 7 a parallel preconditioner is developed, which enables the efficient use of modern many- and multi-core computing architectures.

Chapter 3

Physical Modeling

The SHE equations (2.34) and (2.35) incorporate material-specific properties by the velocity term \mathbf{v} , the modulus $|\mathbf{k}|$ of the wave vector as a function of energy, the generalized density of states Z , and the scattering operator Q . However, the velocity term \mathbf{v} and the density of states Z are not independent and depend on the dispersion relation $\varepsilon(\mathbf{k})$ by

$$\mathbf{v} = \frac{1}{\hbar} \nabla_{\mathbf{k}} \varepsilon , \quad (3.1)$$

$$Z(\varepsilon, \theta, \varphi) = \frac{|\mathbf{k}|^2}{4\pi^3} \frac{\partial |\mathbf{k}|}{\partial \varepsilon} . \quad (2.3)$$

Similarly, the modulus of the wave vector is obtained from inverting the dispersion relation. Consequently, the choice of the dispersion relation plays a central role for the accuracy of the SHE method. Spherically symmetric approximations are presented in Sec. 3.1, but only poor approximations are obtained at higher energies. Sec. 3.2 deals with the state-of-the-art on the inclusion of full-band effects up to high energies.

The second half of this chapter is devoted to the various scattering effects. Since scattering balances the energy gain of carriers due to the electric field, accurate expressions for the scattering operators are mandatory. Scattering mechanisms leading to a linear operator are discussed in Sec. 3.3, while the case of nonlinear scattering operators is investigated in Sec. 3.4.

3.1 Spherically Symmetric Energy Band Models

Due to the nonuniformity of the crystal lattice in silicon with respect to a change in direction, the dispersion relation linking the particle momentum with the particle energy cannot be accurately described by the idealized setting of an infinitely deep quantum well, for which the solution of Schrödinger's equation yields a parabolic dependence of the energy on the wave vector:

$$\varepsilon(\mathbf{k}) = \frac{\hbar^2 |\mathbf{k}|^2}{2m^*} , \quad (3.2)$$

where \hbar is the scaled Planck constant and m^* is the effective mass. Still, this quadratic relationship termed *parabolic band approximation* is a good approximation near the minimum of the energy valley. Due to its simple analytical form, the parabolic dispersion relation is

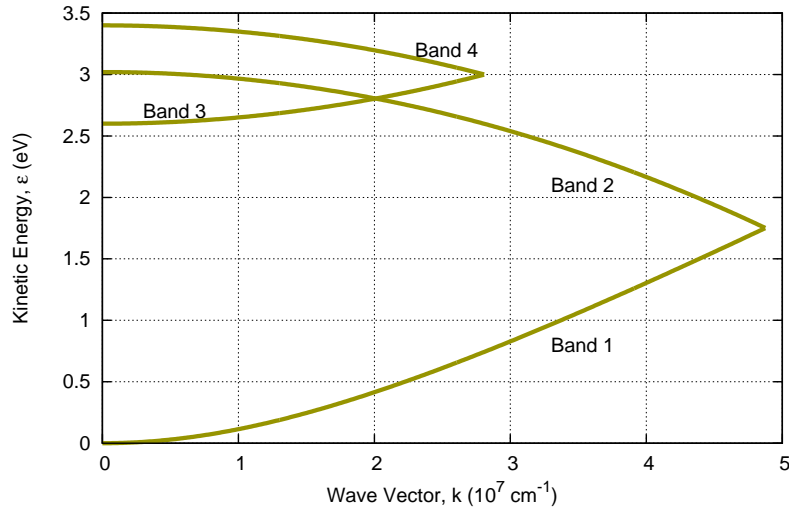


Figure 3.1: Multi-band structure of silicon. Bands 1 and 3 are electron-like (increasing density of states), bands 2 and 4 are hole-like (decreasing density of states).

often used up to high energies, for which it fails to provide an accurate description of the material.

A more accurate approximation to the band structure in silicon can be obtained by a slight modification of the form

$$\gamma(\varepsilon) = \frac{\hbar^2 \mathbf{k}^2}{2m^*}, \quad (3.3)$$

where the typical choice

$$\gamma(\varepsilon) = \varepsilon(1 + \alpha\varepsilon) \quad (3.4)$$

is known as *Kane's model* [55]. The parameter α is called *nonparabolicity factor*; in the case $\alpha = 0$ one obtains again (3.2). More complicated analytical dependencies of the energy on the wave vector are certainly possible, but (3.4) already provides very good results in the low-energy regime. The choice $\alpha = 0.5$ provides a good approximation of the dispersion relation for electrons in relaxed silicon. However, for kinetic energies above 1.75 eV the nonparabolic approximation fails to describe the nonmonotonicity of the density of states in silicon.

The deficiencies of the nonparabolic dispersion relation can be mitigated by a combination of four energy bands as proposed by Brunetti et. al. [11]:

$$\varepsilon + \alpha\varepsilon^2 = \frac{\hbar^2 \mathbf{k}^2}{2m^{*(1)}}, \quad (\text{Band 1}) \quad (3.5)$$

$$\varepsilon = \varepsilon_{\max}^{(2)} - \frac{\hbar^2 \mathbf{k}^2}{2m^{*(2)}}, \quad (\text{Band 2}) \quad (3.6)$$

$$\varepsilon = \varepsilon_{\min}^{(3)} + \frac{\hbar^2 \mathbf{k}^2}{2m^{*(3)}}, \quad (\text{Band 3}) \quad (3.7)$$

$$\varepsilon = \varepsilon_{\max}^{(4)} - \frac{\hbar^2 \mathbf{k}^2}{2m^{*(4)}}. \quad (\text{Band 4}) \quad (3.8)$$

Band	m^*/m_0	ε_{\min}	ε_{\max}	β	α
1	0.320	0	1.75	6	0.35
2	0.712	1.75	3.02	6	0
3	0.750	2.60	3.00	12	0
4	0.750	3.00	3.40	12	0

Table 3.1: Parameters for the analytical band structure proposed by Brunetti et. al. [11]. m_0 denotes the electron mass, β the multiplicity of the respective band and α is the nonparabolicity factor. Each band extends from ε_{\min} to ε_{\max} .

The bands are valid up to energy limits $\varepsilon_{\max}^{(2)}$, $\varepsilon_{\min}^{(3)}$ and $\varepsilon_{\max}^{(4)}$ respectively. The specific form of each band is given by

$$\gamma^{(1)}(\varepsilon) = \varepsilon + \alpha\varepsilon^2, \quad (\text{Band 1}) \quad (3.9)$$

$$\gamma^{(2)}(\varepsilon) = \varepsilon_{\max}^{(2)} - \varepsilon, \quad (\text{Band 2}) \quad (3.10)$$

$$\gamma^{(3)}(\varepsilon) = \varepsilon - \varepsilon_{\min}^{(3)}, \quad (\text{Band 3}) \quad (3.11)$$

$$\gamma^{(4)}(\varepsilon) = \varepsilon_{\max}^{(4)} - \varepsilon. \quad (\text{Band 4}) \quad (3.12)$$

The relationships between the energy and the wave vector can be written in compact form as

$$\gamma^{(\nu)}(\varepsilon) = \frac{\hbar^2 \mathbf{k}^2}{2m^{*(\nu)}}, \quad \nu = 1, 2, 3, 4, \quad (3.13)$$

and are depicted in Fig. 3.1. The total density of states $Z(\varepsilon)$ is computed from the individual densities of states by a weighted sum:

$$Z(\varepsilon) = \beta^{(1)}Z^{(1)}(\varepsilon) + \beta^{(2)}Z^{(2)}(\varepsilon) + \beta^{(3)}Z^{(3)}(\varepsilon) + \beta^{(4)}Z^{(4)}(\varepsilon), \quad (3.14)$$

where the *band multiplicities* $\beta^{(\nu)}$, $\nu = 1, 2, 3, 4$ account for the number of equivalent symmetrical bands of the ν -th band can be found together with the other parameters of the multi-band model in Tab. 3.1.

The BTE has in principle to be solved in each energy band with index ν for a distribution function $f^{(\nu)}$. However, since the individual distribution functions for each energy band are not of particular interest, it is preferred to have a single dispersion relation describing the total distribution function f .

3.2 Incorporation of Full-Band Effects

In order to account for the angular dependence of the energy on the wave vector in a semiconductor, the inverse dispersion relation is expanded as

$$\mathbf{k}(\varepsilon, \theta, \varphi) = \sum_{l=0}^L \sum_{m=-l}^l k_{l,m}(\varepsilon) Y^{l,m}, \quad (3.15)$$

where due to symmetries of the band structure only even values of l and nonnegative m -values, which are a multiple of four, lead to nonzero expansion coefficients. The expansion coefficients $k_{l,m}$ can either be determined by an integration over spheres in \mathbf{k} -space, cf. (2.2), or by minimization of certain target functionals such as the quadratic error of the scaled moments

$$V_0(\varepsilon) := \frac{1}{(2\pi)^3} \int_{\mathbb{B}} \delta(\varepsilon - \varepsilon(\mathbf{k})) \, d\mathbf{k} , \quad (3.16)$$

$$V_n(\varepsilon) := \frac{1}{(2\pi)^3 V_0(\varepsilon)} \int_{\mathbb{B}} |\mathbf{v}(\mathbf{k})|^n \delta(\varepsilon - \varepsilon(\mathbf{k})) \, d\mathbf{k} , \quad (3.17)$$

where \mathbb{B} denotes the Brillouin zone.

A SHE of the valence band has been carried out by Kosina *et al.* [60] up to 1.27 eV. Pham *et al.* [73] proposed a refined method for an expansion also including higher energies. A fitted band structure based on SHE for the conduction band has been presented by Matz *et al.* [69]. Due to the bijective mapping between energy and wave vector, the velocity and the density of states are not in perfect agreement with full-band data. Nevertheless, good results compared to the Monte Carlo method are obtained [45].

A comparison of the presented energy band models is given in Fig. 3.2. Slight deviations of the many-band model and the full-band density of states are due to different Monte Carlo data used in [11]. While the many-band model provides a good fit for the density of states, it fails to approximate the carrier velocity and is worse than the nonparabolic model (3.3). As expected, the fitted band model provides the best accuracy, even though approximations are less accurate at energies above 2 eV.

Vecchi *et al.* [107] used full-band Monte Carlo data for the velocity \mathbf{v} and the generalized density of states Z for a first-order SHE. This is possible because in this case all terms with an explicit representation of the band structure, i.e. $\Gamma_{0,0}^{l',m'}$, vanish. However, higher-order SHE does not allow for a similar procedure, because the angular coupling term (2.33) does not vanish any longer and an explicit expression for the modulus of the wave vector is required.

Recently, Jin *et al.* [48] suggested a reformulation as follows: Consider

$$\frac{Z}{\hbar|\mathbf{k}|} = \frac{|\mathbf{k}|}{4\pi^3\hbar} \frac{\partial|\mathbf{k}|}{\partial\varepsilon} . \quad (3.18)$$

With the relation $2|\mathbf{k}|\partial|\mathbf{k}|/\partial\varepsilon = \partial|\mathbf{k}|^2/\partial\varepsilon$, the expression can be further rearranged to

$$\frac{\partial}{\partial\varepsilon} \left(Z \frac{1}{\hbar} \frac{\partial\varepsilon}{\partial|\mathbf{k}|} \right) . \quad (3.19)$$

With (3.1), one thus obtains

$$\frac{Z}{\hbar|\mathbf{k}|} \approx \frac{1}{2} \frac{\partial|\mathbf{v}|Z}{\partial\varepsilon} , \quad (3.20)$$

where equality holds true only in a homogeneous material with a spherically symmetric dispersion relation. Nevertheless, the results presented in [48] demonstrate that the use of full-band data for the velocity and the density of states using the approximation (3.20)

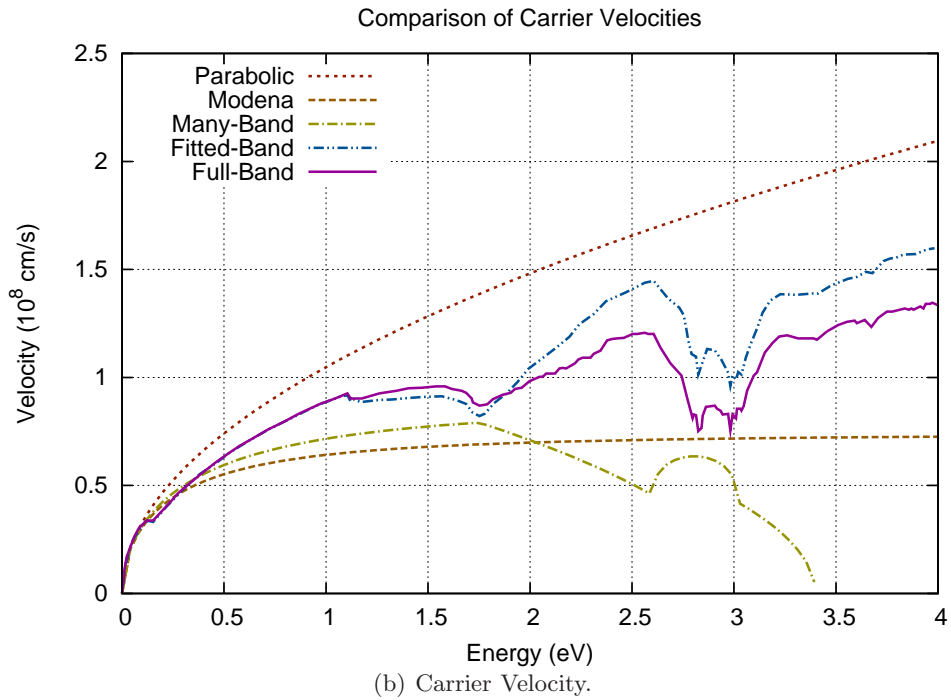
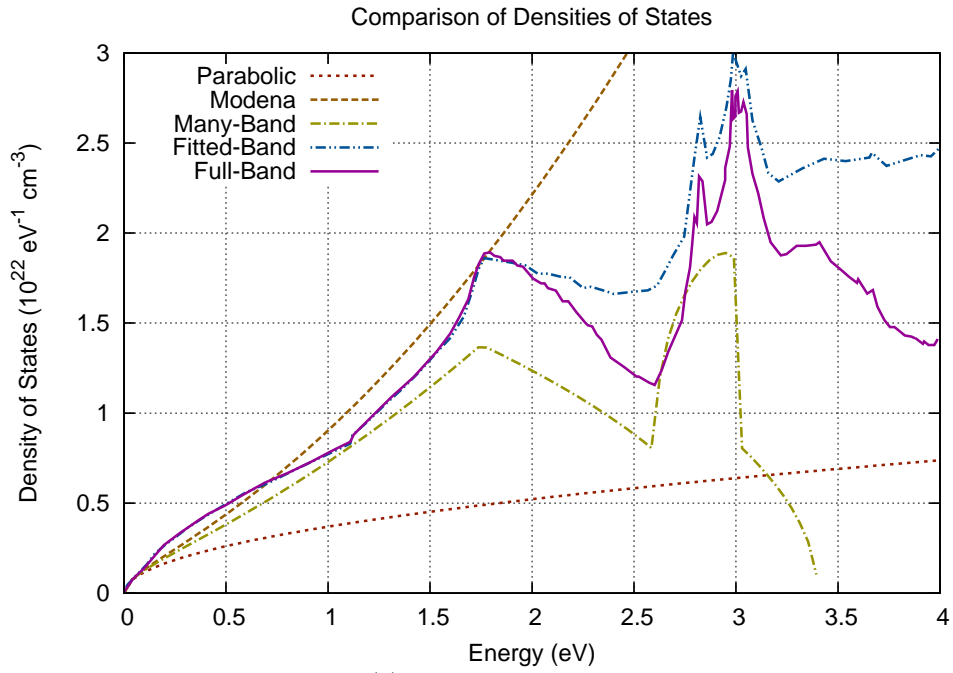


Figure 3.2: Comparison of the density of states and the carrier velocity for the band models (3.2), (3.3), (3.5)-(3.8), and (3.15) with full-band Monte Carlo values from [69]. The nonparabolic band (3.3) using (3.4) and $\alpha = 0.5$ is labelled *Modena* model, as it is also used in e.g. [42].

leads to an accuracy comparable with the anisotropic fitted band (3.15). Consequently, the coupling term (2.33) is then approximated by

$$\Gamma_{l,m}^{l',m'} \approx \frac{1}{2} \frac{\partial |v| Z}{\partial H} \int_{\Omega} \left(\frac{\partial Y^{l,m}}{\partial \theta} e_{\theta} + \frac{1}{\sin \theta} \frac{\partial Y^{l,m}}{\partial \varphi} e_{\varphi} \right) Y^{l',m'} d\Omega \quad (3.21)$$

and similarly for the adjoint term (2.36). The integral can be tabulated easily, since it does not contain any band structure information any longer. As will become clear in Chap. 4, the use of band structure parameters without angular dependencies brings a number of additional benefits from the computational point of view compared to the fitted band structure (3.15).

3.3 Linear Scattering Operators

While the band structure links the particle energy with the particle momentum, it does not fully describe the propagation of carriers. In the presence of an electrostatic force, carriers would be accelerated and thus gain energy indefinitely unless scattering with the crystal lattice or with other carriers is included in the model. The most important scattering mechanisms are discussed in the following. The scattering operator is assumed to be given in the form

$$Q\{f\} = \frac{1}{(2\pi)^3} \int_{\mathbb{B}} s(\mathbf{x}, \mathbf{k}', \mathbf{k}) f(\mathbf{x}, \mathbf{k}', t) - s(\mathbf{x}, \mathbf{k}, \mathbf{k}') f(\mathbf{x}, \mathbf{k}, t) d\mathbf{k}' , \quad (2.13)$$

where it has to be emphasized that scaling factors in front of the scattering integral, here $1/(2\pi)^3$, need to be taken into account when comparing scattering rates from different sources. Note that the numerator of the prefactor differs from the numerator used for the spherical projection (2.6) due to the assumption that scattering does not change spin. Moreover, it should be noted again that the commonly written small sample volume V_s as prefactor for the scattering integral is not written explicitly in the following.

3.3.1 Acoustic Phonon Scattering

Atoms in the crystal lattice vibrate around their fixed equilibrium locations at nonzero temperature. These vibrations are quantized by phonons with energy $\hbar\omega_{\text{phon}}$. Acoustic vibrations refer to a coherent movement of the lattice atoms out of their equilibrium positions. Depending on the displacements with respect to the direction of propagation of the lattice wave, transversal (TA) and longitudinal (LA) acoustic modes are distinguished.

Since the change in particle energy due to acoustic phonon scattering is very small, the process is typically modelled as an elastic process [47], which does not couple different energy levels. The scattering rate can thus be written as

$$s_{\text{ac}}(\mathbf{x}, \mathbf{k}, \mathbf{k}') = \sigma_{\text{ac}} \delta(\varepsilon(\mathbf{k}) - \varepsilon(\mathbf{k}')) , \quad (3.22)$$

where the coefficient σ_{ac} is given by

$$\sigma_{\text{ac}} = \frac{2\pi k_{\text{B}} T \mathcal{E}^2}{\hbar \rho u_{\text{l}}^2} , \quad (3.23)$$

where \mathcal{E} is the deformation potential, ρ is the density of mass, and u_{l} is the longitudinal sound velocity, cf. Tab. 3.2.

	Si	Ge
ρ	2.33 g/cm ³	5.32 g/cm ³
u_1	9.05×10^5 cm/s	5.40×10^5 cm/s
ϵ	$11.7 \times \epsilon_0$	$16.0 \times \epsilon_0$
\mathcal{E}_e	8.90 eV	8.79 eV
\mathcal{E}_h	5.12 eV	7.40 eV

Table 3.2: Material parameters for silicon and germanium, cf. [52]. The subscripts e and h are used to distinguish between electrons and holes.

3.3.2 Optical Phonon Scattering

Optical phonon scattering refers to an out-of-phase movement of lattice atoms. In ionic crystals, these vibrations can be excited by infrared radiation, which explains the name. Similar to acoustic phonon scattering, transversal (TO) and longitudinal (LO) modes are distinguished.

Since the involved phonon energies are rather high, cf. Tab. 3.3, optical phonon scattering is typically modeled as an inelastic process leading to a change of the particle energy. With the phonon occupation number N_{phon} given by the Bose-Einstein statistics

$$N_{\text{phon}} = \frac{1}{\exp\left(\frac{\hbar\omega_{\text{phon}}}{k_B T}\right) - 1}, \quad (3.24)$$

the scattering rate for the initial state \mathbf{k} and the final state \mathbf{k}' can be written as

$$s_{\text{op}}(\mathbf{x}, \mathbf{k}, \mathbf{k}') = \sigma_{\text{op}} \left[N_{\text{phon}} \delta(\varepsilon(\mathbf{k}) - \varepsilon(\mathbf{k}') + \hbar\omega_{\text{op}}) + (1 + N_{\text{phon}}) \delta(\varepsilon(\mathbf{k}) - \varepsilon(\mathbf{k}') - \hbar\omega_{\text{op}}) \right], \quad (3.25)$$

where $\sigma_{\text{op}}(\mathbf{x}, \mathbf{k}, \mathbf{k}')$ is symmetric in \mathbf{k} and \mathbf{k}' and given by

$$\sigma_{\text{op}} = \frac{\pi(D_t K_\nu)^2}{\rho\omega_\nu}, \quad (3.26)$$

with coupling constant $D_t K_\nu$, mass density ρ , and phonon frequency ω_ν . Values for the individual modes can be found in Tab. 3.3. It should be noted that optical phonon scattering couples the energy levels $H - \hbar\omega_{\text{op}}$, H and $H + \hbar\omega_{\text{op}}$ in an asymmetric manner, because scattering from higher energy to lower energy is more likely than vice versa.

3.3.3 Ionized Impurity Scattering

Dopants in a semiconductor are fixed charges inside the crystal lattice. Since carriers are charged particles as well, their trajectories are influenced by these fixed charges, leading to a change of their momentum. The model by Brooks and Herring [10, 47] suggests an elastic scattering process with scattering coefficient

$$s_{\text{imp}}(\mathbf{x}, \mathbf{k}, \mathbf{k}') = \sigma_{\text{imp}}(\mathbf{x}, \mathbf{k}, \mathbf{k}') \delta(\varepsilon(\mathbf{x}) - \varepsilon(\mathbf{x}')), \quad (3.27)$$

		Si		Ge	
ν	Mode	$D_t K_\nu$	$\hbar\omega$	$D_t K_\nu$	$\hbar\omega$
1	TA	0.470×10^8 eV/cm	12.1 meV	0.479×10^8 eV/cm	5.60 meV
2	LA	0.740×10^8 eV/cm	18.5 meV	0.772×10^8 eV/cm	8.60 meV
3	LO	10.23×10^8 eV/cm	62.0 meV	9.280×10^8 eV/cm	37.0 meV
4	TA	0.280×10^8 eV/cm	19.0 meV	0.283×10^8 eV/cm	9.90 meV
5	LA	1.860×10^8 eV/cm	47.4 meV	1.940×10^8 eV/cm	28.0 meV
6	TO	1.860×10^8 eV/cm	58.6 meV	1.690×10^8 eV/cm	32.5 meV

Table 3.3: Modes, coupling constants and energies for inelastic phonon scattering with electrons, cf. [52]. (TA: transversal acoustic, LA: longitudinal acoustic, TO: transversal optical, LO: longitudinal optical)

where $\sigma_{\text{imp}}(\mathbf{x}, \mathbf{k}, \mathbf{k}')$ is symmetric in \mathbf{k} and \mathbf{k}' and given by

$$\sigma_{\text{imp}}(\mathbf{x}, \mathbf{k}, \mathbf{k}') = \frac{2\pi N_{\text{I}} q^4}{\hbar \epsilon^2} \frac{1}{((\mathbf{k}' - \mathbf{k})^2 + 1/\lambda_{\text{D}}^2)^2}. \quad (3.28)$$

The ordinality of the impurity charge is assumed to be one, and N_{a} and N_{d} denote the acceptor and donator concentrations respectively. The Debye length λ_{D} under assumption of local equilibrium is given by

$$\lambda_{\text{D}} = \frac{\epsilon k_{\text{B}} T}{q^2(n+p)}. \quad (3.29)$$

Similar to elastic acoustical phonon scattering, ionized impurity scattering does not couple different energy levels. However, a considerable complication stems from the angular dependence of the coefficient σ_{imp} . This complication can be circumvented by approximating the anisotropic coefficient (3.27) by an elastic-isotropic process with the same momentum relaxation time $\tau_{\text{m;ii}}$ [52]. The momentum relaxation time is computed for an isotropic dispersion relation by an integration over the whole Brillouin zone and by weighting the change of direction of the momentum [67]:

$$\frac{1}{\tau_{\text{m;ii}}(\mathbf{k})} = \frac{1}{(2\pi)^3} \int_{\mathbb{B}} s_{\text{imp}}(\mathbf{x}, \mathbf{k}, \mathbf{k}') (1 - \cos(\theta)) d\mathbf{k}^3$$

Here, the z -axis for the integration in the Brillouin zone is chosen such that it is aligned with \mathbf{k} , hence the angle between \mathbf{k} and \mathbf{k}' is given by the inclination θ . Transformation to spherical coordinates leads to

$$\frac{1}{\tau_{\text{m;ii}}(\mathbf{k})} = \frac{4\pi^3 N_{\text{I}} q^4}{\hbar \epsilon^2} \int_0^\infty \int_0^\pi \frac{1 - \cos(\theta)}{(4|\mathbf{k}|^2 \sin^2(\theta/2) + 1/\lambda_{\text{D}}^2)^2} \sin \theta d\theta dZ d\varepsilon$$

where the density of states Z is independent of the angles because of the assumption of an isotropic dispersion relation. The integral over the inclination θ can be computed analytically as

$$\int_0^\pi \frac{1 - \cos(\theta)}{((\mathbf{k}' - \mathbf{k})^2 + 1/\lambda_{\text{D}}^2)^2} \sin \theta d\theta = \frac{1}{4|\mathbf{k}|^4} \left[\ln(1 + 4\lambda_{\text{D}}^2 |\mathbf{k}|^2) - \frac{4\lambda_{\text{D}}^2 |\mathbf{k}|^2}{1 + 4\lambda_{\text{D}}^2 |\mathbf{k}|^2} \right].$$

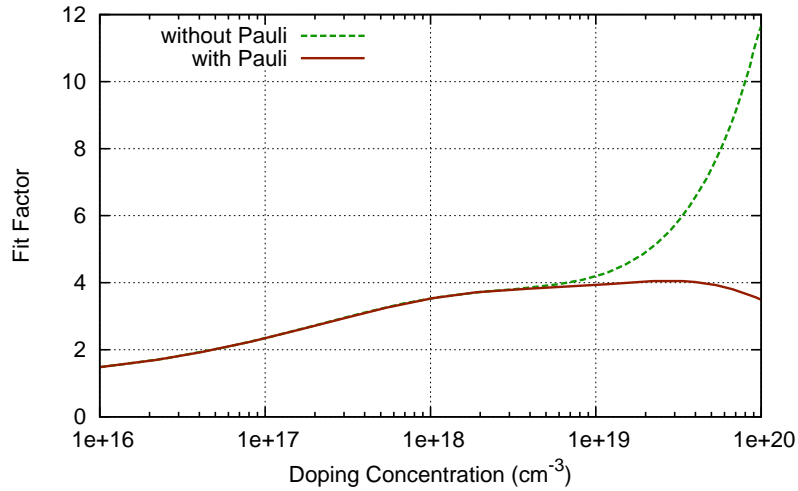


Figure 3.3: Fit factor for ionized impurity scattering in order to reproduce the Caughey-Thomas expression for the mobility [15, 52].

Therefore, the isotropic scattering coefficient

$$\sigma_{\text{imp;iso}}(\mathbf{x}, \mathbf{k}, \mathbf{k}') = \frac{\pi N_I q^4}{\hbar \epsilon^2} \frac{1}{4|\mathbf{k}|^4} \left[\ln(1 + 4\lambda_D^2 |\mathbf{k}|^2) - \frac{4\lambda_D^2 |\mathbf{k}|^2}{1 + 4\lambda_D^2 |\mathbf{k}|^2} \right] \quad (3.30)$$

has the same momentum relaxation time as the anisotropic coefficient (3.27). Note that $|\mathbf{k}|$ should be evaluated consistently with the approximated band, therefore the transformation (3.20) needs to be employed for the full-band case. Moreover, since the Brooks-Herring model fails to correctly describe the carrier mobility at high doping concentrations, an empirical fit factor depicted in Fig. 3.3 is usually employed additionally [52] in order to reproduce the Caughey-Thomas expression for the mobility [15].

3.4 Nonlinear Scattering Operators

The scattering operator in low-density approximation for single carrier processes is linear, which is very attractive from a computational point of view. Consequently, scattering processes leading to a nonlinear scattering operator are often neglected in order to avoid nonlinear iteration schemes. In the following, two such types of scattering mechanisms are considered.

3.4.1 Pauli Exclusion Principle

A high population of the conduction band can lead to the case that the distribution function takes large values near the band edge, thus the term $f(1-f)$ cannot be approximated with f any longer:

$$Q\{f\} = \frac{1}{(2\pi)^3} \int_{\mathbb{B}} s(\mathbf{x}, \mathbf{k}', \mathbf{k}) f(\mathbf{x}, \mathbf{k}', t) (1 - f(\mathbf{x}, \mathbf{k}, t)) - s(\mathbf{x}, \mathbf{k}, \mathbf{k}') f(\mathbf{x}, \mathbf{k}, t) (1 - f(\mathbf{x}, \mathbf{k}', t)) \, d\mathbf{k}' \quad (3.31)$$

Repeating the steps from Sec. 2.2, one finally obtains for the projected in-scattering operator assuming velocity randomization and a scattering rate independent of the angles

$$Q_{\eta,l,m}^{\text{in}}\{f\} = \sigma_{\eta}(\mathbf{x}, \varepsilon \pm \hbar\omega_{\eta}, \varepsilon) \left[Z_{l,m}(\varepsilon) - [f]_{l,m} \right] \frac{[f]_{0,0}(\mathbf{x}, \varepsilon \pm \hbar\omega_{\eta}, t)}{Y_{0,0}}. \quad (3.32)$$

Similarly, the projected out-scattering operator is found as

$$Q_{\eta,l,m}^{\text{out}}\{f\} = \sigma_{\eta}(\mathbf{x}, \varepsilon, \varepsilon \pm \hbar\omega_{\eta}) \left[Z_{0,0}(\varepsilon \pm \hbar\omega_{\eta}) - [f]_{0,0}(\mathbf{x}, \varepsilon \pm \hbar\omega_{\eta}, t) \right] \frac{[f]_{l,m}}{Y_{0,0}}. \quad (3.33)$$

The quadratic nonlinearity needs to be handled by a suitable nonlinear iteration scheme. In [43] it was reported that no complications arose within a Newton scheme.

Numerical results in [43] confirm that the low-density approximation does not have a high impact on macroscopic quantities such as the electron density or carrier velocities, but notable differences in the distribution function are obtained near the band edge. The carrier population is then shifted towards higher energies, because all states at lower energies are already populated.

3.4.2 Carrier-Carrier Scattering

The linear scattering operators in Sec. 3.3 stem from the scattering of carriers with non-carriers. Very important for particularly the high energy tail of the distribution function is carrier-carrier scattering [79]. A carrier-carrier scattering mechanism requires that the two source states are occupied, and the two final states after scattering are empty. This leads to a scattering operator of the form

$$\begin{aligned} Q\{f\} = & \frac{1}{(2\pi)^3} \int_{\mathbb{B}} \int_{\mathbb{B}} \int_{\mathbb{B}} s(\mathbf{x}, \mathbf{k}', \mathbf{k}, \mathbf{k}'_2, \mathbf{k}_2) f(\mathbf{x}, \mathbf{k}', t) (1 - f(\mathbf{x}, \mathbf{k}, t)) f(\mathbf{x}, \mathbf{k}'_2, t) (1 - f(\mathbf{x}, \mathbf{k}_2, t)) \\ & - s(\mathbf{x}, \mathbf{k}, \mathbf{k}', \mathbf{k}_2, \mathbf{k}'_2) f(\mathbf{x}, \mathbf{k}, t) (1 - f(\mathbf{x}, \mathbf{k}', t)) f(\mathbf{x}, \mathbf{k}_2, t) (1 - f(\mathbf{x}, \mathbf{k}'_2, t)) \, d\mathbf{k}' \, d\mathbf{k}_2 \, d\mathbf{k}'_2, \end{aligned} \quad (3.34)$$

where the scattering coefficient $s(\cdot, \cdot, \cdot, \cdot, \cdot)$ now depends on the spatial location and on two pairs of initial and final states. With a low-density approximation, the nonlinearity of degree four of the carrier-carrier scattering operator reduces to second order:

$$\begin{aligned} Q_{\text{cc}}\{f\} = & \frac{1}{(2\pi)^3} \int_{\mathbb{B}} \int_{\mathbb{B}} \int_{\mathbb{B}} s(\mathbf{x}, \mathbf{k}', \mathbf{k}, \mathbf{k}'_2, \mathbf{k}_2) f(\mathbf{x}, \mathbf{k}', t) f(\mathbf{x}, \mathbf{k}'_2, t) \\ & - s(\mathbf{x}, \mathbf{k}, \mathbf{k}', \mathbf{k}_2, \mathbf{k}'_2) f(\mathbf{x}, \mathbf{k}, t) f(\mathbf{x}, \mathbf{k}_2, t) \, d\mathbf{k}' \, d\mathbf{k}_2 \, d\mathbf{k}'_2 \end{aligned} \quad (3.35)$$

The scattering coefficient can be derived to be of the form [96, 99]

$$s(\mathbf{x}, \mathbf{k}', \mathbf{k}, \mathbf{k}'_2, \mathbf{k}_2) = \sigma_{\text{cc}}(\mathbf{x}, \mathbf{k}, \mathbf{k}', \mathbf{k}_2, \mathbf{k}'_2) \delta(\mathbf{k} + \mathbf{k}' - \mathbf{k}_2 - \mathbf{k}'_2) \delta(\varepsilon + \varepsilon' - \varepsilon_2 - \varepsilon'_2), \quad (3.36)$$

where the two delta distributions in (3.36) refer to conservation of momentum and energy respectively, and

$$\sigma_{\text{cc}} = \sigma_{\text{cc}}(\mathbf{x}, \mathbf{k}, \mathbf{k}', \mathbf{k}_2, \mathbf{k}'_2) = \frac{2\pi q^4 n(\mathbf{x})}{\hbar \varepsilon^2} \frac{1}{((\mathbf{k}' - \mathbf{k})^2 + 1/\lambda_{\text{D}}^2)^2}. \quad (3.37)$$

The set of parameters is similar to that of ionized impurity scattering, with the impurity density $N_a + N_d$ replaced by the carrier density n . Since σ_{cc} only depends via β on the difference of the initial and the final state of one of the two carriers, the shorthand notation $\sigma_{cc}(\mathbf{x}, \mathbf{k}, \mathbf{k}')$ is used in the following.

Carrier-carrier scattering, particularly electron-electron scattering, has so far been discussed for first-order SHE only [108, 110]. In a joint work with Peter Willibald Lagger [62], the author has recently extended the method to arbitrary-order SHE, and the derivation is given in the following.

The scattering operator (3.35) is again split into an in-scattering term Q_{cc}^{in} and an out-scattering term Q_{cc}^{out} as in Sec. 2.2. Inserting (3.36) into (3.35), one integration can be carried out due to the momentum conservation. An integration with respect to \mathbf{k}_2 yields

$$Q_{cc}^{\text{in}} = \frac{1}{(2\pi)^3} \int_{\mathbb{B}} \int_{\mathbb{B}} \sigma_{cc}(\mathbf{x}, \mathbf{k}, \mathbf{k}') f(\mathbf{k}') f(\mathbf{k}_2') \delta(\varepsilon + \varepsilon^* - \varepsilon' - \varepsilon_2') d\mathbf{k}' d\mathbf{k}_2', \quad (3.38)$$

with the initial energy $\varepsilon^* := \varepsilon(\mathbf{k}' + \mathbf{k}_2' - \mathbf{k})$ of the second particle involved in the scattering process. A transformation of the two integrals to spherical coordinates leads to

$$Q_{cc}^{\text{in}} = \int_0^\infty \int_0^\infty \int_{\Omega} \int_{\Omega} \sigma_{cc}(\mathbf{x}, \mathbf{k}, \mathbf{k}') f(\mathbf{k}') f(\mathbf{k}_2') Z(\mathbf{k}') Z(\mathbf{k}_2') \times \delta(\varepsilon + \varepsilon^* - \varepsilon' - \varepsilon_2') d\varepsilon' d\varepsilon_2' d\Omega' d\Omega_2', \quad (3.39)$$

where $\mathbf{k} = \mathbf{k}(\varepsilon, \theta, \varphi)$ and similarly for \mathbf{k}' and \mathbf{k}_2' . A projection onto the spherical harmonic $Y^{l,m}$ yields

$$Q_{cc,l,m}^{\text{in}}\{f\}(\mathbf{x}, \varepsilon, t) = \int_0^\infty \int_0^\infty \int_{\Omega} \int_{\Omega} \int_{\Omega} \sigma_{cc}(\mathbf{x}, \mathbf{k}, \mathbf{k}') f(\mathbf{k}') f(\mathbf{k}_2') Z(\mathbf{k}') Z(\mathbf{k}_2') \times \delta(\varepsilon + \varepsilon^* - \varepsilon' - \varepsilon_2') Y^{l,m} Z d\Omega d\Omega' d\Omega_2' d\varepsilon' d\varepsilon_2'. \quad (3.40)$$

Up to now, no approximations have been applied. However, a direct evaluation of these nested integrals at each node in the simulation domain is certainly prohibitive for the use within a simulator due to excessive execution times. Consequently, the further derivation is based on the following two assumptions:

- $\varepsilon^* = \varepsilon(\mathbf{k}' + \mathbf{k}_2' - \mathbf{k})$ can be taken as an external parameter. In principle, the energy ε^* of the second particle before scattering depends due to energy conservation on all variables, i.e. $\varepsilon, \theta, \varphi, \varepsilon', \theta', \varphi', \varepsilon_2', \theta_2', \varphi_2'$. Because the asymptotically exponential distribution of carriers with respect to energy, it is plausible, yet heuristic, that the second particle has an energy close to the band gap. Since no additional information about the second particle involved is known, the average energy is taken for ε^* , which is accessible due to the nonlinear iteration scheme required for the solution of the discrete set of equations.
- The scattering coefficient $\sigma_{cc}(\mathbf{x}, \mathbf{k}, \mathbf{k}')$ can be expanded into spherical harmonics with respect to \mathbf{k} and \mathbf{k}' . This can for example be achieved by using the isotropic approximation (3.30) in order to obtain an isotropic scattering rate with equal macroscopic relaxation time. As an alternative, one may directly compute a spherical projection in order to obtain the expansion coefficients $\sigma_{cc;l_{cc},m_{cc},l'_{cc},m'_{cc}}$ of the expansion

$$\sigma_{cc}(\mathbf{x}, \mathbf{k}, \mathbf{k}') = \sum_{l_{cc}, m_{cc}} \sum_{l'_{cc}, m'_{cc}} \sigma_{cc;l_{cc},m_{cc},l'_{cc},m'_{cc}}(\mathbf{x}, \varepsilon, \varepsilon') Y^{l_{cc},m_{cc}}(\theta, \varphi) Y^{l'_{cc},m'_{cc}}(\theta', \varphi'). \quad (3.41)$$

For the sake of simplicity, it is first assumed $\sigma_{cc} = \sigma_{cc}(\mathbf{x}, \varepsilon, \varepsilon')$ in the following. The same derivations can also be carried out for the coefficients $\sigma_{cc;l_{cc},m_{cc},l'_{cc},m'_{cc}}$, but only the final result for this more general case is given at the end of the derivation.

With these assumptions, one can split the integrands to

$$\begin{aligned} Q_{cc,l,m}^{\text{in}}\{f\} &= \int_0^\infty \int_0^\infty \sigma_{cc}(\mathbf{x}, \varepsilon, \varepsilon') \delta(\varepsilon + \varepsilon^* - \varepsilon' - \varepsilon'_2) \\ &\quad \times \int_\Omega \int_\Omega \int_\Omega f(\mathbf{k}') f(\mathbf{k}'_2) Z(\mathbf{k}') Z(\mathbf{k}'_2) Y_{l,m} Z \, d\Omega \, d\Omega' \, d\Omega'_2 \, d\varepsilon' \, d\varepsilon'_2 . \end{aligned} \quad (3.42)$$

An expansion of f into spherical harmonics, the use of the delta distribution for an elimination of the integral over ε_2 , and the assumption of spherical energy bands leads to

$$\begin{aligned} Q_{cc,l,m}^{\text{in}}\{f\} &= Z \sum_{l',m'} \sum_{l'_2,m'_2} \int_0^\infty c_{cc}(\mathbf{x}, \varepsilon, \varepsilon') f_{l,m}(\varepsilon') f_{l',m'}(\varepsilon + \varepsilon^* - \varepsilon') Z(\varepsilon') Z(\varepsilon + \varepsilon^* - \varepsilon') \, d\varepsilon' \\ &\quad \times \int_\Omega Y_{l,m} \, d\Omega \int_\Omega Y_{l',m'} \, d\Omega' \int_\Omega Y_{l'_2,m'_2} \, d\Omega'_2 . \end{aligned} \quad (3.43)$$

Summing up, the projected in-scattering operator is given by

$$Q_{cc,l,m}^{\text{in}}\{f\} = \frac{Z}{Y_{0,0}^3} \int_0^\infty \sigma_{cc}(\mathbf{x}, \varepsilon, \varepsilon') f_{0,0}(\varepsilon') f_{0,0}(\varepsilon + \varepsilon^* - \varepsilon') Z(\varepsilon) Z(\varepsilon + \varepsilon^* - \varepsilon') \, d\varepsilon' . \quad (3.44)$$

For the more general case of an expansion of the scattering coefficient (3.41), one obtains again with the assumption of spherical energy bands

$$\begin{aligned} Q_{cc,l,m}^{\text{in}}\{f\} &= \frac{1}{Y_{0,0}} Z \int_0^\infty \sigma_{cc;l,m,l',m'}(\mathbf{x}, \varepsilon, \varepsilon') f_{l,m}(\varepsilon') f_{l',m'}(\varepsilon + \varepsilon^* - \varepsilon') \\ &\quad \times Z(\varepsilon) Z(\varepsilon + \varepsilon^* - \varepsilon') \, d\varepsilon' . \end{aligned} \quad (3.45)$$

The projection of the out-scattering operator starts with the same steps as for the in-scattering operator in order to arrive at

$$\begin{aligned} Q_{cc,l,m}^{\text{out}}\{f\} &= Z \sum_{l',m'} f_{l',m'} \sum_{l_2,m_2} \int_0^\infty \int_0^\infty \sigma_{cc}(\mathbf{x}, \varepsilon, \varepsilon') Z(\varepsilon') Z(\varepsilon'_2) \\ &\quad \times \int_\Omega \int_\Omega \int_\Omega f_{l_2,m_2}(\varepsilon^*) \delta(\varepsilon + \varepsilon^* - \varepsilon' - \varepsilon'_2) \\ &\quad \times Y_{l,m} Y_{l',m'} Y_{l_2,m_2}(\theta^*, \varphi^*) \, d\Omega \, d\Omega' \, d\Omega'_2 \, d\varepsilon' \, d\varepsilon'_2 . \end{aligned} \quad (3.46)$$

The angles θ^* and φ^* depend in a complicated way on the other angles, therefore rather crude simplifications are applied. Scattering with another carrier is to a first approximation determined by the density of carriers at the particular location inside the device. Consequently, the distribution function of the second particle, which is described by ε^* and θ^*, φ^* , is approximated by the isotropic part of the distribution function only, since it fully describes the carrier density. With $f(\mathbf{k}^*) = f(\mathbf{k}' + \mathbf{k}'_2 - \mathbf{k}) \approx f_{0,0}(\varepsilon^*) Y_{0,0}$ and considering ε^* again as the average energy, (3.46) simplifies to

$$Q_{cc,l,m}^{\text{out}}\{f\} = \frac{Z}{Y_{0,0}^3} f_{0,0}(\varepsilon^*) f_{l,m}(\varepsilon) \int_0^\infty \sigma_{cc}(\mathbf{x}, \varepsilon, \varepsilon') Z(\varepsilon') Z(\varepsilon + \varepsilon^* - \varepsilon') \, d\varepsilon' . \quad (3.47)$$

The more general case of an expansion of the scattering coefficient (3.41) results in

$$\begin{aligned}
 Q_{cc,l,m}^{\text{out}}\{f\} &= \frac{Z}{Y_{0,0}^2} f_{0,0}(\varepsilon^*) \sum_{l',m'} f_{l',m'} \\
 &\times \sum_{l_{cc},m_{cc}} \int_0^\infty \sigma_{cc;l_{cc},m_{cc},0,0}(\mathbf{x}, \varepsilon, \varepsilon') Z(\varepsilon') Z(\varepsilon + \varepsilon^* - \varepsilon') d\varepsilon' \\
 &\times \int_\Omega Y_{l,m} Y_{l',m'} Y_{l_{cc},m_{cc}} d\Omega .
 \end{aligned} \tag{3.48}$$

For the full projected scattering operator, one thus obtains

$$\begin{aligned}
 Q_{cc,l,m}\{f\} &= \frac{Z}{Y_{0,0}^3} \int_0^\infty \sigma_{cc}(\mathbf{x}, \varepsilon, \varepsilon') [f_{0,0}(\varepsilon') f_{0,0}(\varepsilon + \varepsilon^* - \varepsilon') \\
 &\quad - f_{0,0}(\varepsilon^*) f_{l,m}(\varepsilon)] Z(\varepsilon) Z(\varepsilon + \varepsilon^* - \varepsilon') d\varepsilon' .
 \end{aligned} \tag{3.49}$$

With the use of an expansion of the scattering coefficient (3.41), one obtains

$$\begin{aligned}
 Q_{cc,l,m}\{f\} &= \frac{Z}{Y_{0,0}^2} \sum_{l_{cc},m_{cc}} \sum_{l'_{cc},m'_{cc}} \int_0^\infty \sigma_{cc;l_{cc},m_{cc},l'_{cc},m'_{cc}}(\mathbf{x}, \varepsilon, \varepsilon') \\
 &\quad \left[Y_{0,0} f_{l_{cc},m_{cc}}(\varepsilon') f_{l'_{cc},m'_{cc}}(\varepsilon + \varepsilon^* - \varepsilon') \right. \\
 &\quad \left. - f_{0,0}(\varepsilon^*) \sum_{l',m'} f_{l',m'} \int_\Omega Y_{l,m} Y_{l',m'} Y_{l_{cc},m_{cc}} d\Omega \right] \\
 &\quad \times Z(\varepsilon) Z(\varepsilon + \varepsilon^* - \varepsilon') d\varepsilon' .
 \end{aligned} \tag{3.50}$$

One can immediately see that the full scatter operator vanishes for the equilibrium case, where f is given by a Maxwell distribution. Therefore, even though simplifications have been used for the separate derivation of the projected equations for the in- and the out-scattering operators, the resulting expressions are consistent.

Chapter 4

Structural Properties

The SHE equations furnish a number of interesting structural properties, which are the topic of this chapter. All properties are discussed on the continuous level and result from certain symmetries of the underlying physical processes. Consequently, no additional assumptions about a particular discretization method need to be imposed and the same structural properties hold true for the system of discretized linear equations as outlined in Chap. 5.

In Sec. 4.1 the coupling between the SHE equations is investigated and a scheme for the lossless compression of the system matrix is proposed, which greatly reduces the memory consumption of the SHE method at high expansion orders. The different boundary conditions used for the SHE method are discussed in Sec. 4.4 and extensions to the system matrix compression scheme are proposed in order to handle them. This chapter closes with some numerical results demonstrating the benefits of the proposed compression scheme.

4.1 Sparse Coupling for Spherical Energy Bands

As already noted in Sec. 2.3, the terms $[Y^{l,m'}]_{l,m}$, $\mathbf{j}_{l,m}^{l',m'}$ and $\mathbf{\Gamma}_{l,m}^{l',m'}$ determine the coupling among the projected equations (2.30). If all coupling coefficients were multiples of the Kronecker delta, then the SHE equations were decoupled and could be solved individually. On the contrary, if all coupling coefficients were nonzero, all projected equations were coupled with each other. In analogy to systems of linear equations described by matrices, one is typically interested in a weak coupling, which typically accelerates the solution process, and on the other hand leads to lower memory requirements. A closer inspection of the coupling structure for spherically symmetric dispersion relations is carried out in this section.

For general band structures, the symmetry of the underlying processes leads to the following result: [53]

Theorem 1 (Jungemann *et. al.*). *For a spherical harmonics expansion up to order $L = 2I+1$ with $I \in \mathbb{N}$, there holds for all $i, i' \in \{0, \dots, I\}$, $m \in \{-i, \dots, i\}$ and $m' \in \{-i', \dots, i'\}$*

$$\mathbf{j}_{2i,m}^{2i',m'} = \mathbf{j}_{2i+1,m}^{2i'+1,m'} = \mathbf{0}, \quad \mathbf{\Gamma}_{2i,m}^{2i',m'} = \mathbf{\Gamma}_{2i+1,m}^{2i'+1,m'} = \mathbf{0} .$$

The essence of this theorem is that all nonzero coupling coefficients possess different parities in the leading indices. This small structural information about the coupling was already used for a preprocessing step for the solution of the discretized equations in [53].

Under the assumption of spherical energy bands, i.e. $\varepsilon(\mathbf{k}) = \varepsilon(|\mathbf{k}|)$, the velocity \mathbf{v} , the modulus of the wave vector $|\mathbf{k}|$ and the generalized density of states only depend on the energy ε , but not on the angles θ, φ . Consequently, (2.31), (2.32) and (2.31) are rewritten as

$$[Y^{l',m'}]_{l,m} = \delta_{l,m}^{l',m'}, \quad (4.1)$$

$$\mathbf{j}_{l,m}^{l',m'} = vZ \int Y_{l,m} \mathbf{e}_\varepsilon Y_{l',m'} \, d\Omega =: vZ \mathbf{a}_{l,m}^{l',m'}, \quad (4.2)$$

$$\mathbf{\Gamma}_{l,m}^{l',m'} = \frac{Z}{\hbar|\mathbf{k}|} \int \left(\frac{\partial Y_{l,m}}{\partial \theta} \mathbf{e}_\theta + \frac{1}{\sin \theta} \frac{\partial Y_{l,m}}{\partial \varphi} \mathbf{e}_\varphi \right) Y_{l',m'} \, d\Omega =: \frac{Z}{\hbar|\mathbf{k}|} \mathbf{b}_{l,m}^{l',m'}, \quad (4.3)$$

where $\delta_{l,m}^{l',m'}$ denotes the Kronecker delta and $\mathbf{v} = v\mathbf{e}_\varepsilon$. A similar decomposition is possible with the full-band modification (3.20).

The coupling between index pairs (l, m) and (l', m') is determined by the integral terms $\mathbf{a}_{l,m}^{l',m'}$ and $\mathbf{b}_{l,m}^{l',m'}$ only. As shown by the author, it turns out that the coupling is rather weak:

Theorem 2. *For spherical energy bands and indices $l, l' \in \{0, \dots, L\}$, $m \in \{-l, \dots, l\}$ and $m' \in \{-l', \dots, l'\}$, there holds:*

(i) *If $\mathbf{j}_{l,m}^{l',m'}$ is nonzero, then $l \in \{l' \pm 1\}$ and $m \in \{\pm|m'| \pm 1, m'\}$.*

(ii) *If $\mathbf{\Gamma}_{l,m}^{l',m'}$ is nonzero, then $l \in \{l' \pm 1\}$ and $m \in \{\pm|m'| \pm 1, m'\}$.*

A rather lengthy and technical proof is given in [87] and makes use of recurrence relations and orthogonalities of trigonometric functions and associated Legendre functions.

Thm. 2 is very important for large expansion orders L : The total number of unknown expansion coefficients is $(L+1)^2$, but according to the result of the theorem, each $f_{l,m}$ is directly coupled with at most ten other coefficients. It should also be noted that the weak coupling stated in Thm. 2 has already been observed for less general situations in earlier publications [37, 78].

Next, the structure of the SHE equations (2.30) for spherical energy bands is investigated in depth. Unlike the presentation in [87], the structure is investigated already at the continuous level, which has the advantage of covering a wider class of discretization schemes and less notational clutter. Due to the equivalence of (2.30) and (2.38) for spherical energy bands, the results in this section apply equally to an expansion of the distribution function f and to an expansion of the generalized distribution function g .

A motivation for a first-order expansion is now given, then the scheme is extended to general expansion orders. Ignoring the stabilization using MEDS in a first step, the four SHE equations using Einstein summation convention read

$$\begin{aligned} \frac{\partial f_{0,0}}{\partial t} + vZ \mathbf{a}_{0,0}^{l',m'} \cdot \nabla_{\mathbf{x}} f_{l',m'} + \frac{Z f_{l',m'}}{\hbar|\mathbf{k}|} \mathbf{b}_{0,0}^{l',m'} \cdot \mathbf{F} + \sum_{\eta} \left(\tilde{s}_{0,0}^{l',m';\text{out}} s_{\eta}^{\text{out}} - \tilde{s}_{0,0}^{l',m';\text{in}} s_{\eta}^{\text{in}} \right) f_{l',m'} &= 0, \\ \frac{\partial f_{1,-1}}{\partial t} + vZ \mathbf{a}_{1,-1}^{l',m'} \cdot \nabla_{\mathbf{x}} f_{l',m'} + \frac{Z f_{l',m'}}{\hbar|\mathbf{k}|} \mathbf{b}_{1,-1}^{l',m'} \cdot \mathbf{F} + \sum_{\eta} \left(\tilde{s}_{1,-1}^{l',m';\text{out}} s_{\eta}^{\text{out}} - \tilde{s}_{1,-1}^{l',m';\text{in}} s_{\eta}^{\text{in}} \right) f_{l',m'} &= 0, \\ \frac{\partial f_{1,0}}{\partial t} + vZ \mathbf{a}_{1,0}^{l',m'} \cdot \nabla_{\mathbf{x}} f_{l',m'} + \frac{Z f_{l',m'}}{\hbar|\mathbf{k}|} \mathbf{b}_{1,0}^{l',m'} \cdot \mathbf{F} + \sum_{\eta} \left(\tilde{s}_{1,0}^{l',m';\text{out}} s_{\eta}^{\text{out}} - \tilde{s}_{1,0}^{l',m';\text{in}} s_{\eta}^{\text{in}} \right) f_{l',m'} &= 0, \\ \frac{\partial f_{1,1}}{\partial t} + vZ \mathbf{a}_{1,1}^{l',m'} \cdot \nabla_{\mathbf{x}} f_{l',m'} + \frac{Z f_{l',m'}}{\hbar|\mathbf{k}|} \mathbf{b}_{1,1}^{l',m'} \cdot \mathbf{F} + \sum_{\eta} \left(\tilde{s}_{1,1}^{l',m';\text{out}} s_{\eta}^{\text{out}} - \tilde{s}_{1,1}^{l',m';\text{in}} s_{\eta}^{\text{in}} \right) f_{l',m'} &= 0. \end{aligned}$$

The terms $\tilde{s}_{l,m}^{l',m';\text{out}} s_\eta^{\text{out}}$ and $\tilde{s}_{l,m}^{l',m';\text{in}} s_\eta^{\text{in}}$ may be operators in order to take shifts of the arguments of the distribution function into account and denote the angular coupling of the scattering operator and reduce to Kronecker deltas when scattering processes are modeled as velocity randomizing, cf. Sec. 2.2.

This continuous linear system of partial differential equations can be written in operator matrix form as

$$\begin{aligned}
& \left[\frac{\partial}{\partial t} \begin{pmatrix} 1 & 0 & 0 & 0 \\ 0 & 1 & 0 & 0 \\ 0 & 0 & 1 & 0 \\ 0 & 0 & 0 & 1 \end{pmatrix} + vZ\nabla_{\mathbf{x}} \cdot \begin{pmatrix} \mathbf{a}_{0,0}^{0,0} & \mathbf{a}_{0,0}^{1,-1} & \mathbf{a}_{0,0}^{1,0} & \mathbf{a}_{0,0}^{1,1} \\ \mathbf{a}_{1,-1}^{0,0} & \mathbf{a}_{1,-1}^{1,-1} & \mathbf{a}_{1,-1}^{1,0} & \mathbf{a}_{1,-1}^{1,1} \\ \mathbf{a}_{1,0}^{0,0} & \mathbf{a}_{1,0}^{1,-1} & \mathbf{a}_{1,0}^{1,0} & \mathbf{a}_{1,0}^{1,1} \\ \mathbf{a}_{1,1}^{0,0} & \mathbf{a}_{1,1}^{1,-1} & \mathbf{a}_{1,1}^{1,0} & \mathbf{a}_{1,1}^{1,1} \end{pmatrix} \right. \\
& + \frac{ZF}{\hbar|\mathbf{k}|} \cdot \begin{pmatrix} \mathbf{b}_{0,0}^{0,0} & \mathbf{b}_{0,0}^{1,-1} & \mathbf{b}_{0,0}^{1,0} & \mathbf{b}_{0,0}^{1,1} \\ \mathbf{b}_{1,-1}^{0,0} & \mathbf{b}_{1,-1}^{1,-1} & \mathbf{b}_{1,-1}^{1,0} & \mathbf{b}_{1,-1}^{1,1} \\ \mathbf{b}_{1,0}^{0,0} & \mathbf{b}_{1,0}^{1,-1} & \mathbf{b}_{1,0}^{1,0} & \mathbf{b}_{1,0}^{1,1} \\ \mathbf{b}_{1,1}^{0,0} & \mathbf{b}_{1,1}^{1,-1} & \mathbf{b}_{1,1}^{1,0} & \mathbf{b}_{1,1}^{1,1} \end{pmatrix} \\
& + \sum_{\eta} s_{\eta}^{\text{out}} \begin{pmatrix} \tilde{s}_{0,0}^{0,0;\text{out}} & \tilde{s}_{0,0}^{1,-1;\text{out}} & \tilde{s}_{0,0}^{1,0;\text{out}} & \tilde{s}_{0,0}^{1,1;\text{out}} \\ \tilde{s}_{1,-1}^{0,0;\text{out}} & \tilde{s}_{1,-1}^{1,-1;\text{out}} & \tilde{s}_{1,-1}^{1,0;\text{out}} & \tilde{s}_{1,-1}^{1,1;\text{out}} \\ \tilde{s}_{1,0}^{0,0;\text{out}} & \tilde{s}_{1,0}^{1,-1;\text{out}} & \tilde{s}_{1,0}^{1,0;\text{out}} & \tilde{s}_{1,0}^{1,1;\text{out}} \\ \tilde{s}_{1,1}^{0,0;\text{out}} & \tilde{s}_{1,1}^{1,-1;\text{out}} & \tilde{s}_{1,1}^{1,0;\text{out}} & \tilde{s}_{1,1}^{1,1;\text{out}} \end{pmatrix} \\
& \left. - \sum_{\eta} s_{\eta}^{\text{in}} \begin{pmatrix} \tilde{s}_{0,0}^{0,0;\text{in}} & \tilde{s}_{0,0}^{1,-1;\text{in}} & \tilde{s}_{0,0}^{1,0;\text{in}} & \tilde{s}_{0,0}^{1,1;\text{in}} \\ \tilde{s}_{1,-1}^{0,0;\text{in}} & \tilde{s}_{1,-1}^{1,-1;\text{in}} & \tilde{s}_{1,-1}^{1,0;\text{in}} & \tilde{s}_{1,-1}^{1,1;\text{in}} \\ \tilde{s}_{1,0}^{0,0;\text{in}} & \tilde{s}_{1,0}^{1,-1;\text{in}} & \tilde{s}_{1,0}^{1,0;\text{in}} & \tilde{s}_{1,0}^{1,1;\text{in}} \\ \tilde{s}_{1,1}^{0,0;\text{in}} & \tilde{s}_{1,1}^{1,-1;\text{in}} & \tilde{s}_{1,1}^{1,0;\text{in}} & \tilde{s}_{1,1}^{1,1;\text{in}} \end{pmatrix} \right] \times \begin{pmatrix} f_{0,0} \\ f_{1,-1} \\ f_{1,0} \\ f_{1,1} \end{pmatrix} = \mathbf{0}, \tag{4.4}
\end{aligned}$$

where the gradient and the time derivative act as an operator on the expansion coefficients, not on the coefficient matrices. The crucial observation now is that all entries in each of the matrices are independent of the spatial variable \mathbf{x} as well as of total energy H . Writing $\mathbf{F}(\mathbf{x})$ and \mathbf{x} in components,

$$\mathbf{F}(\mathbf{x}) = \begin{pmatrix} F_1(\mathbf{x}) \\ F_2(\mathbf{x}) \\ F_3(\mathbf{x}) \end{pmatrix}, \quad \mathbf{x} = \begin{pmatrix} x_1 \\ x_2 \\ x_3 \end{pmatrix},$$

the considered first-order system can thus be written as

$$\left[\frac{\partial}{\partial t} \mathbf{I} + \sum_{p=1}^3 vZ \frac{\partial}{\partial x_p} \mathbf{A}_p + \sum_{p=1}^3 \frac{ZF_p}{\hbar|\mathbf{k}|} \mathbf{B}_p + \sum_{\eta} s_{\eta}^{\text{out}} \mathbf{S}_{\eta}^{\text{out}} - \sum_{\eta} s_{\eta}^{\text{in}} \mathbf{S}_{\eta}^{\text{in}} \right] \begin{pmatrix} f_{0,0} \\ f_{1,-1} \\ f_{1,0} \\ f_{1,1} \end{pmatrix} = \mathbf{0}, \tag{4.5}$$

where the matrices \mathbf{I} , \mathbf{A}_p , \mathbf{B}_p , $\mathbf{S}_{\eta}^{\text{out}}$ and $\mathbf{S}_{\eta}^{\text{in}}$ are given by the respective matrices in (4.4).

For the case of a general expansion order L , an enumeration of the index pairs (l, m) is required. Let κ denote such a mapping, for instance $\kappa(l, m) = l^2 + l + m + 1$. Repeating the calculation for the general case, one obtains that the operator matrix \mathbf{S} for the SHE equations can be written as

$$\mathbf{S} = \sum_{i=1}^{11} q_i(\mathbf{x}, H) \mathbf{R}_i. \tag{4.6}$$

The spatial terms q_1, \dots, q_{11} are given by

$$q_1(\mathbf{x}, H) = \frac{\partial}{\partial t}, \quad (4.7)$$

$$q_p(\mathbf{x}, H) = v \frac{\partial}{\partial x_{p-1}}, \quad p = 2, 3, 4, \quad (4.8)$$

$$q_p(\mathbf{x}, H) = -F_{p-4} \frac{1}{\hbar |\mathbf{k}|}, \quad p = 5, 6, 7, \quad (4.9)$$

$$q_8(\mathbf{x}, H) = \frac{1}{Y_{0,0}} \sum_{\eta} \sigma_{\eta}(\mathbf{x}, H, H + \hbar\omega_{\eta}) Z_{0,0} Z_{0,0}(H + \hbar\omega_{\eta}), \quad (4.10)$$

$$q_9(\mathbf{x}, H) = \frac{1}{Y_{0,0}} \sum_{\eta} \sigma_{\eta}(\mathbf{x}, H, H - \hbar\omega_{\eta}) Z_{0,0} Z_{0,0}(H - \hbar\omega_{\eta}), \quad (4.11)$$

$$q_{10}(\mathbf{x}, H) = -\frac{1}{Y_{0,0}} \sum_{\eta} \sigma_{\eta}(\mathbf{x}, H + \hbar\omega_{\eta}, H) Z_{0,0}(H + \hbar\omega_{\eta}) \mathbb{D}_{\hbar\omega_{\eta}}, \quad (4.12)$$

$$q_{11}(\mathbf{x}, H) = -\frac{1}{Y_{0,0}} \sum_{\eta} \sigma_{\eta}(\mathbf{x}, H - \hbar\omega_{\eta}, H) Z_{0,0}(H - \hbar\omega_{\eta}) \mathbb{D}_{-\hbar\omega_{\eta}}, \quad (4.13)$$

with the energy shift operator $\mathbb{D}_y\{f\}(\mathbf{x}, H) := f(\mathbf{x}, H + y)$. Note that some of the terms q_2, \dots, q_7 evaluate to zero if one- or two-dimensional simulations are carried out. The angular coupling matrices $\mathbf{R}_1, \dots, \mathbf{R}_{11}$ are determined by

$$(\mathbf{R}_1)_{\kappa(l,m),\kappa(l',m')} = \delta_{l,l'} \delta_{m,m'}, \quad (4.14)$$

$$(\mathbf{R}_p)_{\kappa(l,m),\kappa(l',m')} = (\mathbf{a}_{l,m}^{l',m'})_{p-1}, \quad p = 2, 3, 4, \quad (4.15)$$

$$(\mathbf{R}_p)_{\kappa(l,m),\kappa(l',m')} = (\mathbf{b}_{l,m}^{l',m'})_{p-4}, \quad p = 5, 6, 7, \quad (4.16)$$

$$(\mathbf{R}_8)_{\kappa(l,m),\kappa(l',m')} = \delta_{l,l'} \delta_{m,m'}, \quad (4.17)$$

$$(\mathbf{R}_9)_{\kappa(l,m),\kappa(l',m')} = \delta_{l,l'} \delta_{m,m'}, \quad (4.18)$$

$$(\mathbf{R}_{10})_{\kappa(l,m),\kappa(l',m')} = \delta_{l,l'} \delta_{m,m'} \delta_{l',0} \delta_{m',0}, \quad (4.19)$$

$$(\mathbf{R}_{11})_{\kappa(l,m),\kappa(l',m')} = \delta_{l,l'} \delta_{m,m'} \delta_{l',0} \delta_{m',0}. \quad (4.20)$$

Hence, the full continuous system of equations \mathbf{S} can be composed out of continuous spatial terms q_p and constant angular coupling matrices \mathbf{R}_p , $p = 1, \dots, 11$. It is worthwhile to mention that each of the coefficient pair (q_8, q_9) can be replaced by a single coefficient, and similarly for (q_{10}, q_{11}) if only elastic scattering is considered. In analogy, each of the pairs $(\mathbf{R}_8, \mathbf{R}_9)$ and $(\mathbf{R}_{10}, \mathbf{R}_{11})$ can be replaced by a single matrix [87].

The decomposition of the continuous case is preserved after spatial discretization. To see this, let $\mathbf{Q}_1, \dots, \mathbf{Q}_{11}$ denote the matrices arising from an arbitrary discretization of the terms q_1, \dots, q_{11} . In most cases, a finite volume or a finite element method will be employed, but also less widespread techniques such as wavelet methods could be used. Then, the discrete system matrix \mathbf{S}_h for the SHE equations can be written as

$$\mathbf{S}_h = \sum_{i=1}^{11} \mathbf{Q}_i \otimes \mathbf{R}_i, \quad (4.21)$$

where \otimes denotes the Kronecker product (cf. A.1 for the definition). After a suitable rearrangement of unknowns, the system matrix could also be written in the equivalent form

$$\tilde{\mathbf{S}}_{\text{h}} = \sum_{i=1}^{11} \mathbf{R}_i \otimes \mathbf{Q}_i . \quad (4.22)$$

The advantage of a representation using sums of Kronecker products is the considerably smaller memory required for the factors. For a SHE of order L , the matrices \mathbf{R}_i are of size $(L+1)^2 \times (L+1)^2$ and sparse according to Sec. 4.1. For a spatial discretization using N unknowns, the matrices \mathbf{Q}_i are of dimension $N \times N$ and typically sparse, hence the full system matrix \mathbf{S}_{h} is of dimension $N(L+1)^2 \times N(L+1)^2$. While the explicit storage of a sparse system \mathbf{S}_{h} thus requires $\mathcal{O}(N(L+1)^2) = \mathcal{O}(NL^2)$ memory, a storage of the Kronecker product factors requires $\mathcal{O}(N+L^2)$ memory only, which is a considerable difference already for $L = 5$ or $L = 7$.

In light of the memory requirements for the system matrix it is also worthwhile to point out the importance of Thm. 2: Without the sparsity of coupling coefficients and without the use of a Kronecker representation, $\mathcal{O}(N(L+1)^4) = \mathcal{O}(NL^4)$ memory is required. With the sparsity of coupling coefficients, only $\mathcal{O}(NL^2)$ memory is required for a full representation of \mathbf{S}_{h} , which is further reduced to $\mathcal{O}(N+L^2)$ when using a Kronecker product representation. Since typical values of L are in the range three to seven, the memory savings due to Thm. 2 combined with (4.21) can be orders of magnitude.

4.2 Coupling for Nonspherical Energy Bands

The matrix compression described in the previous section relies on the factorizations (4.2) and (4.3) of the coupling terms $\mathbf{J}_{l,m}^{l',m'}$ and $\mathbf{\Gamma}_{l,m}^{l',m'}$, such that the factors depend on either energy (and possibly the spatial location) or on the indices l , m , l' and m' , but not on both. Moreover, the derivation requires that the density of states does not show an angular dependence. However, in the case of nonspherical energy bands, these three terms depend on energy and on angles.

In order to decouple the radial (energy) contributions from the angular ones for nonspherical energy band models, a spherical projection up to order L' of the coupling terms can be performed by approximating [53]

$$\mathbf{v}(\varepsilon, \theta, \varphi) \approx \sum_{l''=0}^{L'} \sum_{m''=-l''}^{l''} \tilde{\mathbf{v}}_{l'',m''}(\varepsilon) Y^{l'',m''}(\theta, \varphi) , \quad (4.23)$$

$$\frac{1}{\hbar |\mathbf{k}(\varepsilon, \theta, \varphi)|} \approx \sum_{l''=0}^{L'} \sum_{m''=-l''}^{l''} \tilde{\Gamma}_{l'',m''}(\varepsilon) Y^{l'',m''}(\theta, \varphi) , \quad (4.24)$$

$$\mathbf{Z}(\varepsilon, \theta, \varphi) \approx \sum_{l''=0}^{L'} \sum_{m''=-l''}^{l''} \tilde{\mathbf{Z}}_{l'',m''}(\varepsilon) Y^{l'',m''}(\theta, \varphi) , \quad (4.25)$$

where the expansion coefficients are given for $\varepsilon > 0$ by

$$\begin{aligned}\tilde{\mathbf{v}}_{l'',m''}(\varepsilon) &= \int_{\Omega} \mathbf{v}(\varepsilon, \theta, \varphi) Y^{l'',m''}(\theta, \varphi) \, d\Omega, \\ \tilde{\Gamma}_{l'',m''}(\varepsilon) &= \int_{\Omega} \frac{1}{\hbar|\mathbf{k}(\varepsilon, \theta, \varphi)|} Y^{l'',m''}(\theta, \varphi) \, d\Omega, \\ \tilde{Z}_{l'',m''}(\varepsilon) &= \int_{\Omega} Z(\varepsilon, \theta, \varphi) Y^{l'',m''}(\theta, \varphi) \, d\Omega.\end{aligned}$$

For simplicity, the expansion order L' , which depends on the complexity of the band structure, is taken to be the same for \mathbf{v} , $(\hbar|\mathbf{k}|)^{-1}$ and Z . In a slightly different context, values of $L' = 4$ have been used in [73] and [69] for an expansion of \mathbf{k} , and good accuracy has been obtained. On the other hand, a spherically symmetric velocity profile is exactly recovered by an expansion order $L' = 1$.

The expansion order of the generalized density of states Z is implicitly coupled to the expansion order L of the distribution function by the scattering operator (2.23). Thus, even if Z is expanded up to order $L' > L$, only expansion terms up to order L can be considered. For this reason $L' \leq L$ is assumed in the following.

Substitution of the expansions (4.23) and (4.24) into (4.2) and (4.3) yields

$$\begin{aligned}\mathbf{j}_{l,m}^{l',m'} &= \tilde{\mathbf{v}}_{l'',m''}(\varepsilon) \int_{\Omega} Y^{l,m} Y^{l',m'} Y^{l'',m''} \, d\Omega =: \mathbf{v}_{l'',m''}(\varepsilon) a_{l,m}^{l',m';l'',m''}, \\ \Gamma_{l,m}^{l',m'} &= \tilde{\Gamma}_{l'',m''}(\varepsilon) \int_{\Omega} \left(\frac{\partial Y^{l,m}}{\partial \theta} e_{\theta} + \frac{1}{\sin \theta} \frac{\partial Y^{l,m}}{\partial \varphi} e_{\varphi} \right) Y^{l',m'} Y^{l'',m''} \, d\Omega =: \Gamma_{l'',m''}(\varepsilon) \mathbf{b}_{l,m}^{l',m';l'',m''},\end{aligned}$$

so that in both cases a sum of $(L' + 1)^2$ decoupled terms is obtained. Note that in the case of spherical energy bands, the sum degenerates to a single term. Repeating the steps from the previous section, the continuous system of partial differential equations \mathbf{S} can be written similar to (4.6) in the form

$$\mathbf{S}_h = \sum_{i=1}^{1+10(L'+1)^2} q_i(\mathbf{x}, H) \mathbf{R}_i, \quad (4.26)$$

while the discrete system matrix \mathbf{S}_h can be written in analogy to (4.21) as

$$\mathbf{S}_h = \sum_{i=1}^{1+10(L'+1)^2} \mathbf{Q}_i \otimes \mathbf{R}_i. \quad (4.27)$$

The entries of the coupling matrices due to $a_{l,m}^{l',m';l'',m''}$ are directly obtained from the Wigner 3jm-symbols, cf. A.2. The sparsity of the coupling matrices due to $\mathbf{b}_{l,m}^{l',m';l'',m''}$ is not clear at present, but a similar structure is expected. Assuming for simplicity dense spherical harmonics coupling matrices, the system matrix can be stored using at most $\mathcal{O}(L'^2(L^4 + N))$ memory, where in typical situations $L^4 \ll N$.

4.3 Stabilization Schemes

The stabilization schemes discussed in Sec. 2.3 lead to different equations for even-order and odd-order projected equations. Since MEDS basically exchanges the summation index

and the sign of the coupling term $\Gamma_{l,m}^{l',m'}$, the representations (4.6) and (4.26) can be extended to

$$\mathbf{S} = \sum_{i=1}^p q_i(\mathbf{x}, H) (\mathbf{R}_i^e + \mathbf{R}_i^o) , \quad (4.28)$$

where p denotes the number of matrices. \mathbf{R}_i^e refers to the even-order equations and is obtained from \mathbf{R}_i by setting all rows $\kappa(2l+1, m)$ to zero. \mathbf{R}_i^o is obtained from \mathbf{R}_i by transposition and zeroing all rows $\kappa(2l, m)$ of the transposed matrix. In addition, signs are swapped in terms affected by MEDS.

For the discretization it is assumed that even-order harmonics can be discretized in a different manner than odd-order harmonics. If all even-order unknowns are enumerated first, the system matrix \mathbf{S}_h has a block-structure of the form

$$\mathbf{S}_h = \begin{pmatrix} \mathbf{S}_h^{ee} & \mathbf{S}_h^{eo} \\ \mathbf{S}_h^{oe} & \mathbf{S}_h^{oo} \end{pmatrix} = \sum_{i=1}^p \begin{pmatrix} \mathbf{Q}_i^{ee} \otimes \mathbf{R}_i^{ee} & \mathbf{Q}_i^{eo} \otimes \mathbf{R}_i^{eo} \\ \mathbf{Q}_i^{oe} \otimes \mathbf{R}_i^{oe} & \mathbf{Q}_i^{oo} \otimes \mathbf{R}_i^{oo} \end{pmatrix} . \quad (4.29)$$

The even-to-even coupling matrix \mathbf{S}_h^{ee} and the odd-to-odd coupling matrix \mathbf{S}_h^{oo} are square matrices and determined according to Thm. 1 or Thm. 2 only by the projected time derivative $\partial[f]_{l,m}/\partial t$ and the projected scattering operator $Q_{l,m}\{f\}$. The even-to-odd coupling matrix \mathbf{S}_h^{eo} is not necessarily square and determined by the free-streaming operator with sparsity pattern given by Thm. 2. The odd-to-even coupling matrix \mathbf{S}_h^{oe} is rectangular in general and determined by the free-streaming operator and for nonspherical bands also by the scattering operator $Q_{l,m}\{f\}$, cf. (2.23).

Since the coupling structure of the scattering operator is explicitly given by (2.23), the structure of \mathbf{S}_h^{ee} and \mathbf{S}_h^{oo} is as follows:

Theorem 3. *The following statements hold true for a system matrix (4.29) obtained from a discretization of the stabilized SHE equations in steady-state with velocity-randomizing scattering processes only:*

- (i) *The matrix \mathbf{S}_h^{oo} is diagonal.*
- (ii) *For spherical energy bands without considering inelastic scattering, \mathbf{S}_h^{ee} is diagonal.*

This structural information is very important for the construction of solution schemes in Sec. 4.5.

4.4 Boundary Conditions

Only the discretization of the resulting system of partial differential equations in the interior of the simulation domain has been considered in an abstract fashion so far. At the boundary, suitable conditions need to be imposed and incorporated into the proposed compression scheme.

At all noncontact boundaries, homogeneous Neumann boundary conditions are imposed [42, 53, 78], which can be directly included in the proposed compression scheme, because no additional boundary terms appear. At the contact boundaries, two different types of boundary conditions are typically imposed. The first type are Dirichlet boundary

conditions [78], where the distribution function is set to a Maxwell distribution. Hence, the expansion coefficient $f_{0,0}$ is set according to (2.1), while $f_{l,m}$ is set to zero for $(l, m) \neq (0, 0)$. This is either enforced by replacing the corresponding matrix row with unity in the diagonal and zeros elsewhere as well as setting the appropriate value at the right hand side vector, or by directly absorbing the known values to the load vector. For the proposed compression scheme, the second way is of advantage, because in that case boundary conditions do not alter the matrix structure.

The second type of contact boundary conditions is a Robin-type generation/recombination process [53]

$$\gamma_{l,m}(\varepsilon) = -\frac{Z_{l,m}(\varepsilon)f_{l,m}(\varepsilon) - Z_{l,m}(\varepsilon)f^{\text{eq}}(\varepsilon)}{\tau_0},$$

where f^{eq} denotes the equilibrium Maxwell distribution, or, similar in structure, a surface generation process of the form [42]

$$\Gamma^{\text{S}} = [f^{\text{eq}}(\mathbf{k}')\vartheta(\mathbf{v} \cdot \mathbf{n}) + f(\mathbf{k}')\vartheta(-\mathbf{v} \cdot \mathbf{n})]\mathbf{v} \cdot \mathbf{n},$$

where ϑ denotes the step function and \mathbf{n} is the unit surface normal vector pointing into the device. This type of boundary conditions leads to additional entries in the system matrix due to the surface boundary integrals. Consequently, the scheme needs to be adjusted and written in the form

$$\mathbf{S}_h = \mathbf{S}_h^{\text{inner}} + \mathbf{S}_h^{\text{contact}}, \quad (4.30)$$

where $\mathbf{S}_h^{\text{inner}}$ contains the discretized equations for all interior points as given by (4.21), (4.27) or (4.29), and $\mathbf{S}_h^{\text{contact}}$ consists of the discretized contact boundary terms. Since the number of contact boundary points is much smaller than the total number of grid points N , the sparse matrix $\mathbf{S}_h^{\text{contact}}$ can be set up without compression scheme and the additional memory requirements are negligible.

As can be easily verified, $\mathbf{S}_h^{\text{contact}}$ can also be written as a sum of Kronecker products. Consequently, the following discussions are based on the case of Dirichlet boundary conditions, but are also applicable to the more general case including Robin-type boundary conditions, which only add additional summands.

4.5 Solution of the Linear System

The system matrix representation introduced in the previous sections is of use only if the resulting scheme can be solved without recovering the full matrix again. Such a reconstruction is, in principle, necessary if direct solvers such as the Gauss algorithm are used, because the matrix structure is altered in a way that destroys the block structure. In contrast, for many popular iterative solvers from the family of Krylov methods, it is usually sufficient to provide matrix-vector multiplications. Therefore, methods to compute the matrix-vector product $\mathbf{S}_h \mathbf{x}$ for a given vector \mathbf{x} are discussed first.

Given a system matrix of the form (4.21) or (4.27), it is well known that a row-by-row reconstruction of the compressed matrix \mathbf{S}_h for the matrix-vector product is not efficient.

Therefore, the vector \mathbf{x} is decomposed into N blocks of size $(L+1)^2$ by

$$\mathbf{x} = \begin{pmatrix} \mathbf{x}_1 \\ \vdots \\ \mathbf{x}_N \end{pmatrix} = \sum_{j=1}^N \mathbf{e}_j \otimes \mathbf{x}_j, \quad (4.31)$$

where \mathbf{e}_j is the j -th column vector of the identity matrix. The matrix-vector product can now be written as

$$\mathbf{S}\mathbf{x} = \left[\sum_{i=1}^p \mathbf{Q}_i \otimes \mathbf{R}_i \right] \left[\sum_{j=1}^N \mathbf{e}_j \otimes \mathbf{x}_j \right] \quad (4.32)$$

$$= \sum_{i=1}^p \sum_{j=1}^N (\mathbf{Q}_i \mathbf{e}_j) \otimes (\mathbf{R}_i \mathbf{x}_j). \quad (4.33)$$

Here, the product $\mathbf{Q}_i \mathbf{e}_j$ is simply the j -th column of \mathbf{Q}_i .

In the case of spherical energy bands, it can be shown that the matrix-vector multiplication requires slightly less computational effort than the uncompressed case [87]. As discussed in Sec. 4.2, nonspherical bands lead to a larger number of summands, thus leading to a higher computational effort for the matrix-vector multiplications compared to the uncompressed case. Nevertheless, the additional computational effort is increased only moderately, while the memory requirements can be reduced significantly.

Recent publications report the elimination of odd order unknowns in a preprocessing step [42, 53]. Moreover, it has been shown that for a first-order expansion the system matrix after elimination of odd order unknowns is an M -matrix [42]. Furthermore, numerical experiments indicate a considerable improvement in the convergence of iterative solvers. However, for a matrix structure as given by (4.29), a direct elimination of odd order unknowns would destroy the representation of the system matrix \mathbf{S}_h as a sum of Kronecker products. Writing the system as

$$\mathbf{S}_h \mathbf{f} = \begin{pmatrix} \mathbf{S}_h^{ee} & \mathbf{S}_h^{eo} \\ \mathbf{S}_h^{oe} & \mathbf{S}_h^{oo} \end{pmatrix} \begin{pmatrix} \mathbf{f}^e \\ \mathbf{f}^o \end{pmatrix} = \begin{pmatrix} \mathbf{r}^e \\ \mathbf{r}^o \end{pmatrix} \quad (4.34)$$

with the vector of unknowns \mathbf{f} split into \mathbf{f}^e and \mathbf{f}^o as unknowns associated with even and odd order harmonics respectively and analogously for the right hand side vector \mathbf{r} , the elimination of odd order unknowns is carried out using the Schur complement:

$$(\mathbf{S}_h^{ee} - \mathbf{S}_h^{eo}(\mathbf{S}_h^{oo})^{-1}\mathbf{S}_h^{oe})\mathbf{f}^e = \mathbf{r}^e - \mathbf{S}_h^{eo}(\mathbf{S}_h^{oo})^{-1}\mathbf{r}^o. \quad (4.35)$$

According to Thm. 3, \mathbf{S}_h^{oo} is a diagonal matrix, thus the inverse is directly available. The other matrix-vector products are carried out as discussed in the beginning of this section. Note that the matrix $\mathbf{S}_h^{ee} - \mathbf{S}_h^{eo}(\mathbf{S}_h^{oo})^{-1}\mathbf{S}_h^{oe}$ is never set up explicitly.

In contrast to a matrix-vector multiplication with the full system matrix \mathbf{S}_h , where the proposed matrix compression scheme requires approximately the same computational effort, a matrix-vector multiplication with the condensed matrix $(\mathbf{S}_h^{ee} - \mathbf{S}_h^{eo}(\mathbf{S}_h^{oo})^{-1}\mathbf{S}_h^{oe})$ is more expensive than a matrix-vector multiplication with a fully set up condensed matrix. The penalty is quantified in Sec. 4.6.

With a system matrix representation of the form (4.21), the total memory needed for the SHE equations is essentially given by the memory required for the unknowns, which adds

L	S	$\sum Q_i \otimes R_i$	Unknowns
1	3.7 MB	4.7 MB	0.2 MB
3	28.4 MB	4.7 MB	1.4 MB
5	83.1 MB	4.7 MB	3.5 MB
7	168 MB	4.8 MB	6.6 MB
9	263 MB	4.8 MB	10.7 MB
11	470 MB	4.8 MB	15.7 MB
13	709 MB	4.9 MB	21.6 MB

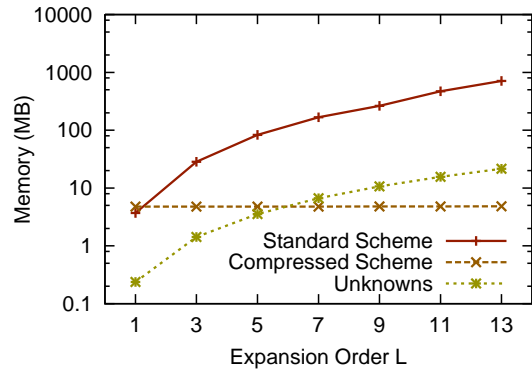


Figure 4.1: Memory requirements for the uncompressed and the compressed system matrix compared to the memory needed for the unknowns for different expansion orders L on a grid in the three-dimensional (\mathbf{x}, H) -space with $5 \times 50 \times 50$ nodes.

another perspective on the selection of the iterative solver. Since $\mathbf{\Gamma}_{l,m}^{l',m'} \neq \mathbf{\Gamma}_{l',m'}^{l,m}$, the system matrix \mathbf{S}_h is not symmetric. Moreover, numerical experiments indicate that the matrix \mathbf{S}_h is indefinite, thus many popular solvers cannot be used. A popular solver for indefinite problems is GMRES [89,112], which is typically restarted after, say, s steps and denoted by GMRES(s). Since GMRES has been used in recent publications on SHE simulations [42,53], it deserves a closer inspection. For a system with N' unknowns, the memory required by GMRES(s) during the solution process is $\mathcal{O}(sN')$. In typical applications, in which the system matrix is uncompressed, this additional memory approximately equals the amount of memory needed for the storage of the system matrix, hence it is not a major concern. However, with the system matrix representation (4.6) the memory needed for the unknowns is dominant, thus the additional memory for GMRES(s) directly pushes the overall memory requirements from $\mathcal{O}(NL^2)$ to $\mathcal{O}(sNL^2)$. The number of steps s is typically chosen between 20 and 30 as smaller values may lead to smaller convergence rates or the solver may even fail to converge within a reasonable number of iterations. Hence, it is concluded that GMRES(s) is too expensive for SHE simulations when using the representation (4.6). Instead, iterative solvers with smaller memory consumption such as BiCGStab [102] should be used.

4.6 Results

In this section execution times and memory requirements of the Kronecker product representation (4.6) using a single core of a machine with a Core 2 Quad 9550 CPU are reported. To simplify wording, the representation (4.6) will be referred to as matrix compression scheme. All simulations were carried out for a stationary two-dimensional device on a regular staggered grid with $5 \times 50 \times 50$ nodes in (\mathbf{x}, H) -space for various expansion orders. Spherical energy bands were assumed and the H -transform and MEDS were used for stabilization. A fixed potential distribution was applied to the device to obtain comparable results. For self-consistency with the Poisson equation using a Newton scheme, similar results can in principle be obtained by application of the matrix compression scheme to the Jacobian.

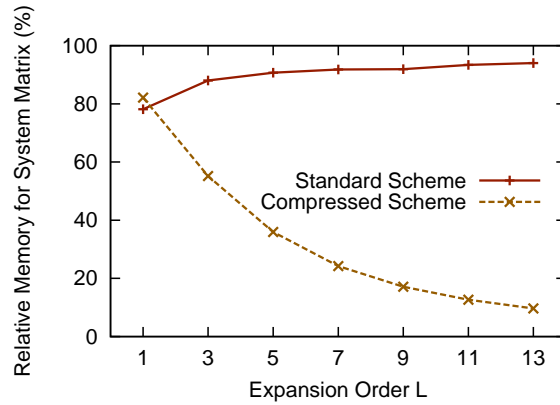


Figure 4.2: Memory used for the uncompressed and the compressed system matrix for different expansion orders L on a three-dimensional (\mathbf{x}, H) -grid with 12 500 nodes.

L	Full system		Condensed	
	S	compr.	S_{cond}	compr.
1	3.9	7.4	0.2	9.2
3	28.4	19.3	4.0	17.9
5	73.9	53.2	15.7	48.9
7	134.8	98.3	36.5	92.2
9	228.1	160.7	68.2	149.8

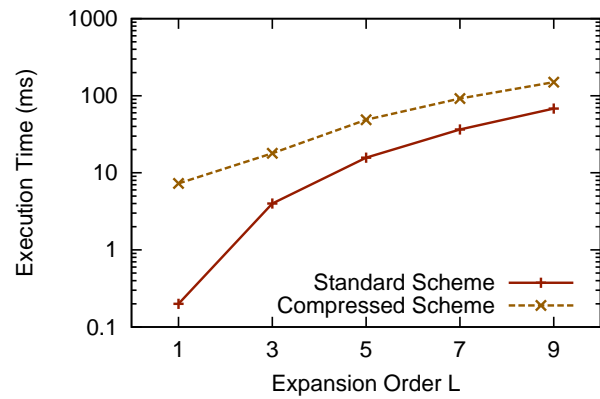


Figure 4.3: Comparison of execution times (milliseconds) for matrix-vector multiplication at different expansion orders L for the fully set up system matrix and the proposed compressed matrix scheme. Both the full system of linear equations and the condensed system with odd order unknowns eliminated in a preprocessing step are compared.

First, memory requirements for the storage of the system matrix are compared. The total number of entries stored in the matrix were extracted, multiplied by three to account for row and column indices. Eight bytes per entry for double precision are used. In this way, the influence of different sparse matrix storage schemes is eliminated. The results in Fig. 4.1 and Fig. 4.2 clearly demonstrate the asymptotic advantage of (4.6): While no savings are observed at $L = 1$, memory savings of a factor of 18 are obtained already at an expansion order of $L = 5$. At $L = 13$, this factor grows to 145. In particular, the memory requirement for the matrix compression scheme shows only a weak dependence on L and is determined only by the additional memory needed for the coupling matrices \mathbf{R}_i in (4.14)-(4.20). With increasing expansion order L , the additional memory requirements for the compressed scheme grow quadratically with L because of the $(L + 1)^2$ spherical harmonics of degree smaller or equal to L . Even at $L = 13$ the additional memory compared to $L = 1$ is less than one megabyte. Consequently, the memory used for the unknowns dominates already at moderate values of L , cf. Fig. 4.1 and Fig. 4.2.

L	GMRES(50)	GMRES(30)	GMRES(10)	BiCGStab	Unknowns
1	10.2 MB	6.2 MB	2.2 MB	1.2 MB	0.2 MB
3	71.4 MB	43.4 MB	15.4 MB	8.4 MB	1.4 MB
5	178.5 MB	108.5 MB	38.5 MB	21.0 MB	3.5 MB
7	336.6 MB	204.7 MB	72.6 MB	39.6 MB	6.6 MB
9	545.7 MB	331.7 MB	117.7 MB	64.2 MB	10.7 MB
11	800.7 MB	486.7 MB	172.7 MB	93.5 MB	15.7 MB
13	1101.6 MB	669.6 MB	237.6 MB	129.6 MB	21.6 MB

Table 4.1: Additional memory requirements of the linear solvers GMRES(s) with different values of s and BiCGStab compared to the memory needed for the unknowns, cf. Fig. 4.4.

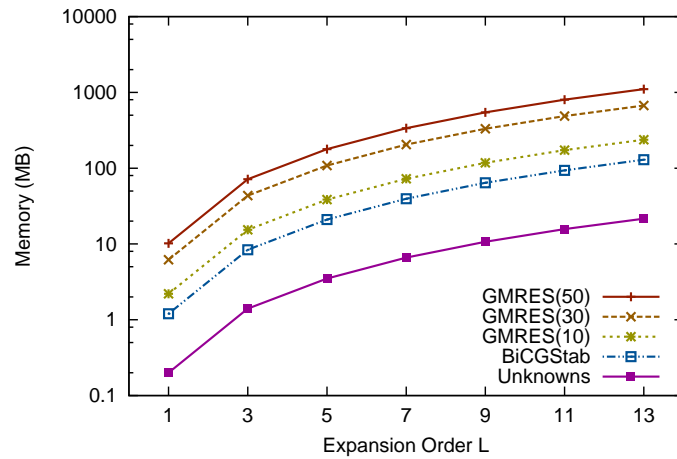


Figure 4.4: Additional memory requirements of the linear solvers GMRES(s) with different values of s and BiCGStab as given in Tab. 4.1.

Execution times for matrix-vector multiplications are compared in Fig. 4.3 for the case of a full system matrix and the system matrix with odd expansion orders eliminated. For the lowest expansion order $L = 1$, the matrix compression does not pay off and execution times are by a factor of two larger than for the standard storage scheme. This is due to the additional structural overhead of the compressed scheme at expansion order $L = 1$, where no compression effect occurs. However, for larger values of L , the matrix compression scheme leads to faster matrix-vector multiplications with the full system of linear equations. An additional performance gain of about ten percent is observed. Comparing execution times for the condensed system, where odd order unknowns have been eliminated in a preprocessing step, the runtime penalty for matrix-vector multiplication is a factor of 15 at $L = 1$, but in this case there is no compression effect anyway. At $L = 5$, the runtime penalty is only a factor of three and drops to slightly above two at $L = 13$. In conclusion, the matrix compression scheme allows for a trade-off between memory consumption and execution time, where the memory reduction is much larger than the penalty on execution times.

A comparison of the additional memory required by GMRES(50), GMRES(30), GMRES(10) and BiCGStab is shown in Tab. 4.1 and Fig. 4.4. As expected, GMRES leads to higher memory requirements than many other Krylov methods such as BiCGStab. For GMRES(s), $s + 1$ auxiliary vectors of the same length as the vector of unknowns are used, while BiCGStab uses six auxiliary vectors of that size. It can clearly be seen that the memory required by GMRES(50) is by one order of magnitude larger than the memory needed for the compressed system (i.e. second and third column in Fig. 4.1) and BiCGStab. On the other hand, without system matrix compression, the additional memory needed by GMRES(50) is comparable to the memory needed for the system matrix and is thus less of a concern.

Chapter 5

SHE on Unstructured Grids

Up to now, the SHE equations have been derived and investigated on the continuous level. Generic discretization schemes were considered in the previous chapter and a system matrix compression scheme was developed. It is thus time to consider the discretization of the equations, which is the focus of this chapter. To make the chapter as self-contained as possible, the necessary prerequisites about the box integration scheme and the generation of suitable unstructured grids are presented first.

5.1 The Box Integration Scheme

The box integration scheme is a widely used discretization scheme, particularly for semiconductor device simulation and for fluid dynamics. Outside the field of microelectronics it is typically called finite volume method [4, 64]. The main advantage of the box integration scheme is its local conservation property, thus it is particularly suited for the discretization of conservation equations such as the drift-diffusion equations. The box integration can be derived in different ways. In this section a rather direct approach is taken, while a mathematically cleaner approach can be found in [4], where connections with the finite element method are more pronounced.

In the following, the box integration scheme is explained by example of the discretization of the Poisson equation on the domain Ξ . Consider

$$\begin{aligned}\Delta\psi &= f \quad \text{in } \Xi \subset \mathbb{R}^n, \\ \psi &= 0 \quad \text{on } \partial\Xi,\end{aligned}$$

where homogeneous Dirichlet boundary conditions are assumed for simplicity. Given a tessellation $\mathcal{B} = (B_i)_{i=1}^N$ of the domain Ξ into small boxes B_i , a local integral form of the Poisson equation is

$$\int_{B_i} \Delta\psi \, dV = \int_{B_i} f \, dV \quad \text{on } \Xi, \quad \int_{\partial B_i \cap \partial\Xi} \psi \, dA = 0.$$

Using Gauss' Theorem, the problem is recast into

$$\int_{\partial B_i} \nabla\psi \cdot \mathbf{n} \, dA = \int_{B_i} f \, dV \quad \text{on } \Xi, \quad \int_{\partial B_i \cap \partial\Xi} \psi \, dA = 0,$$

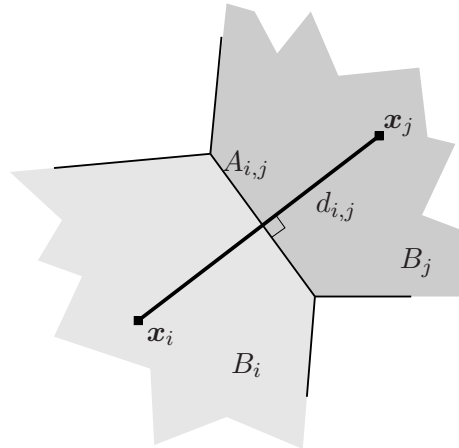


Figure 5.1: Schematic of a mesh for a box integration scheme. The length between vertices \mathbf{x}_i and \mathbf{x}_j is $d_{i,j}$, while the area of the interface between boxes B_i and B_j is $A_{i,j}$.

where \mathbf{n} denotes the unit normal vector to the boundary of the box in outward direction.

Let the connecting line $[\mathbf{x}_i, \mathbf{x}_j]$ of the box centers \mathbf{x}_i and \mathbf{x}_j of the boxes B_i and B_j be perpendicular to the box boundary, cf. Fig. 5.1. A first-order approximation of the normal derivative of the potential is a differential quotient along the connecting line $[\mathbf{x}_i, \mathbf{x}_j]$ of length $d_{i,j}$. Thus, one obtains the discrete local conservation equations

$$\sum_j \frac{\psi_j - \psi_i}{d_{i,j}} A_{i,j} = f(\mathbf{x}_i) V_i, \quad (5.1)$$

where V_i denotes the volume of the box B_i and the interface area $A_{i,j}$ is zero if the boxes B_i and B_j do not have a common boundary. Note that the transition from the continuous to the discrete formulation requires an approximation of fluxes through the box boundaries. There exists a large number of different flux approximation schemes, an overview can be found e.g. in the textbook of LeVeque [64].

To summarize, the main ingredients of a box integration scheme are as follows:

- Integrate the equation to be discretized over each box B_i of the tessellation \mathcal{B} of the domain Ξ .
- Use Gauss' Theorem to recast the volume integral as an integral over the box boundary.
- Discretize the flux through the box interfaces.
- Compute the interface integrals over the discretized fluxes either directly, or via a suitable numerical integration scheme.
- Solve the resulting system of linear equations.

5.2 Construction of Boxes

Two families of tessellations \mathcal{B} of the domain Ξ are frequently used with a box integration scheme. The first family is referred to as *vertex-centered*, where the unknowns and the

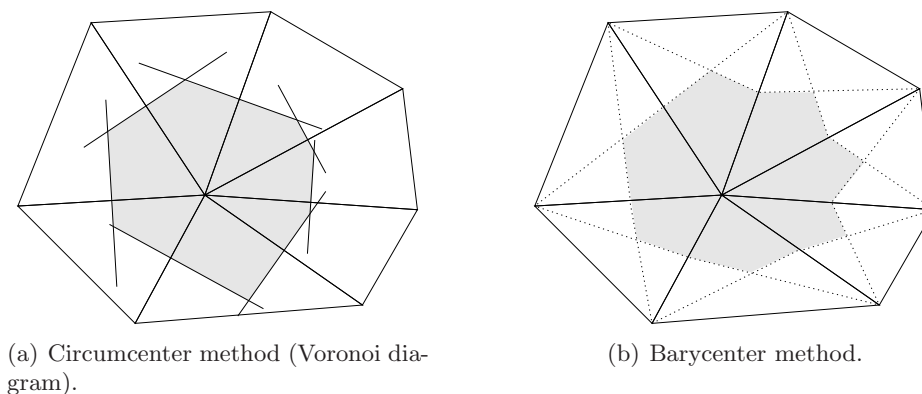


Figure 5.2: Two methods for the construction of a dual box tessellation from a triangulation.

boxes B_i are associated with the vertices of another mesh. The second family is based on a *cell-centered* approach, where the unknowns are directly associated with the cells of the mesh (e.g. triangles, tetrahedra, hexahedra), which also constitute the boxes B_i . Other formulations such as *cell-vertex* methods exist [4], but are not further addressed in the following. The respective preference of a certain family is often based on the availability of good flux approximation schemes for the problem at hand. Due to the wide-spread use of vertex-centered box integration schemes in the field of semiconductor device simulation, the focus in this section is on this first family. In particular, the box integration scheme for the SHE equations presented in the next section is based on a vertex-centered construction.

While a *cell-centered* box integration scheme can be carried out on virtually any mesh, the *vertex-centered* method is a-priori based on a different mesh and the boxes in \mathcal{B} need to be constructed first. The following two constructions are common [4]:

- When employing *Voronoi diagrams* (aka. *circumcenter method*) [71], the boxes are convex sets associated with a given set of disjoint points $X = \{\mathbf{x}_1, \dots, \mathbf{x}_m\}$. Each box $B_i \in \mathcal{B}$ consists of points closer to \mathbf{x}_i than to any other point of X , i.e.

$$B_i = \{ \mathbf{p} \in \Xi \mid \|\mathbf{p} - \mathbf{x}_i\| \leq \|\mathbf{p} - \mathbf{x}_j\| \quad \forall j \neq i, j \in \{1, \dots, m\} \} . \quad (5.2)$$

An interesting fact is that each Voronoi diagram is the dual of a triangulation, where the vertices are exactly the points of X . Here, a triangulation does not necessarily refer to a triangulation in two spatial dimensions, but may also refer to the general case of a decomposition of the n -dimensional space into n -simplices. Note that not every triangulation is the dual of a Voronoi diagram: If the circumsphere of a cell T includes vertices other than those of T , then the triangulation is not the dual of a Voronoi diagram. Triangulations, which are the dual of a Voronoi diagram, are called *Delaunay triangulations*. Unlike for the unstructured case, Voronoi diagrams can be derived directly from structured grids, particularly meshes consisting of rectangles and bricks.

The advantage of Voronoi diagrams is that the interfaces between boxes are perpendicular to the connections between the respective vertices, thus allowing for the simple approximation of the normal flux. However, the generation of underlying Delaunay

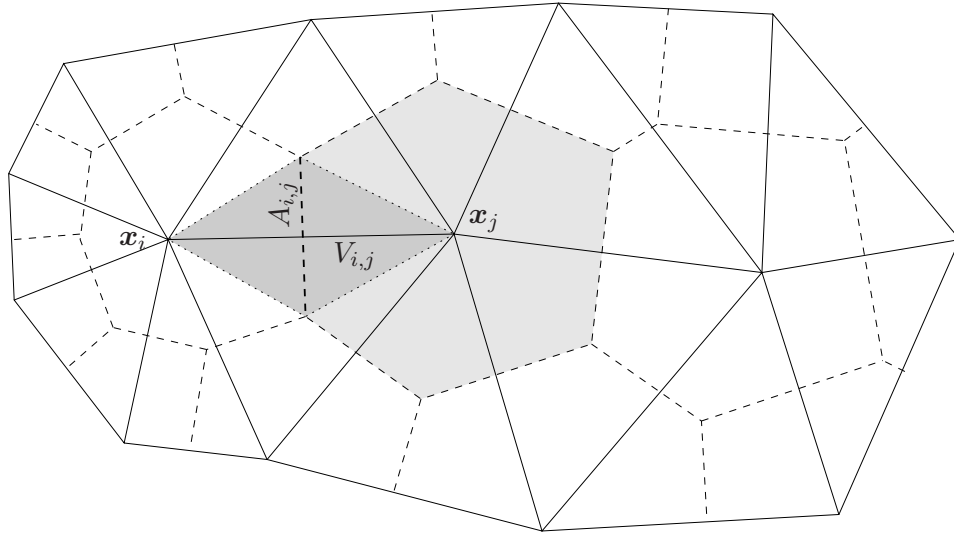


Figure 5.3: Schematic of a triangular Delaunay mesh and its dual Voronoi diagram, where the box containing vertex \mathbf{x}_j is highlighted. The Voronoi volume fraction $V_{i,j}$ and the interface area $A_{i,j}$ are associated with each edge $[\mathbf{x}_i, \mathbf{x}_j]$

triangulations results in additional effort needed for mesh generation on the one hand and mesh refinement on the other hand [94, 113]. In addition, the computation of Voronoi diagrams becomes increasingly challenging in higher spatial dimensions.

- For the *barycenter method* [4] the barycenters of the triangles are connected with the midpoint of the edges to obtain the dual box tessellation (cf. Fig. 5.2(b)). An advantage is that the method can be, unlike others, algorithmically generalized to higher dimensions with reasonable effort and without further requirements on the mesh. However, in comparison to the circumcenter method the number of facets of each box is larger, and the boxes are not necessarily convex.

In order to employ a box integration scheme, there is usually no need to set up the boxes explicitly. As motivated in Sec. 5.1, it is usually sufficient to have the box volumes V_i and the interface areas $A_{i,j}$ available. For the discretization of an additional advective term, the box volume fraction $V_{i,j}$ associated with the interface $A_{i,j}$ is also required, cf. Fig. 5.3. Since the computation of these values for triangular and tetrahedral meshes is only poorly documented in the relevant literature, the respective algorithms are detailed in the following.

Since Voronoi quantities are required based on connections between \mathbf{x}_i and \mathbf{x}_j , it is sufficient to provide an algorithm for the computation of the respective quantities for each edge $[\mathbf{x}_i, \mathbf{x}_j]$. The Voronoi information for the full domain is then obtained by an iteration over all edges of the domain.

Algorithm 3 (Computation of Voronoi quantities for a triangular Delaunay mesh). *Requirements: Triangular Delaunay mesh with all circumcenters in the interior of the mesh*
Input: edge $[\mathbf{x}_i, \mathbf{x}_j]$

- If there are two adjacent cells, compute the two circumcenters \mathbf{c}_1 and \mathbf{c}_2 .
- If there is one adjacent cell, compute the circumcenter \mathbf{c}_1 and set \mathbf{c}_2 to the midpoint of the edge.

- Compute the interface area $A_{i,j} \leftarrow |\mathbf{c}_1 - \mathbf{c}_2|$.
- Compute the edge length $d_{i,j} \leftarrow |\mathbf{x}_i - \mathbf{x}_j|$.
- Compute the box volume fraction $V_{i,j} \leftarrow A_{i,j}d_{i,j}/4$.

Return $A_{i,j}, d_{i,j}, V_{i,j}$.

The box volumes V_i for the box associated with vertex \mathbf{x}_i is obtained by a summation over all box fractions, i.e. $V_i = \sum_j V_{i,j}$. The three-dimensional equivalent is slightly more involved:

Algorithm 4 (Computation of Voronoi quantities for a tetrahedral Delaunay mesh). *Requirements: Triangular Delaunay mesh with all circumcenters in the interior of the mesh*
Input: edge $[\mathbf{x}_i, \mathbf{x}_j]$

- Compute the edge length $d_{i,j} \leftarrow |\mathbf{x}_i - \mathbf{x}_j|$.
- Set $A_{i,j} \leftarrow 0$.
- Set $V_{i,j} \leftarrow 0$.
- For each adjacent cell $[\mathbf{x}_i, \mathbf{x}_j, \mathbf{x}_k, \mathbf{x}_l]$, compute the circumcenter \mathbf{c}_r .
- Set $\mathbf{p} \leftarrow \sum_r \mathbf{c}_r/N$, where N is the number of adjacent cells.
- For each facet $[\mathbf{x}_i, \mathbf{x}_j, \mathbf{x}_k]$ adjacent to edge $[\mathbf{x}_i, \mathbf{x}_j]$, do
 - If there are two adjacent cells, let \mathbf{c}_1 and \mathbf{c}_2 denote the two circumcenters.
 - If there is one adjacent cell, let the circumcenter of the cell be given by \mathbf{c}_1 and set \mathbf{c}_2 to the circumcenter of the facet.
 - Compute the area A of the triangle $[\mathbf{p}, \mathbf{c}_1, \mathbf{c}_2]$.
 - Update the interface area $A_{i,j} \leftarrow A_{i,j} + A$.
 - Update the box volume fraction $V_{i,j} \leftarrow V_{i,j} + Ad_{i,j}/6$.

Return $A_{i,j}, d_{i,j}, V_{i,j}$.

Note that the point \mathbf{p} is used for the computation of the polygon defined by the circumcenters. Again, the box volumes V_i are obtained by a summation over all $V_{i,j}$ related to a vertex \mathbf{x}_i .

It has to be noted that the Delaunay property does not ensure that the circumcenters of all cells are inside the mesh, i.e. located inside or at the boundary of any cell of the mesh. Consequently, cells with regular shapes are required near the mesh boundary in order to fulfill the requirements of the two algorithms above, cf. Fig. 5.4. If this criterion is not strictly fulfilled, the system matrix \mathbf{S} will be disturbed by, say, a matrix \mathbf{D} . Similar to the analysis of round-off errors, the difference of the solution \mathbf{y} of the perturbed system with respect to the true solution \mathbf{x} is bounded by

$$\frac{\|\mathbf{y} - \mathbf{x}\|}{\|\mathbf{x}\|} \leq \kappa(\mathbf{S}) \frac{\|\mathbf{D}\|}{\|\mathbf{S}\|}, \quad (5.3)$$

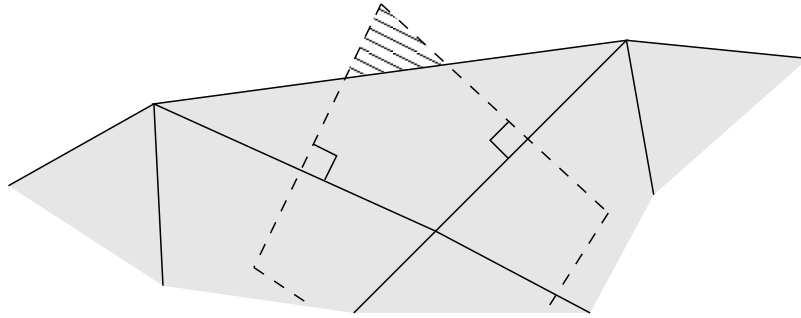


Figure 5.4: Flat triangles at the domain boundary can lead to circumcenters outside the simulation domain. As a consequence, the volumes and interface areas of dual boxes extend outside the simulation domain (hatched area), leading to systematic errors in the assembled system of linear equations.

where $\kappa(\mathbf{S})$ denotes the condition number of \mathbf{S} and suitable vector and matrix norms are chosen [27]. Consequently, violations in the range of round-off errors can be justified from a mathematical point of view. Higher violations are acceptable if the condition number is known to be small and only low accuracy in the solution vector is required. In practice, however, even much stronger violations than those justified from the analytical bound (5.3) can result in insignificant errors in the solution vector due to high regularity of the underlying formation. Nevertheless, the regularity of the mesh near the boundary is particularly important for semiconductor device simulations with dominant current flow near the surface, as it is the case e.g. in a MOSFET.

The generation of Delaunay triangulations of good quality for arbitrary domains is a challenging task already in two dimensions [94], and particularly in three dimensions [17]. The meshes used throughout this thesis are generated by Netgen [91], which is capable of generating two- and three-dimensional Delaunay triangulations. A further discussion of the peculiarities of Delaunay mesh generation and refinement is, however, beyond the scope of this thesis.

The SHE method requires an energy coordinate in addition to the spatial coordinate. In principle, one may generate a mesh directly for the (\mathbf{x}, H) -space, but this is impractical for two reasons. First, the author is not aware of the existence any four-dimensional mesh generators capable of handling complex domains. Second, the essence of the H -transform in Sec. 2.3 is the possibility to align the grid with the trajectory of electrons in free flight given by planes of constant total energy H . Consequently, the embedding of a mesh from the spatial domain to the (\mathbf{x}, H) -space by a tensorial prolongation is of advantage. Given discrete total energies $H_1 < H_2 < \dots < H_{N_H}$, every vertex \mathbf{x} in the n -dimensional mesh is first embedded in the $n+1$ -dimensional space at location (\mathbf{x}, H_1) . The full $n+1$ -dimensional mesh of prismatic cells is then obtained by repeatedly shifting the three-dimensional mesh along the energy axis to obtain the points (\mathbf{x}, H_2) , (\mathbf{x}, H_3) , \dots , (\mathbf{x}, H_{N_H}) . The procedure is illustrated in Fig. 5.5 for the case of a spatially two-dimensional mesh. Clearly, the energy spacing does not need to be equidistant. Moreover, the computation of Voronoi quantities for the mesh in (\mathbf{x}, H) -space is obtained from Voronoi information in \mathbf{x} -space by a multiplication of the energy spacing.

There is no need for setting up the mesh in (\mathbf{x}, H) -space explicitly, because the additional H coordinate can also be handled implicitly. Since the coupling of different energy levels is

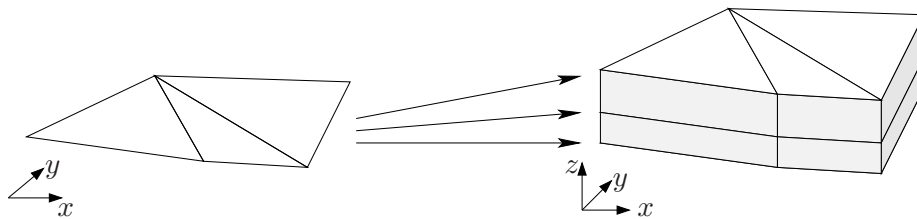


Figure 5.5: A three-dimensional prismatic mesh can be obtained from a two-dimensional mesh by appropriate translations. The two-dimensional cells are then facets of the three-dimensional prism. Here, the remaining facets are obtained by joining corresponding vertices.

local in space, it is more memory efficient to stick with the spatial mesh and to store the total energy values in an array with, say, N_H elements. The respective array index i can then be used to identify e.g. the vertex (\mathbf{x}, H_i) , even though only the vertex \mathbf{x} is explicitly stored. Since this approach leads to better compatibility with other macroscopic transport models, which do not require an additional energy coordinate, this implicitly tensorial representation is used in *ViennaSHE*. The price to pay is an additional effort required for a visualization of the computed distribution function in one and two spatial dimensions, because the mesh in (\mathbf{x}, H) -space needs to be made available then.

5.3 Box Integration for SHE

With the discussion of the box integration scheme in Sec. 5.1 and the computation of Voronoi information from Sec. 5.2, the discretization of the SHE equations (2.34) and (2.35) can now be tackled. For the sake of clarity, the SHE method for spherical energy bands in steady-state is considered. The general case is obtained without additional difficulties.

Due to the use of MEDS for stabilization, cf. Sec. 2.3, two different sets of equations (2.34) and (2.35) need to be considered. The even-order equations are discretized directly on the boxes B_i of the underlying Voronoi tessellation \mathcal{B} , while the odd-order equations are associated with the dual tessellation $\tilde{\mathcal{B}}$ centered at the interfaces between the boxes, cf. Fig. 5.6. Note that the set $\tilde{\mathcal{B}}$ is obtained by taking the union over all adjoint boxes $B_{i,j}$ of all boxes B_i . The volume of adjoint the boxes $B_{i,j} \in \tilde{\mathcal{B}}$ overlapping the neighboring boxes $B_i \in \mathcal{B}$ and $B_j \in \mathcal{B}$ is given by $2V_{i,j}$, cf. Fig. 5.3 and Sec. 5.2. Consequently, the even-order expansion coefficients are associated with the vertices of the mesh, while the odd-order expansion coefficients are associated with the edge midpoints. More precisely, the discretization of the expansion coefficients reads

$$f_{l,m}(\mathbf{x}, H) = \sum_{i=1}^{|\mathcal{B}|} \sum_{n=1}^{N_H} \alpha_{i,n;l,m} \chi_{B_i}(\mathbf{x}) \chi_{[H_n^-, H_n^+]}(H), \quad l \text{ even}, \quad (5.4)$$

$$f_{l,m}(\mathbf{x}, H) = \sum_{j=1}^{|\tilde{\mathcal{B}}|} \sum_{n=1}^{N_H} \beta_{j,n;l,m} \chi_{\tilde{B}_j}(\mathbf{x}) \chi_{[H_n^-, H_n^+]}(H), \quad l \text{ odd}, \quad (5.5)$$

where χ_{B_i} denotes the indicator function of the box B_i , $\chi_{[H_n^-, H_n^+]}$ is the indicator function of the energy interval for the N_H discrete energies H_n with lower and upper bound H_n^- and H_n^+ , and $\tilde{\mathcal{B}}$ refers to the set of adjoint boxes \tilde{B}_i with indicator function $\chi_{\tilde{B}_i}$. The unknowns

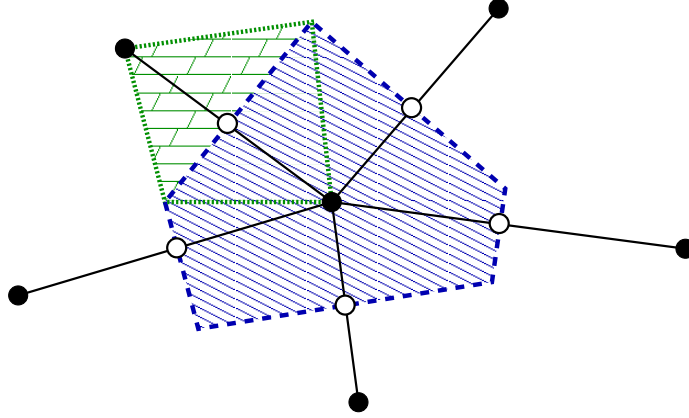


Figure 5.6: Schematic view of the box discretization for SHE. Even-order unknowns are associated with vertices (filled circles, blue box $B_i \in \mathcal{B}$), while odd-order unknowns are associated with edges (open circles, green box $B_{i,j} \in \tilde{\mathcal{B}}$).

of the resulting linear system of equations after discretization are the coefficients $\alpha_{i,n;l,m}$ and $\beta_{i,n;l,m}$, where the $\beta_{i,n;l,m}$ are eliminated in a preprocessing step of the linear solver as discussed in Sec. 4.3.

5.3.1 Discretization of the Even-Order Equations

Following the box integration procedure from Sec. 5.1, integration over energy from H_n^- to H_n^+ and over a box B_i given on the spatial grid leads to

$$\begin{aligned} & \int_{H_n^-}^{H_n^+} \int_{B_i} \nabla \mathbf{x} \cdot \mathbf{j}_{l,m}^{l',m'} f_{l',m'} - \mathbf{F} \cdot \mathbf{\Gamma}_{l,m}^{l',m'} f_{l',m'} dV dH \\ &= \frac{1}{Y_{0,0}} \sum_{\eta} \int_{H_n^-}^{H_n^+} \int_{B_i} \left[Z_{l,m} \sigma_{\eta}(\mathbf{x}, H \pm \hbar\omega_{\eta}, H) f_{0,0}(\mathbf{x}, H \pm \hbar\omega_{\eta}) Z_{0,0}(H \pm \hbar\omega_{\eta}) \right. \\ & \quad \left. - f_{l,m} Z_{l,m} \sigma_{\eta}(\mathbf{x}, H, H \mp \hbar\omega_{\eta}) Z_{0,0}(H \mp \hbar\omega_{\eta}) \right] dV dH . \end{aligned} \quad (5.6)$$

The first term on the left hand side is transformed to a surface integral using Gauss' Theorem, and then the integrals on the left hand side are decomposed into the individual intersections with the neighboring adjoint boxes $B_{i,j}$:

$$\begin{aligned} & \sum_{B_{i,j} \text{ of } B_i} \int_{H_n^-}^{H_n^+} \left[\int_{\partial B_i \cap B_{i,j}} \mathbf{j}_{l,m}^{l',m'} f_{l',m'} \cdot \mathbf{n}_{i,j} dA - \int_{B_i \cap B_{i,j}} \mathbf{F} \cdot \mathbf{\Gamma}_{l,m}^{l',m'} f_{l',m'} dV \right] dH \\ &= \frac{1}{Y_{0,0}} \sum_{\eta} \int_{H_n^-}^{H_n^+} \int_{B_i} \left[Z_{l,m} \sigma_{\eta}(\mathbf{x}, H \pm \hbar\omega_{\eta}, H) f_{0,0}(\mathbf{x}, H \pm \hbar\omega_{\eta}, t) Z_{0,0}(H \pm \hbar\omega_{\eta}) \right. \\ & \quad \left. - f_{l,m} Z_{l,m} \sigma_{\eta}(\mathbf{x}, H, H \mp \hbar\omega_{\eta}) Z_{0,0}(H \mp \hbar\omega_{\eta}) \right] dV dH , \end{aligned} \quad (5.7)$$

where $\mathbf{n}_{i,j}$ denotes the outward pointing unit vector with respect to B_i and perpendicular to the common interface of B_i and B_j . Since for even l the coupling terms $\mathbf{j}_{l,m}^{l',m'}$ and $\mathbf{\Gamma}_{l,m}^{l',m'}$ take

according to Thm. 1 nonzero values for odd l' only, and the scattering operator exclusively couples terms of the same order (l, m) , the discretization (5.5) can directly be inserted:

$$\begin{aligned} \sum_{B_{i,j} \text{ of } B_i} \beta_{i,n;l',m'} & \left[A_{i,j} \mathbf{n}_{i,j} \cdot \int_{H_n^-}^{H_n^+} \mathbf{j}_{l,m}^{l',m'} dH - V_{i,j} \mathbf{F}|_{B_{i,j}} \cdot \int_{H_n^-}^{H_n^+} \mathbf{\Gamma}_{l,m}^{l',m'} dH \right] \\ & = \frac{1}{Y_{0,0}} \sum_{\eta} \int_{H_n^-}^{H_n^+} \left[Z_{l,m} \sigma_{\eta}(\mathbf{x}, H \pm \hbar\omega_{\eta}, H) \alpha_{i,n \pm n'_{\eta}; 0,0} Z_{0,0}(H \pm \hbar\omega_{\eta}) \right. \\ & \quad \left. - \alpha_{i,n;l,m} Z_{l,m} \sigma_{\eta}(\mathbf{x}, H, H \mp \hbar\omega_{\eta}) Z_{0,0}(H \mp \hbar\omega_{\eta}) \right] V_i dH, \end{aligned} \quad (5.8)$$

where $\mathbf{j}_{l,m}^{l',m'}$, $\mathbf{\Gamma}_{l,m}^{l',m'}$ as well as the scattering rates are assumed to be homogeneous over the device, the force \mathbf{F} is approximated by a constant vector $\mathbf{F}_{i,j}$ on $B_{i,j}$ and where n'_{η} refers to a suitable index shift such that $H_{n+n'_{\eta}} \simeq H_n + \hbar\omega_{\eta}$. Typically, discrete energies are chosen as fractions of $\hbar\omega_{\eta}$ such that $H_n + \hbar\omega_{\eta}$ is again a discrete energy. It is noteworthy that the approximation of the force term by a constant vector over $B_{i,j}$ is mostly a matter of convenience. One may also use more accurate representations, but the price to pay is increased computational effort for the evaluation of the integral over $B_{i,j}$. A dimensional splitting has been used by Hong *et al.* [42], which can be seen in this context as considering only the projection $\mathbf{F} \cdot \mathbf{n}_{i,j}$ for the integration over $B_{i,j}$.

A slight rearrangement for better exposition of the unknowns $\alpha_{i,n;l,m}$ and $\beta_{i,n;l,m}$ yields

$$\begin{aligned} \sum_{B_{i,j} \text{ of } B_i} \beta_{j,k;l',m'} & \left[A_{i,j} \mathbf{n}_{i,j} \cdot \int_{H_n^-}^{H_n^+} \mathbf{j}_{l,m}^{l',m'} dH - V_{i,j} \mathbf{F}_{i,j} \cdot \int_{H_n^-}^{H_n^+} \mathbf{\Gamma}_{l,m}^{l',m'} dH \right] \\ & = \alpha_{i,n \pm n'_{\eta}; 0,0} \frac{V_i}{Y_{0,0}} \sum_{\eta} \int_{H_n^-}^{H_n^+} \sigma_{\eta}(\mathbf{x}, H \pm \hbar\omega_{\eta}, H) Z_{l,m} dH \\ & \quad - \alpha_{i,n;l,m} \frac{V_i}{Y_{0,0}} \sum_{\eta} \int_{H_n^-}^{H_n^+} \sigma_{\eta}(\mathbf{x}, H, H \mp \hbar\omega_{\eta}) Z_{0,0}(H \mp \hbar\omega_{\eta}) dH. \end{aligned} \quad (5.9)$$

In the case of spherical energy bands, the integrals on the left hand side can be rewritten using (4.2) and (4.3) as

$$\int_{H_n^-}^{H_n^+} \mathbf{j}_{l,m}^{l',m'} dH = \mathbf{a}_{l,m}^{l',m'} \int_{H_n^-}^{H_n^+} vZ dH, \quad (5.10)$$

$$\int_{H_n^-}^{H_n^+} \mathbf{\Gamma}_{l,m}^{l',m'} dH = \mathbf{b}_{l,m}^{l',m'} \int_{H_n^-}^{H_n^+} \frac{Z}{\hbar|\mathbf{k}|} dH. \quad (5.11)$$

The integrals on the right hand side can be calculated analytically for the parabolic dispersion relation (3.2) and the nonparabolic model (3.3), cf. [42]. When using the full-band modification (3.20), the integral (5.11) simplifies to an evaluation of the full-band data at H_n^- and H_n^+ .

5.3.2 Discretization of the Odd-Order Equations

The discretization of the odd-order projected equations (2.35) is carried out using essentially the same steps as for the even-order equations, but differs in a few technical details. Inte-

gration over the energy interval from H_n^- to H_n^+ and over an adjoint box $B_{i,j}$ overlapping the boxes B_i and B_j leads to

$$\begin{aligned} & \int_{H_n^-}^{H_n^+} \int_{B_{i,j}} \mathbf{j}_{l,m}^{l',m'} \cdot \nabla_{\mathbf{x}} f_{l',m'} + \mathbf{F} \cdot \hat{\mathbf{\Gamma}}_{l,m}^{l',m'} f_{l',m'} dV dH \\ &= \frac{1}{Y_{0,0}} \sum_{\eta} \int_{H_n^-}^{H_n^+} \int_{B_{i,j}} \left[Z_{l,m} \sigma_{\eta}(\mathbf{x}, H \pm \hbar\omega_{\eta}, H) f_{0,0}(\mathbf{x}, H \pm \hbar\omega_{\eta}) Z_{0,0}(H \pm \hbar\omega_{\eta}) \right. \\ & \quad \left. - f_{l,m} Z_{l,m} \sigma_{\eta}(\mathbf{x}, H, H \mp \hbar\omega_{\eta}) Z_{0,0}(H \mp \hbar\omega_{\eta}) \right] dV dH . \end{aligned} \quad (5.12)$$

Assuming $\mathbf{j}_{l,m}^{l',m'}$ to be piecewise constant in each of the adjoint boxes $B_{i,j}$, application of Gauss' Theorem to the first term, and splitting the second integral into the two overlaps with B_i and B_j leads to

$$\begin{aligned} & \int_{H_n^-}^{H_n^+} \left[\int_{\partial B_{i,j} \cap B_i} \mathbf{j}_{l,m}^{l',m'} f_{l',m'} \cdot \mathbf{n} dA + \int_{\partial B_{i,j} \cap B_j} \mathbf{j}_{l,m}^{l',m'} f_{l',m'} \cdot \mathbf{n} dA , \right. \\ & \quad \left. + \int_{B_{i,j} \cap B_i} \mathbf{F} \cdot \hat{\mathbf{\Gamma}}_{l,m}^{l',m'} f_{l',m'} dV + \int_{B_{i,j} \cap B_j} \mathbf{F} \cdot \hat{\mathbf{\Gamma}}_{l,m}^{l',m'} f_{l',m'} dV \right] dH \\ &= \frac{1}{Y_{0,0}} \sum_{\eta} \int_{H_n^-}^{H_n^+} \int_{B_{i,j}} \left[Z_{l,m} \sigma_{\eta}(\mathbf{x}, H \pm \hbar\omega_{\eta}, H) f_{0,0}(\mathbf{x}, H \pm \hbar\omega_{\eta}) Z_{0,0}(H \pm \hbar\omega_{\eta}) \right. \\ & \quad \left. - f_{l,m} Z_{l,m} \sigma_{\eta}(\mathbf{x}, H, H \mp \hbar\omega_{\eta}) Z_{0,0}(H \mp \hbar\omega_{\eta}) \right] dV dH . \end{aligned} \quad (5.13)$$

For odd l , the terms $\mathbf{j}_{l,m}^{l',m'}$ and $\hat{\mathbf{\Gamma}}_{l,m}^{l',m'}$ are nonzero for even l' only. Inserting the expansion (5.4) on the left hand side and (5.5) on the right hand side, one arrives at

$$\begin{aligned} & \alpha_{i,n;l',m'} \int_{H_n^-}^{H_n^+} \left[\int_{\partial B_{i,j} \cap B_i} \mathbf{j}_{l,m}^{l',m'} \cdot \mathbf{n} dA + \int_{B_{i,j} \cap B_i} \mathbf{F} \cdot \hat{\mathbf{\Gamma}}_{l,m}^{l',m'} dV \right] dH \\ & \quad + \alpha_{j,n;l',m'} \int_{H_n^-}^{H_n^+} \left[\int_{\partial B_{i,j} \cap B_j} \mathbf{j}_{l,m}^{l',m'} \cdot \mathbf{n} dA + \int_{B_{i,j} \cap B_j} \mathbf{F} \cdot \hat{\mathbf{\Gamma}}_{l,m}^{l',m'} dV \right] dH \\ &= \beta_{i,n \pm n';0,0} \frac{2V_{i,j}}{Y_{0,0}} \sum_{\eta} \int_{H_n^-}^{H_n^+} Z_{l,m} \sigma_{\eta}(\mathbf{x}, H \pm \hbar\omega_{\eta}, H) Z_{0,0}(H \pm \hbar\omega_{\eta}) dH \\ & \quad - \beta_{i,n;l,m} \frac{2V_{i,j}}{Y_{0,0}} \sum_{\eta} \int_{H_n^-}^{H_n^+} Z_{l,m} \sigma_{\eta}(\mathbf{x}, H, H \mp \hbar\omega_{\eta}) Z_{0,0}(H \mp \hbar\omega_{\eta}) dH , \end{aligned} \quad (5.14)$$

where the scattering rates and the density of states are assumed to be independent of the spatial variable. Since the current density expansion terms $\mathbf{j}_{l,m}^{l',m'}$ are also assumed to be constant within the box $B_{i,j}$, an application of Gauss' Theorem shows

$$\begin{aligned} & \int_{\partial B_{i,j} \cap B_i} \mathbf{j}_{l,m}^{l',m'} \cdot \mathbf{n} dA + \int_{\partial B_{i,j} \cap B_j} \mathbf{j}_{l,m}^{l',m'} \cdot \mathbf{n} dA \\ &= \int_{\partial B_j \cap B_{i,j}} \mathbf{j}_{l,m}^{l',m'} \cdot \mathbf{n}_{j,i} dA + \int_{\partial B_i \cap B_{i,j}} \mathbf{j}_{l,m}^{l',m'} \cdot \mathbf{n}_{i,j} dA , \end{aligned} \quad (5.15)$$

which allows to replace the integration over the boundary of $B_{i,j}$ by two integrations over the interface of the boxes B_i and B_j . This leads with constant force approximations $\mathbf{F}_{i,j}$ over the box $B_{i,j}$ to

$$\begin{aligned}
& \alpha_{i,n;l',m'} \int_{H_n^-}^{H_n^+} \left[A_{i,j} \mathbf{j}_{l,m}^{l',m'} \cdot \mathbf{n}_{j,i} + V_{i,j} \mathbf{F}_{i,j} \cdot \hat{\mathbf{F}}_{l,m}^{l',m'} \right] dH \\
& + \alpha_{j,n;l',m'} \int_{H_n^-}^{H_n^+} \left[A_{i,j} \mathbf{j}_{l,m}^{l',m'} \cdot \mathbf{n}_{i,j} + V_{i,j} \mathbf{F}_{i,j} \cdot \hat{\mathbf{F}}_{l,m}^{l',m'} \right] dH \\
& = \beta_{i,n \pm n';0,0} \frac{2V_{i,j}}{Y_{0,0}} \sum_{\eta} \int_{H_n^-}^{H_n^+} \sigma_{\eta}(\mathbf{x}, H \pm \hbar\omega_{\eta}, H) Z_{l,m} dH \\
& - \beta_{i,n;l,m} \frac{2V_{i,j}}{Y_{0,0}} \sum_{\eta} \int_{H_n^-}^{H_n^+} \sigma_{\eta}(\mathbf{x}, H, H \mp \hbar\omega_{\eta}) Z_{0,0}(H \mp \hbar\omega_{\eta}) dH .
\end{aligned} \tag{5.16}$$

The integrals over the coupling coefficients can again be further simplified as in (5.10) and (5.11).

5.4 Results

A comparison of the number of vertices required for a MOSFET and for a FinFET using structured and unstructured grids is given in the following. A comparison for a one-dimensional n^+nn^+ -diode is omitted since there the structured and unstructured meshes coincide.

The schematic MOSFET layout shown in Fig. 5.7 consists of 1 028 nodes. A much more aggressive coarsening could have been applied to the left and the right of the device, as well as deep inside the bulk of the device (bottom). Nevertheless, the structured grid shown at the right, which has the same grid spacing as the triangular mesh in the channel region, consists of 1 594 nodes, which consequently leads to about 50 percent more unknowns. Note that the high resolution inside the channel induces an increased solution deep in the substrate, because so-called *hanging nodes*¹ are prohibited for the box integration scheme. Therefore, a lower resolution, which would be typically sufficient deep in the substrate, cannot be obtained there. For demonstration purposes, only a coarse mesh has been chosen at the contacts. A finer grid at the contacts would result again in additional grid nodes in the bulk for the structured grid.

For a fully three-dimensional layout such as that of a FinFET, the difference in the number of grid points between structured and unstructured grids becomes much larger. Since the current flow is predominantly near the surface of the fin, a coarser mesh can be chosen in the center of the fin when using unstructured grids. At the transition from the source to the channel and particularly from the channel to the drain, a fine resolution is necessary in order to account for the high electric fields and the heated carriers in the latter case. The sample meshes of a FinFET depicted in Fig. 5.8 show that with only 4 838 nodes a fine mesh can be obtained in the channel and towards the drain region, while a structured grid with comparable resolution in the channel leads to 27 456 nodes, hence the difference is a factor of six. This difference mostly stems from the spurious high resolution of the structured grid in the source and drain regions.

¹A hanging node is a vertex that lies in the interior of an edge or face of another cell

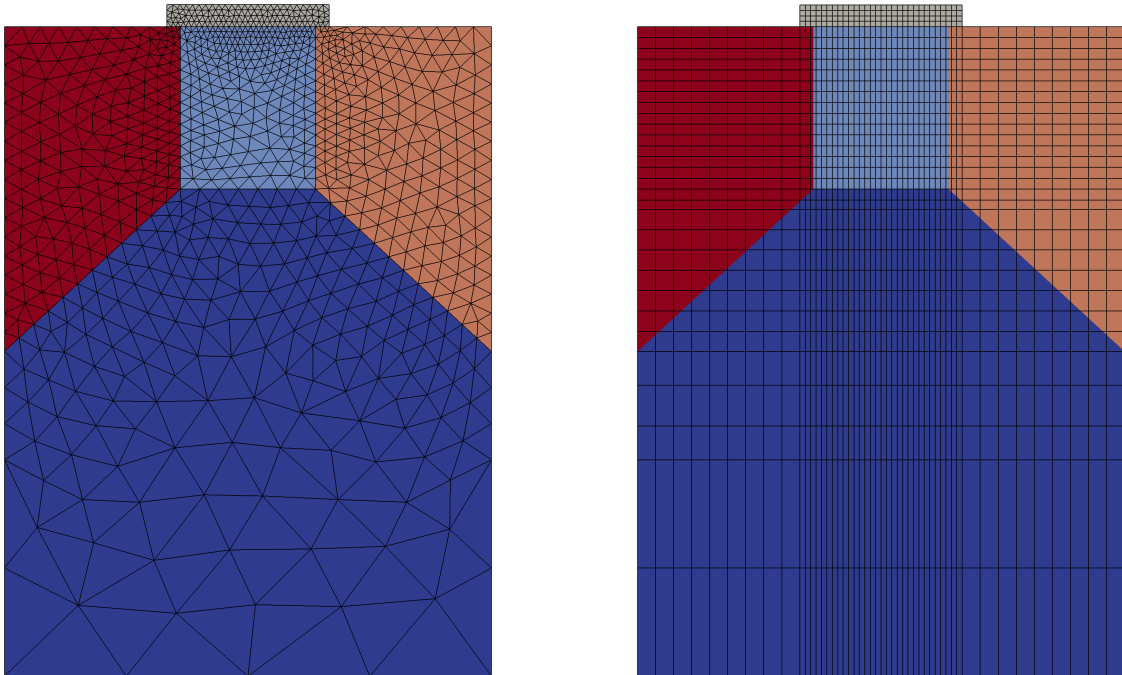


Figure 5.7: Comparison of a triangular mesh of a MOSFET and a structured grid with the same resolution inside the channel. While the triangular grid consists of 1 028 points, the structured grid leads to 1 594 grid points.

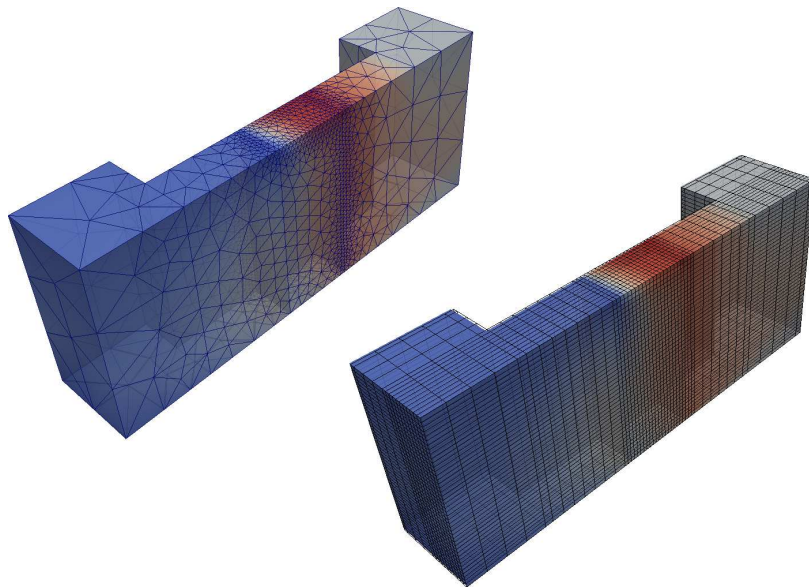


Figure 5.8: Comparison of the tetrahedral unstructured grid used for the simulation of half of a tri-gate transistor (no gate, oxide and body shown), and a structured grid with the same mesh size inside the channel. While the tetrahedral grid consists of 4 838 points, the structured grid is made up of 27 456 points, thus leading to considerably higher computational costs. For simplicity, only a course mesh has been chosen around the contacts.

Chapter 6

Adaptive Variable-Order SHE

The structural properties discussed in Chap. 4 show that in the case of spherical energy bands the coupling between the SHE equations is sparse. This allows for a reduction of memory requirements for the system matrix of the discretized equations from $\mathcal{O}(NL^4)$ to $\mathcal{O}(NL^2)$. The proposed matrix compression scheme further reduces the memory requirements for the system matrix to $\mathcal{O}(N + L^2)$, which finally results in the total memory requirements being dominated by the $N(L+1)^2 = \mathcal{O}(NL^2)$ unknowns already at an expansion order of five. For a three-dimensional device simulation using 100 discrete total energies and 10 000 grid points ($N = 10^6$), the number of unknowns for a first-order expansion are up to 4×10^6 , where 10^6 even-order expansion coefficients enter the linear solver. On the same grid, a ninth-order expansion leads to a total of 10^8 unknowns, of which 4.5×10^7 enter the linear solver. Even though the matrix compression scheme ensures that the total memory requirements stay within a reasonable amount of a few gigabytes, the high computational effort due to the large number of unknowns leads to long simulation times.

With the use of unstructured grids for the SHE method as described in Chap. 5, the number of grid points in the (\mathbf{x}, H) -space can be reduced to lower numbers than for structured grids without sacrificing accuracy in critical device regions. Therefore, the total number of unknowns in the linear system is reduced from $N(L+1)^2$ to $N'(L+1)^2$, where N and N' refer to the number of unknowns in (\mathbf{x}, H) -space and N' can be a factor two to five smaller than N , cf. Sec. 5.4.

Similar to unstructured grids, which allow for a high resolution in critical regions and a lower resolution in less important regions, a higher expansion order can be chosen at locations and energies with high influence on a target quantity such as current, carrier density, or average carrier velocity. Consequently, instead of a fixed-order expansion as in (2.41), variable-order expansions of the form

$$f(\mathbf{x}_i, \mathbf{k}(H_n, \theta, \varphi), t) = \sum_{l=0}^{L(\mathbf{x}_i, H_n)} \sum_{m=-l}^l f_{l,m}(\mathbf{x}_i, H_n, t) Y_{l,m}(\theta, \varphi) \quad (6.1)$$

are considered in this chapter. The aim is to further reduce the total number of unknowns to $N'(L'+1)^2$, where the average expansion order L' for a grid point \mathbf{x}_i obtained by averaging all positive expansion orders over all positive discrete kinetic energies can be well below an equivalent uniform expansion order L without sacrificing accuracy.

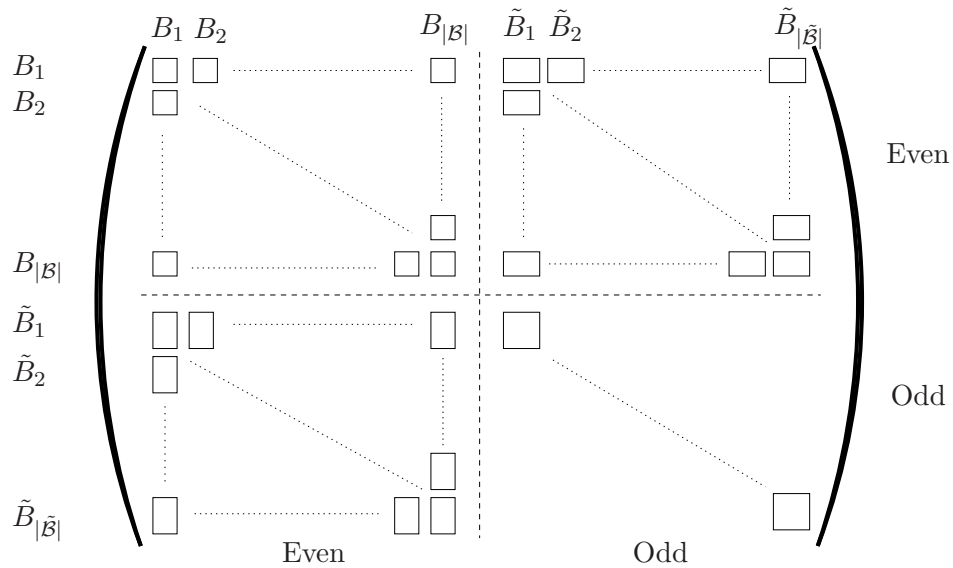


Figure 6.1: System matrix structure for uniform expansion orders with spherical energy bands at a constant energy. If two boxes B_i and B_j do not have a common interface, the respective blocks are zero. If boxes B_i and \tilde{B}_j do not overlap, the respective blocks are also zero. The odd-to-odd coupling implies a diagonal block due to the structure of the scattering operators.

6.1 Variable-Order SHE

The advantage of the SHE method is that the equilibrium distribution is described exactly by a zeroth-order expansion. This is in contrast to macroscopic transport models derived from moments of the BTE, where higher-order moments do not vanish. Therefore, it is reasonable to expect that for the resolution of small deviations from the equilibrium distribution, only a low expansion order is required for the SHE method in order to obtain good accuracy.

In this section the discretization of the SHE equations using variable-order expansions is presented. For a maximum expansion order L_{\max} in the simulation domain, a variable-order expansion can be obtained by assembling a system matrix for maximum expansion order L_{\max} and then imposing homogeneous Dirichlet conditions on all expansion coefficients $f_{l,m}(\mathbf{x}_i, H_n)$ with $l > L(\mathbf{x}_i, H_n)$. However, such an approach is impractical due to the unnecessary effort of setting up a much larger system matrix than actually required. In addition, the benefit of reduced memory required for variable expansion orders is eliminated when setting up a system matrix for uniform expansion order L_{\max} first.

It is assumed that the unknowns are enumerated in such a way that the expansion coefficients for a particular box $B \in \mathcal{B}$ or a dual box $\tilde{B} \in \tilde{\mathcal{B}}$ are consecutive. In addition, the unknowns associated with boxes $B \in \mathcal{B}$ are enumerated first, then the unknowns associated with the dual boxes $\tilde{B} \in \tilde{\mathcal{B}}$, which leads to the system matrix structure discussed in Sec. 4.3. The resulting structure of the system matrix for a uniform expansion order is depicted in Fig. 6.1. The block sizes for each block coupling two boxes are:

	Even	Odd
Even	$N_L^{\text{even}} \times N_L^{\text{even}}$	$N_L^{\text{even}} \times N_L^{\text{odd}}$
Odd	$N_L^{\text{odd}} \times N_L^{\text{even}}$	$N_L^{\text{odd}} \times N_L^{\text{odd}}$

Here, N_L^{even} and N_L^{odd} denote the number of even and odd expansion coefficients up to and including order L respectively. For instance, consider the block in the rows for box B_i and in the columns for the dual box \tilde{B}_i , which is located at the interface between B_i and B_j . From the discrete equations for the even-order projections in steady-state (5.9) one obtains the system matrix block for a certain discrete energy H_n directly from rewriting the discrete equations in matrix form:

$$\left[\begin{array}{c} \sum_{d=1}^3 A_{i,j} n_{i,j;d} \\ \\ - \sum_{d=1}^3 V_{i,j} F_{i,j;d} \end{array} \left(\begin{array}{ccc} \int_{H_n^-}^{H_n^+} j_{0,0;d}^{1,-1} dH & \cdots & \int_{H_n^-}^{H_n^+} j_{0,0;d}^{L,L} dH \\ \int_{H_n^-}^{H_n^+} j_{2,-2;d}^{1,-1} dH & \cdots & \int_{H_n^-}^{H_n^+} j_{2,-2;d}^{L,L} dH \\ \vdots & \ddots & \vdots \\ \int_{H_n^-}^{H_n^+} j_{L-1,L-1;d}^{1,-1} dH & \cdots & \int_{H_n^-}^{H_n^+} j_{L-1,L-1;d}^{L,L} dH \end{array} \right) \right] \left(\begin{array}{c} \beta_{i,n;1,-1} \\ \vdots \\ \beta_{i,n;L,L-2} \\ \beta_{i,n;L,L} \end{array} \right), \quad (6.2)$$

where the subscript index d denotes the d -th component of the vector and the expansion order L is odd. The matrix block (B_i, B_i) results from the scattering operator and is diagonal up to couplings induced by energy displacements $\hbar\omega_\eta$ due to inelastic scattering mechanisms, cf. Thm. 3. A similar structure is obtained for the even-to-even, the odd-to-even, and the odd-to-odd block.

When allowing variable-order expansions, the dimensions of the coupling blocks can differ for each box B_i and each dual box \tilde{B}_i . Reconsidering the example of the matrix block for the box B_i and the dual box \tilde{B}_i from above, and assuming an even expansion order L_i for B_i and an odd expansion order \tilde{L}_i for the dual box \tilde{B}_i , the discrete system of equations is given by

$$\left[\begin{array}{c} \sum_{d=1}^3 A_{i,j} n_{i,j;d} \\ \\ - \sum_{d=1}^3 V_{i,j} F_{i,j} n_{i,j;d} \end{array} \left(\begin{array}{ccc} \int_{H_n^-}^{H_n^+} j_{0,0;d}^{1,-1} dH & \cdots & \int_{H_n^-}^{H_n^+} j_{0,0;d}^{\tilde{L}_i, \tilde{L}_i} dH \\ \int_{H_n^-}^{H_n^+} j_{2,-2;d}^{1,-1} dH & \cdots & \int_{H_n^-}^{H_n^+} j_{2,-2;d}^{\tilde{L}_i, \tilde{L}_i} dH \\ \vdots & \ddots & \vdots \\ \int_{H_n^-}^{H_n^+} j_{L_i-1, L_i-1;d}^{1,-1} dH & \cdots & \int_{H_n^-}^{H_n^+} j_{L_i-1, L_i-1;d}^{\tilde{L}_i, \tilde{L}_i} dH \end{array} \right) \right] \left(\begin{array}{c} \beta_{i,n;1,-1} \\ \vdots \\ \beta_{i,n;\tilde{L}_i, \tilde{L}_i-2} \\ \beta_{i,n;\tilde{L}_i, \tilde{L}_i} \end{array} \right). \quad (6.3)$$

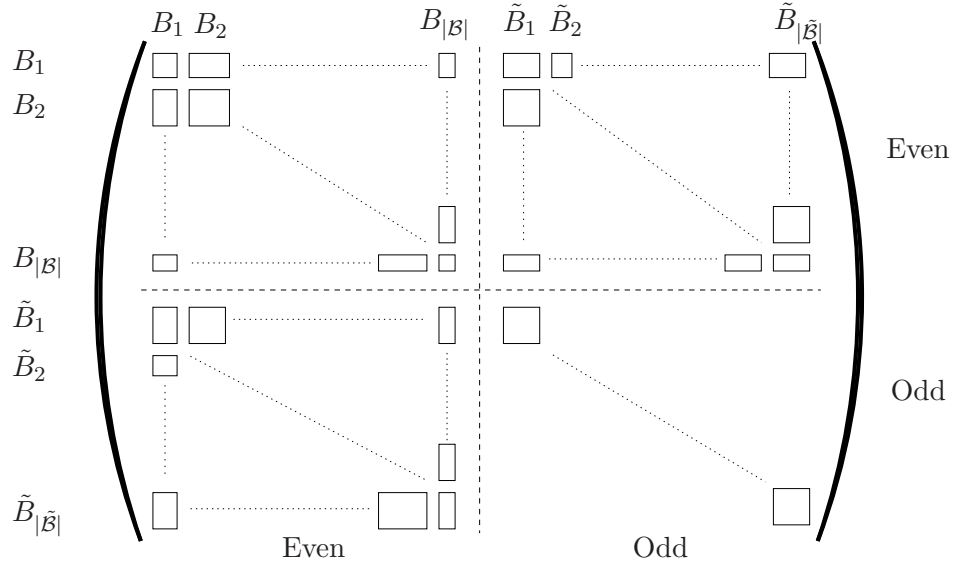


Figure 6.2: System matrix structure for variable-order expansions with spherical energy bands at a constant energy. The coupling blocks have varying sizes.

This leads to the system matrix structure shown in Fig. 6.2, where the individual small blocks are now of different dimension according to the respective expansion order.

The expansion orders for the boxes B_i and the dual boxes \tilde{B}_i should not be chosen arbitrarily. Consider the case of spherical energy bands, where only a single box B carries the maximum even expansion order L_{\max} . If all surrounding dual boxes carry an odd expansion order of at most $L_{\max} - 3$, then the highest-order expansion coefficients $f_{L_{\max},m}$ for the box B do not couple due to Thm. 2 with expansion coefficients of lower order. Since the right hand side of the linear equation is zero except for Dirichlet boundary values, the expansion coefficients $f_{L_{\max},m}$ are computed as zero. Moreover, since the size of the final linear system of equations is determined by the expansion orders of the boxes $B_i \in \mathcal{B}$ only, Thm. 2 suggests that the odd expansion order of the dual box \tilde{B} should be larger than the even expansion orders of the two overlapped boxes B_i and B_j , otherwise the linear system of equations yields a less accurate solution at the same computational effort. Summing up, one obtains:

Guideline 1. *The odd expansion order of each of each dual box $\tilde{B} \in \tilde{\mathcal{B}}$ should be larger than the even expansion orders of the boxes B_i and B_j overlapped by \tilde{B} .*

Conversely, since odd expansion orders larger than required do not lead to higher accuracy because of the same reasoning with the roles of B_i and \tilde{B}_i exchanged, the odd expansion order of a dual box is set to the maximum even expansion order of the overlapped boxes plus one, i.e.

$$\text{order}(\tilde{B}_{i,j}) = \max(\text{order}(B_i), \text{order}(B_j)) + 1. \quad (6.4)$$

Consider two neighboring boxes B_i and B_j with expansion orders L_i and L_j , $L_i < L_j$. Denote the dual box overlapping B_i and B_j with $\tilde{B}_{i,j}$. From Thm. 2 and Guideline 2 it follows that the expansion coefficients defined for B_i couple with expansion coefficients in $\tilde{B}_{i,j}$ up to order $L_i + 1$. These expansion coefficients in $\tilde{B}_{i,j}$ couple according to Thm. 2

with expansion coefficients in B_j up to order $L_i + 2$, thus there is no gain in accuracy for L_j larger than $L_i + 2$. This leads to the second guideline:

Guideline 2. *The maximum even expansion order of neighboring boxes B_i and B_j should not differ by more than two.*

6.2 Adaptive Control of the SHE Order

In the previous section the efficient assembly of SHE equations using variable expansion orders has been discussed. However, the variable expansion orders were assumed to be given for each box B and each dual box \tilde{B} . For every-day TCAD purposes, such a selection should be based on an adaptive strategy until a prescribed accuracy for a certain target quantity is reached. This section thus discusses strategies to automatically pick suitable expansion orders within the simulation domain. Due to Guideline 1, it suffices to select expansion orders for the the boxes in \mathcal{B} .

What is considered to be a *suitable* or *good* expansion order for a box B clearly depends on the target quantity. Macroscopic quantities are typically obtained by moments of the distribution function such as

$$X(\mathbf{x}, t) = \int_{\mathbb{R}^3} \Phi(\mathbf{k}) f(\mathbf{x}, \mathbf{k}, t) d\mathbf{k}^3, \quad (6.5)$$

where $\Phi(\mathbf{k})$ is a suitable polynomial of \mathbf{k} . Due to the asymptotically exponential decay of the distribution function f with the modulus of \mathbf{k} , the distribution function needs to be computed with high accuracy at low energies, while lower accuracy is sufficient at higher energies for the computation of X . However, for the investigation of high-energy phenomena such as hot carrier degradation [9,101], the distribution function needs to be fairly accurate at high energies, while there is less emphasis on accuracy at lower energies. Consequently, *suitable* expansion orders depend on the quantities of interest.

In the following, three different strategies for the adaptive choice of expansion orders are presented. The first approach is based on an analytical result for the SHE of a function $g(\theta, \varphi)$ in dependence of the smoothness of g . The second approach increases the expansion order particularly in regions with high weight on one or more target quantities. The third approach is a rather classical residual-based technique, which is common in finite element and finite volume methods [1,8,56]. Even though the three strategies are presented separately, in practice they should be combined in order to obtain best results.

6.2.1 Rate of Decay of Expansion Coefficients

The SHE can be seen as the three-dimensional extension of Fourier series. Since the latter is more widely known than the former, the motivation for the adaptive strategy for SHE is first given for Fourier series. The transition from Fourier series to SHE does not impose additional complications then.

A 2π -periodic function $f(\varphi)$ can be expanded into trigonometric functions as

$$f(\varphi) = \sum_{m=0}^{\infty} a_m \cos(m\varphi) + b_m \sin(m\varphi), \quad (6.6)$$

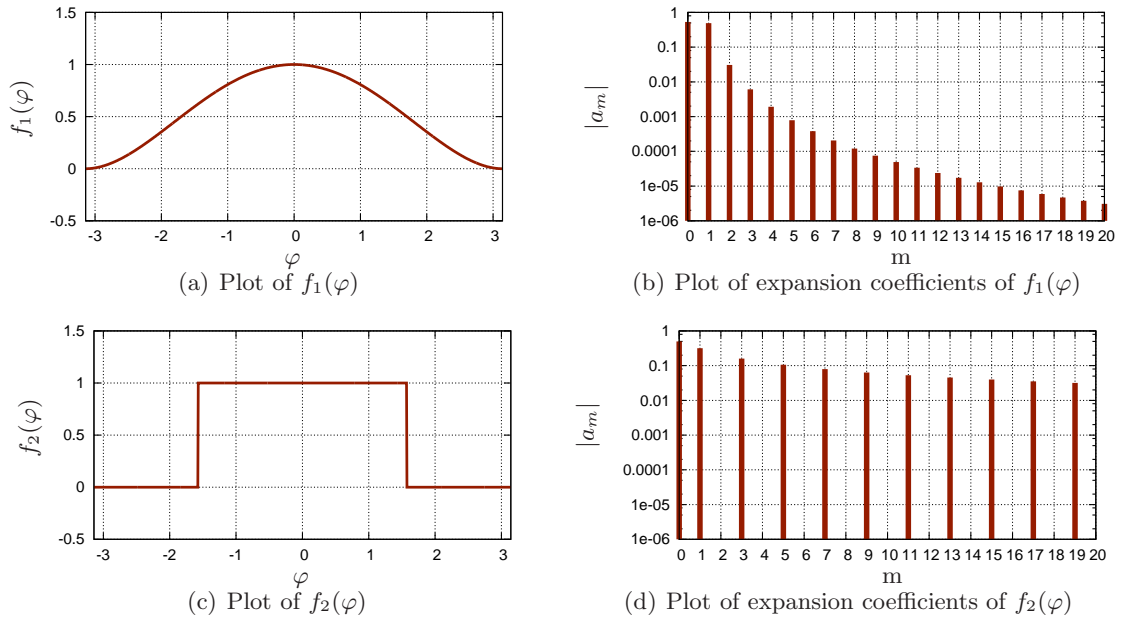


Figure 6.3: Comparison of the Fourier series of a differentiable function f_1 and a discontinuous function f_2 .

where $b_0 = 0$. The function f does not need to be continuous, it is sufficient for f to be integrable. The expansion coefficients are computed from f as

$$a_0 = \frac{1}{2\pi} \int_{-\pi}^{\pi} f(\varphi) d\varphi, \quad (6.7)$$

$$a_m = \frac{1}{\pi} \int_{-\pi}^{\pi} f(\varphi) \cos(m\varphi) d\varphi, \quad (6.8)$$

$$b_m = \frac{1}{\pi} \int_{-\pi}^{\pi} f(\varphi) \sin(m\varphi) d\varphi. \quad (6.9)$$

Consider the two 2π -periodic functions depicted in Fig. 6.3

$$f_1(\varphi) = [(x - \pi)(x + \pi)]^2/\pi^4 = x^4/\pi^4 - 2x^2/\pi^2 + 1, \quad f_2(\varphi) = \begin{cases} 1, & |\varphi| \leq \pi/2, \\ 0, & \pi/2 < |\varphi| \leq \pi. \end{cases} \quad (6.10)$$

While f_1 is continuously differentiable, f_2 is discontinuous. The Fourier series of the functions are given by

$$f_1(\varphi) = \frac{8}{15} - 48 \sum_{m=1}^{\infty} \frac{(-1)^m}{\pi^4 m^4} \cos(m\varphi), \quad f_2(\varphi) = \frac{1}{2} - \sum_{m=1}^{\infty} \frac{2(-1)^m}{\pi(2m-1)} \cos((2m-1)\varphi). \quad (6.11)$$

For the smooth function f_1 , the Fourier coefficients decay with the fourth power of m , while the Fourier coefficients of f_2 only decay inversely proportional to m . More generally, it can be shown that for a function with integrable derivatives up to order k , the expansion

coefficients decay at least with rate m^{-k} . Conversely, the rate of decay of the Fourier coefficients are a measure for the smoothness of the expanded function [13, 28].

For SHE, a similar result holds for a function f defined on the unit sphere Ω [18, 31]:

Theorem 4. *Let f be k -times continuously differentiable on the unit sphere Ω , where k is a nonnegative integer. For the spherical harmonics expansion*

$$f = \sum_{l=0}^{\infty} \sum_{m=-l}^l f_{l,m} Y^{l,m} =: \sum_{l=0}^{\infty} Q_l, \quad (6.12)$$

where Q_l is a spherical harmonic of degree l , there holds

$$|Q_l(\theta, \varphi)| \leq C l^{1/2-k}, \quad (6.13)$$

for a constant $C = C(f) > 0$ independent of k and all angles θ and φ .

Since the spherically symmetric distribution function f in equilibrium is described exactly by a zeroth-order expansion, higher-order expansion coefficients provide a measure for the distortion of f from equilibrium. This is in contrast to macroscopic models derived from moments of the BTE such as those described in Sec. 1.1, where even moments of the distribution function in equilibrium do not vanish.

Given a numerical solution of the SHE equations for certain expansion orders $L(\mathbf{x}_i, H_i)$, an adaptive adjustment of the expansion order can be based on (6.13). Division by $f_{0,0} \approx C$ and taking the logarithm leads for $l > 2$ to

$$\log |Q_l| - \log f_{0,0} \lesssim (1/2 - k) \log l, \quad (6.14)$$

where here and in the following $\log |Q_l|$ refers to $\max_{\theta, \varphi} \log |Q_l(\theta, \varphi)|$. Taking the left hand side as an estimate for k and dropping the constant $1/2$, which acts only as an offset to the estimate on the rate of decay k , results in

$$\eta := -k \sim \frac{\log |Q_l| - \log f_{0,0}}{\log l}, \quad (6.15)$$

with η taking the role of an error estimator. The larger the value of η at a certain point (\mathbf{x}_i, H_n) , the slower is the decay of the distribution function, thus the higher is the expected gain in accuracy from an increased expansion order.

Since due to Guideline 1 the highest available expansion order is associated with dual boxes in $\tilde{\mathcal{B}}$, the rate of decay for a box B_i can be based either on the highest expansion order for the box B_i , or on the dual boxes $\tilde{B}_{i,j}$ overlapping B_i . In the latter case, one obtains for the error estimator η_i for the box B_i

$$\eta_i \sim \left[\frac{\sum_{\tilde{B}_{i,j}} \log |Q_{l+1}|}{\tilde{N}_i} - \log f_{0,0} \right] / \log(l+1), \quad (6.16)$$

where the maximum expansion order in B_i is l , the sum extends over the dual boxes overlapping B_i and \tilde{N}_i denotes the number of dual boxes overlapping B_i .

The exact evaluation of the term $\log |Q_l| = \max_{\theta, \varphi} \log |Q_l(\theta, \varphi)|$ is a maximization problem over all angles and leads to high overall numerical effort, because such a maximization problem needs to be solved at every grid point (\mathbf{x}_i, H_n) . A numerically very cheap approximation to the maximum is

$$|Q_{l+1}| \approx \sum_{m=-l-1}^{l+1} |f_{l+1,m}| |Y_{l,m}| \approx \sum_{m=-l-1}^{l+1} |f_{l+1,m}|, \quad (6.17)$$

since the expansion coefficients $f_{l,m}$ are readily available. The approximation $|Y_{l,m}| \approx 1$ leads to an overestimation of the maximum, but is not a concern because it leads to a constant offset in the error indicator η_i only.

The case $l = 0$ in (6.16) requires additional treatment since $\log(l+1)$ evaluates to zero. Replacing l by $l+1$ resolves these problems and partly accounts for the overestimation of $|Q_{l+1}|$ by (6.17). For larger values of l , the replacement of l by $l+1$ does not cause a significant difference anyway. This leads to the final form of the estimator:

$$\eta_i \sim \left[\frac{\sum_{\tilde{B}_{i,j}} \log \left[\sum_{m=-L_i-1}^{L_i+1} |f_{L_i+1,m}(\tilde{B}_{i,j})| \right]}{\tilde{N}_i} - \log |f_{0,0}| \right] / \log(L_i + 2), \quad (6.18)$$

where L_i denotes the maximum even expansion order of the box B_i . After an evaluation of the estimator for all boxes B_i , the expansion order can then be increased for the boxes with largest values of η_i . An additional smoothing step then ensures conformity with respect to Guidelines 1 and 2.

The estimator (6.18) is based on the rate of decay of the expansion coefficients only and does not consider the exponential decay of the distribution function at higher energies. Therefore, the estimator treats regions with large values of the distribution function as being equally important as regions with very low values of the distribution function. This is a disadvantage if the target quantity is a macroscopic quantity such as the average carrier velocity, for which only large values of the distribution function lead to significant contributions. In such situations, an additional term $\alpha \log f_{0,0}$ may be added to (6.18) in order to penalize low-probability regions of the distribution function. In the special case $\alpha = 1/\log(L_i + 2)$, this modification is equivalent to dropping the term $\log f_{0,0}$ from (6.18). It should be noted that this modification towards higher weight at regions with high probability is similar in spirit to a target quantity driven control of the expansion order discussed next.

6.2.2 Target Quantity Driven Adaptive Control

Another approach to the adaptive control of the expansion order is based on one or more dedicated target quantities, for which the expansion orders are chosen such that a prescribed accuracy is obtained. For instance, consider as target quantity the average particle energy

$$\langle \varepsilon \rangle(\mathbf{x}) = \int_0^\infty \varepsilon f(\mathbf{x}, \varepsilon) Z(\varepsilon) d\varepsilon. \quad (6.19)$$

The average energy of a discrete solution $f(\mathbf{x}_i, H_n)$ of the SHE equations is computed using e.g. a simple midpoint quadrature rule as

$$\langle \varepsilon \rangle(\mathbf{x}_i) \approx \sum_{n=0}^{N_H} \varepsilon(H_n) f_{0,0}(\mathbf{x}_i, H_n) Z(H_n) (H_n^+ - H_n^-). \quad (6.20)$$

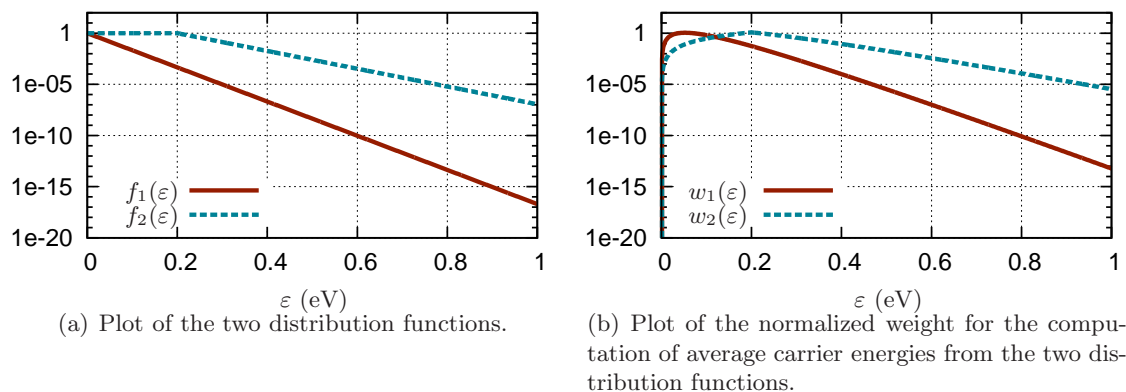


Figure 6.4: Comparison of weights for the computation of average energies for a Maxwellian distribution f_1 and a shifted, heated Maxwellian f_2 . The two weights are normalized to a peak value 1.

Hence, this allows for an extraction of the individual weight $w(\mathbf{x}_i, H_n)$ of the grid node (\mathbf{x}_i, H_n) on the target quantity as

$$w(\mathbf{x}_i, H_n) = \frac{\varepsilon(H_n) f_{0,0}(\mathbf{x}_i, H_n) Z(H_n) (H_n^+ - H_n^-)}{\langle \varepsilon \rangle(\mathbf{x}_i)}. \quad (6.21)$$

Weights for other target quantities such as the average carrier velocity or the carrier density can be defined in a similar manner. Therefore, $w(\mathbf{x}_i, H_n)$ can be seen as a generic weight function for an arbitrary target quantity $q(\mathbf{x}, H)$, where typically macroscopic target quantities of the form $q(\mathbf{x})$ are of interest.

An increase of the expansion order is most appropriate in regions where the weights w are high. On the contrary, regions with a weight of several orders of magnitude below the boxes of highest weight can be kept at lowest expansion order, because the contribution to the target quantity is very small anyway.

A comparison of the weight functions for the calculation of the average carrier energy of a Maxwellian distribution f_1 and a shifted and heated Maxwellian distribution f_2 is depicted in Fig. 6.4. For the Maxwellian distribution it is sufficient to consider only energies up to about 0.3 eV for the computation of the average energy at an accuracy of about one percent, because the weights at higher energies are below 10^{-3} already. However, for the shifted and heated Maxwellian distribution, contributions up to an energy of about 0.6 eV need to be considered for comparable accuracy.

6.2.3 Residual-Based Adaptive Control

An expansion order control based solely on the weight function w does not account appropriately for long-range influences of regions of the distribution function with low probability on regions with higher probability. This is a particular concern in short devices at high electric fields, where strong variations of the distribution function with respect to energy are observed. Similar to the estimation of the rate of decay in Sec. 6.2.1, a residual-based approach provides a better monitor for the need for higher expansion orders than the target quantity driven approach in the previous section.

Let $\mathbf{f}^L = (f_{l,m}^L(\mathbf{x}_i, H_n))_{l,m;i,n}$ denote the numerical solution of the SHE equations for a possibly variable expansion order $L = L(\mathbf{x}_i, H_n)$ obtained from the solution of the system

$$\mathbf{S}^L \mathbf{f}^L = \mathbf{b}^L . \quad (6.22)$$

Now, let $\mathbf{f}^{L \leftrightarrow L'} = (f_{l,m}^{L \leftrightarrow L'}(\mathbf{x}_i, H_n))_{l,m;i,n}$ denote the prolonged solution \mathbf{f}^L for a possibly variable expansion order $L' = L'(\mathbf{x}_i, H_n) > L(\mathbf{x}_i, H_n)$ obtained by

$$f_{l,m}^{L \leftrightarrow L'}(\mathbf{x}_i, H_n) = \begin{cases} f_{l,m}^L(\mathbf{x}_i, H_n) , & l \leq L(\mathbf{x}_i, H_n) \\ 0 , & \text{otherwise} . \end{cases} \quad (6.23)$$

Denoting the system matrix for the expansion orders L' with $\mathbf{S}^{L'}$ and the right hand side with $\mathbf{b}^{L'}$, the residual

$$\mathbf{e}^{L \leftrightarrow L'} := \mathbf{S}^{L'} \mathbf{f}^{L \leftrightarrow L'} - \mathbf{b}^{L'} \quad (6.24)$$

provides an indication on where to increase the expansion order. In order to make the residual invariant with respect to the scale of the values $f_{l,m}^L(\mathbf{x}_i, H_n)$, the linear system should be first symmetrized and rescaled as discussed in Sec. 7.2. Note that the matrix compression scheme derived and discussed in Chap. 4 allows for a convenient means to store the larger system matrix \mathbf{S}' and to compute the matrix-vector product $\mathbf{S}^{L'} \mathbf{f}^{L \leftrightarrow L'}$ efficiently.

It is important to keep in mind that the residual is not invariant with respect to transformations of the linear system. In particular, if the j -th equation is multiplied with a certain factor, then also the residual is multiplied with the same factor, even though the solution of the linear system is unchanged. Consequently, it is advisable to first apply normalizations, for instance by multiplication of each equation in the system with the reciprocal of the respective diagonal entry.

Similar to other expansion order control strategies outlined above, an increase of the expansion order can finally be carried out for boxes with highest residuals. An additional expansion order smoothing step after the increase ensures that Guidelines 1 and 2 are obeyed.

6.3 Results

Average carrier velocities along a 100 nm n^+nn^+ -diode with a bias of 0.7 Volt and intrinsic region between $x = 20$ nm and $x = 60$ nm are compared for different uniform expansion orders as well as for the three adaptive expansion order schemes after one (maximum SHE order 3), two (maximum SHE order 5) and three (maximum SHE order 7) adaption steps. The total energy range spans 2 eV using an energy spacing of 12.5 meV. A first-order expansion is kept directly at the band edge, because it has been observed that it improves numerical stability at high expansion orders. At the contacts, a Maxwell distribution is imposed as a Dirichlet boundary condition, thus the expansion is kept at first order there. The resulting velocity curves are depicted in Fig. 6.5 and show rather small differences between the different expansion orders. Nevertheless, the logarithmic plots of the relative errors in Fig. 6.9 provide full insight.

The adaptive strategy based on the decay of expansion coefficients as described in Sec. 6.2.1 is illustrated in Fig. 6.6. In order to emphasize refinement in high-probability

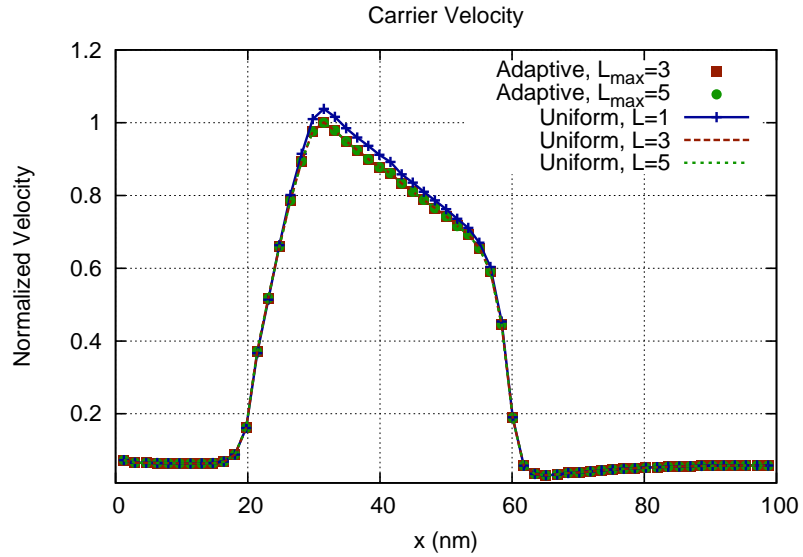


Figure 6.5: Comparison of carrier velocities for different uniform and adaptive SHE orders. The differences between the adaptive schemes are below the image resolution and analyzed in more detail in Fig. 6.9.

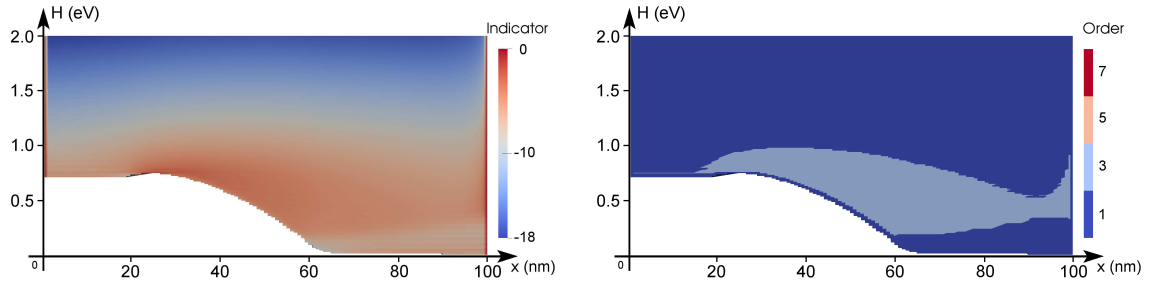
regions, the term $0.25 \times \log(f_{0,0})$ is added to (6.18) as discussed above. The resulting indicator values are shifted such that the highest value is zero. The threshold for an expansion order increase is set to -6.0 . The indicator is not computed at the contact, but evaluated to 0 in Fig. 6.6. During the adaption procedure, the adaptive control stays at a first-order expansion in the left n^+ region, where the distribution function is still close to equilibrium. The expansion order is then increased in the intrinsic region and away from the band edge at higher energies after the intrinsic regions. In summary, the adaptive strategy based on the decay of the expansion coefficients increases the expansion order mostly along the high energy tail and close to the band edge inside the intrinsic region. The increase of the expansion order near the right contact stems from the use of Dirichlet boundary conditions and can be considered to be an artifact, because the distribution function is forced from a heated distribution to a Maxwell distribution at the contact, leading to an unphysical boundary layer as discussed by Schroeder *et al.* [92].

A different behavior is observed for the target quantity based control shown in Fig. 6.7. The indicator is obtained by taking the logarithm of the contribution of the respective box in the simulation domain and shifting the values such that the highest contribution leads to an indicator value of zero. A threshold value of -2.0 has been used for increasing the expansion order. Since the distribution function changes its shape only mildly at higher energies, the indicator is essentially unchanged during the adaption, leading to higher expansion orders near the band edge only. Note that the high-energy tail of the distribution function right after the intrinsic region is resolved by the increased expansion order. The error plot in Fig. 6.9(b) shows that virtually the same accuracy as for uniform expansions is obtained. However, the expansion order at later adaption steps abruptly changes from first-order to highest order as quickly as possible without violating Guidelines 1 and 2, thus it is reasonable to expect that a less abrupt change of the expansion order can preserve the accuracy using a lower number of unknowns.

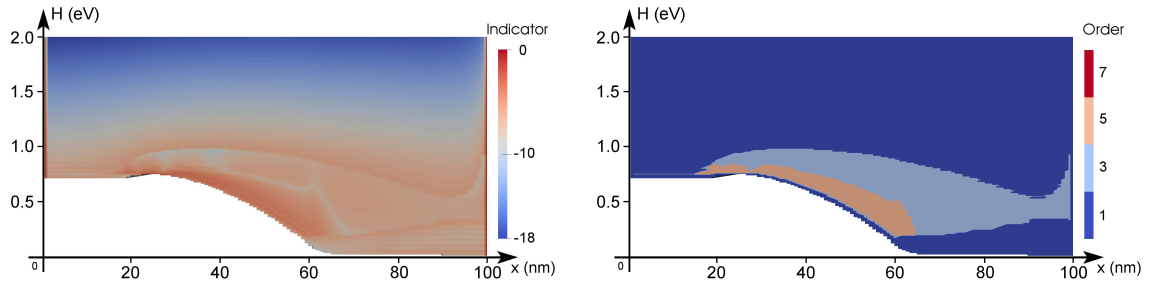
Fig. 6.8 depicts the effect of the residual based expansion order control. The residual has been normalized first by scaling the uniform system such that a unit diagonal is obtained. The indicator is then obtained by taking the logarithm of the residual values and applying a suitable shift such that the highest residual value leads to an indicator value of zero. The expansion order is increased if the indicator is larger than -2.0 . In principle, one may assign less weight to higher energies such as for the adaptive strategy based on the rate of decay of expansion coefficients. For illustration purposes, the unmodified indicator is shown. It should be noted that the strategy based on the decay leads to qualitatively similar indicator values if no modification at higher energies is applied. The pure residual based strategy increases the expansion order to third-order up to high energies in the right half of the device. However, fifth-order expansions are used in a very small region in the device only. A seventh-order expansion is only assigned right above the band edge inside the intrinsic region. The error plot in Fig. 6.9(c) is very similar to the error plot for the strategy based on the decay of expansion coefficients, hence the same conclusions can be drawn.

Fig. 6.9 further shows that the SHE method converges to a solution as the expansion order increases. As reference, a uniform seventh-order expansion is used. A first-order expansion shows an average error of about 10^{-2} over the device with respect to the seventh-order expansion taken as reference. The average error of a third-order expansion is around $10^{-3.5}$, and approximately 10^{-5} for a fifth-order expansion. A similar exponential decay of the error with the SHE order has also been observed by Jungemann *et al.* [53] for the collector current of a bipolar junction transistor, even though at a lower rate.

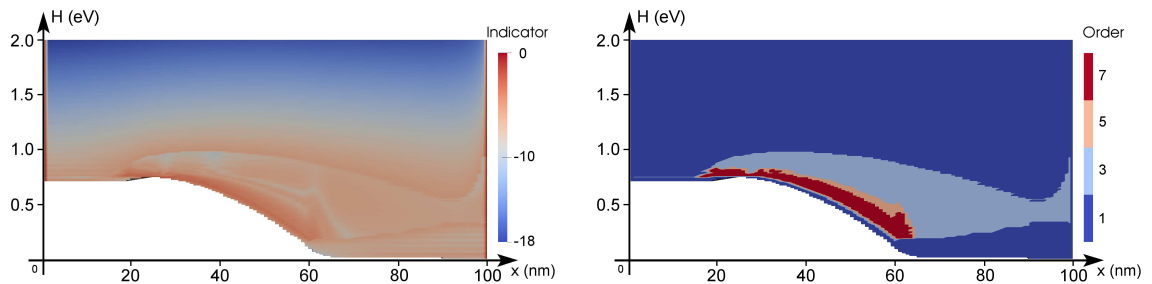
The number of unknowns obtained with uniform and three adaptive expansions are depicted in Fig. 6.10. Savings of a factor of almost three are obtained with the target quantity based scheme, which yields virtually the same accuracy as uniform expansions. Memory requirements and execution times are consequently reduced by the same factor. Typically, higher savings for the execution times are obtained in practice, because linear solvers with optimal complexity are not available in general. A combination of the three different schemes proposed may give slightly higher savings, which become significant at very high expansion orders only.



(a) Indicator for the first adaptation step (left). Expansion order after the first adaptation step (right).

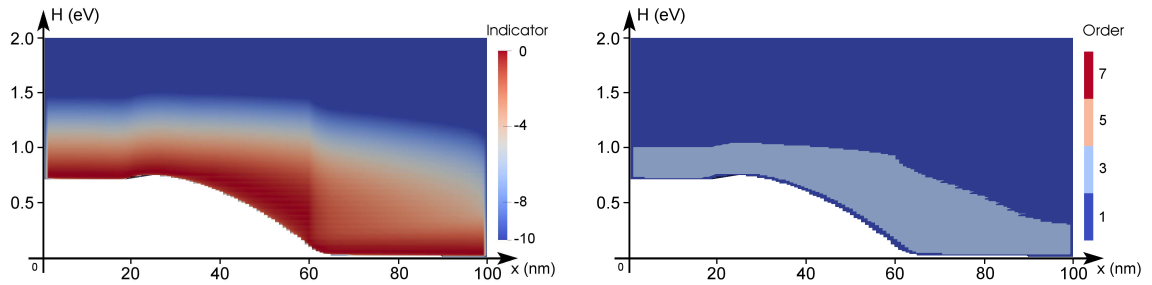


(b) Indicator for the second adaptation step (left). Expansion order after the second adaptation step (right).

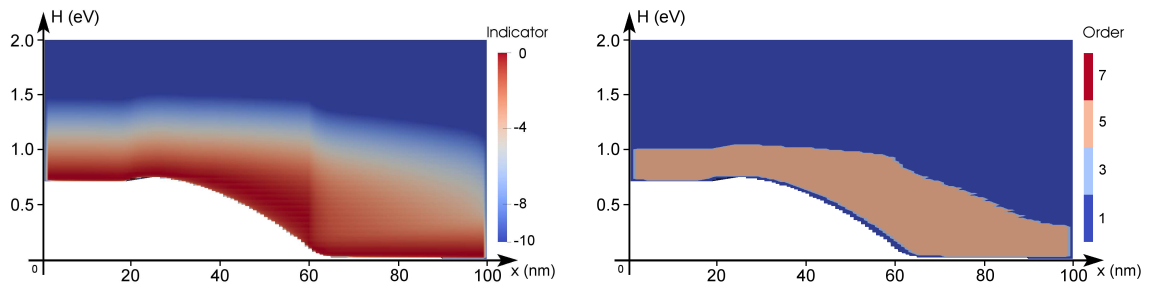


(c) Indicator for the third adaptation step (left). Expansion order after the third adaptation step (right).

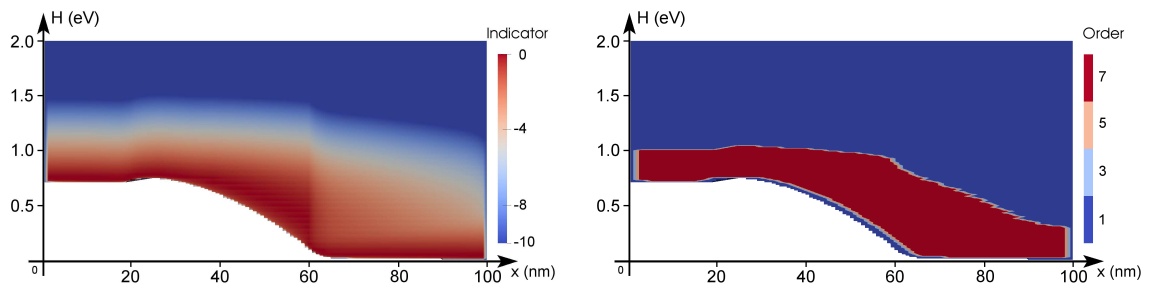
Figure 6.6: Expansion indicator and expansion orders in the n^+nn^+ diode for three adaptation steps using an adaptive scheme based on the decay of expansion coefficients as outlined in Sec. 6.2.1. The scheme starts with a uniform first-order expansion. The error indicator is not computed on the left and right contact and thus plotted with an arbitrary value of 0.



(a) Indicator for the first adaptation step (left). Expansion order after the first adaption step (right).

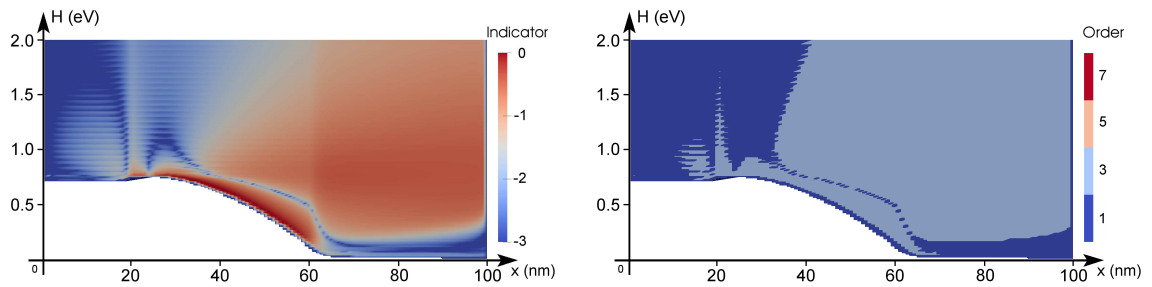


(b) Indicator for the second adaptation step (left). Expansion order after the second adaption step (right).

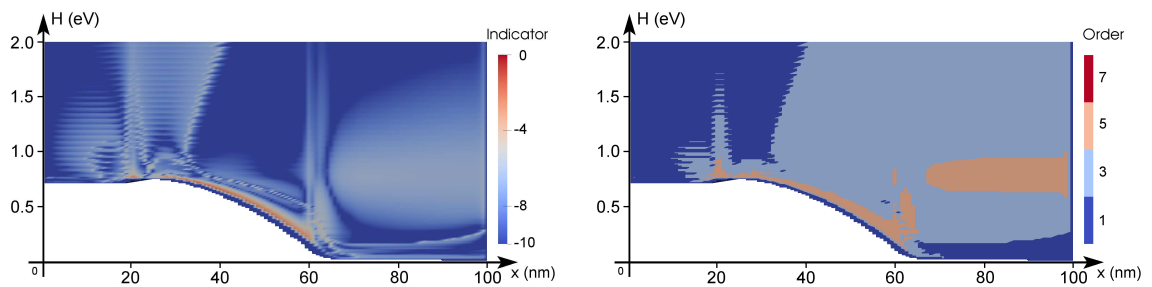


(c) Indicator for the third adaptation step (left). Expansion order after the third adaption step (right).

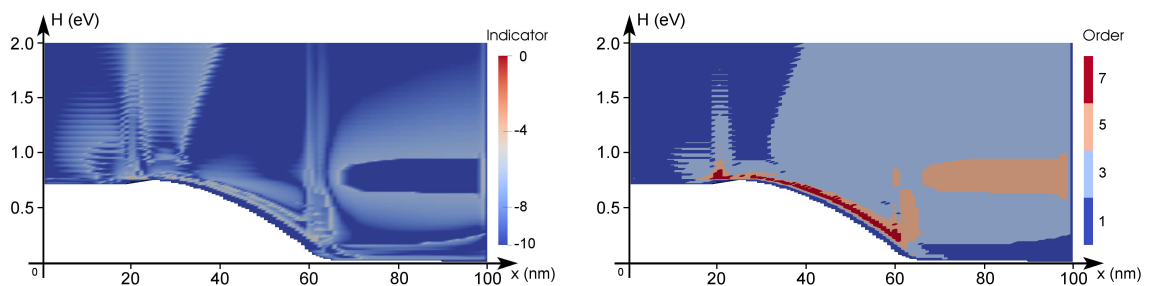
Figure 6.7: Expansion indicator and expansion orders in the n^+nn^+ diode for three adaptation steps using an adaptive scheme based on a target quantity as discussed in Sec. 6.2.2. The scheme starts with a uniform first-order expansion.



(a) Indicator for the first adaptation step (left). Expansion order after the first adaptation step (right).

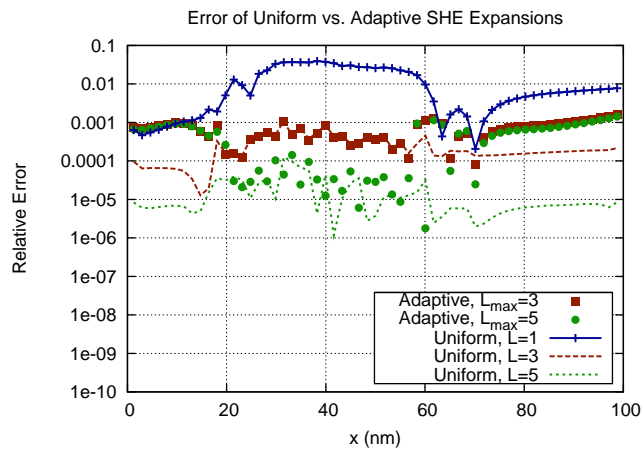


(b) Indicator for the second adaptation step (left). Expansion order after the second adaptation step (right).

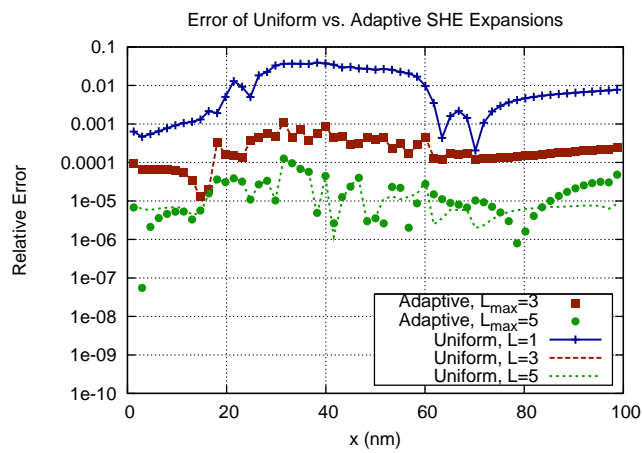


(c) Indicator for the third adaptation step (left). Expansion order after the third adaptation step (right).

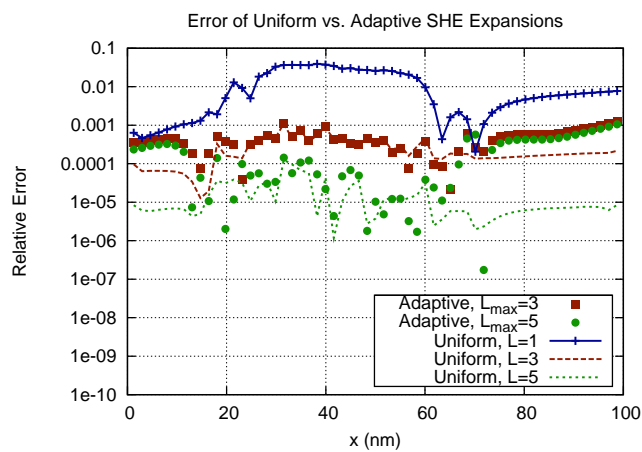
Figure 6.8: Expansion indicator and expansion orders in the n^+nn^+ diode for three adaptation steps using an adaptive scheme based on residuals as described in Sec. 6.2.3. The scheme starts with a uniform first-order expansion.



(a) Rate of decay based scheme.



(b) Target quantity based scheme.



(c) Residual based scheme.

Figure 6.9: Comparison of the relative errors in carrier velocities for different uniform and adaptive SHE orders using different adaptive schemes. A uniform seventh-order expansion is used as reference.

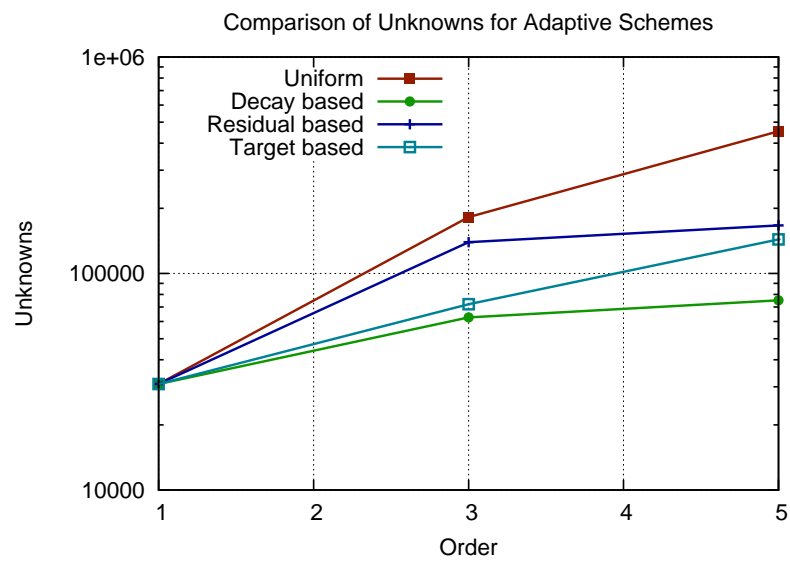


Figure 6.10: Comparison of the number of unknowns for the three different adaptive expansion order control schemes.

Chapter 7

Parallelization

The paradigm shift from single- to multi- and many-core computing architectures places additional emphasis on the development of parallel algorithms. In particular, the use of graphics processing units (GPUs) for general purpose computations poses a considerable challenge due to the high number of threads executed in parallel. Already the implementation of standard algorithms like dense matrix-matrix multiplications requires a considerable amount of sophistication in order to utilize the vast computing resources of GPUs efficiently [70].

In the context of the discretized SHE equations (5.9) and (5.16), the assembly can be carried out in parallel for each box $B \in \mathcal{B}$ and each adjoint box $\tilde{B} \in \tilde{\mathcal{B}}$, provided a suitable storage scheme for the sparse system matrix is chosen. Similarly, the elimination of odd-order unknowns from the system matrix can be achieved in parallel, since the procedure can be carried out separately for each row associated with a box B of the system matrix. The iterative solvers essentially rely on sparse matrix-vector products, inner products and vector updates, which can also be run in parallel employing parallel reduction schemes. However, the additional need for preconditioners is a hindrance for a full parallelization, because the design of good parallel preconditioners is very challenging and typically problem-specific [104].

In this chapter a parallel preconditioning scheme for the SHE equations is proposed and evaluated. The physical principles on which the preconditioner is based are discussed in Sec. 7.1 and additional numerical improvements for the system matrix are given in Sec. 7.2. The preconditioner scheme is then proposed in Sec. 7.3 and evaluated for a simple n^+nn^+ -diode in Sec. 7.4. Even though parallel preconditioners suitable for GPUs have already been implemented recently, cf. e.g. [33, 40], their black-box nature does not make full use of all available information. The preconditioner scheme presented in the following incorporates these additional information into otherwise black-box preconditioners.

The scheme is derived for a given electrostatic potential, as it is for instance the case with a Gummel iteration, cf. Sec. 2.4. A block-preconditioner for the Newton scheme is obtained by concatenation of a preconditioner for the Poisson equation, the SHE preconditioner presented in the following, and a preconditioner for the continuity equation for the other carrier type.

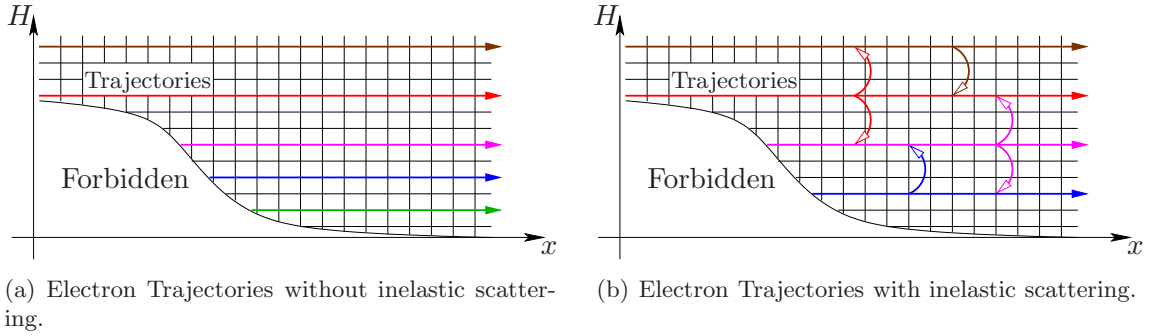


Figure 7.1: Trajectories of carriers in free flight within the device are given by constant total energy H .

7.1 Energy Couplings Revisited

As discussed in Chap. 3, carriers within the device can change their total energy only by inelastic scattering events, thus the scattering operator $Q_{l,m}\{f\}$ is responsible for coupling different energy levels. However, if only elastic scattering processes are considered, the total energy of the particles remains unchanged and the different energy levels do not couple, cf. Fig. 7.1. Therefore, in a SHE simulation using only elastic scattering and N_H different energy levels, the resulting system of linear equations is consequently decoupled into N_H independent problems. Such a decomposition has been observed already in early publications on SHE [21, 105] in a slightly different setting: If the grid spacing with respect to energy is a fraction of the optical phonon energy $\hbar\omega_{\text{op}}$, say $\hbar\omega_{\text{op}}/n$ with integer n , then the system decomposes into n decoupled systems of equations. This observation, however, is of rather limited relevance in practice, since different phonon energies $\hbar\omega_\eta$ for inelastic scattering may be employed simultaneously, cf. Sec. 3.3, hence the system no longer decouples into a reasonably large number of independent systems in order to scale well to a higher number of cores.

It is assumed throughout the following investigations that all unknowns of the discrete linear system of equations referring to a certain energy H_n are enumerated consecutively. A simple interpretation of the system matrix structure is possible if first all unknowns associated with the lowest energy H_1 are enumerated, then all unknowns with energy H_2 and so forth. The unknowns for a certain energy can be enumerated arbitrarily, even though an enumeration such as in Sec. 6.1 is of advantage for easing the understanding of the system matrix structure.

The scattering of carriers is a random process in the sense that the time between two collisions of a particle are random. Equivalently, the mean free flight denotes the average distance a carrier travels before it scatters. As devices are scaled down, the average number of scattering events of a carrier while moving through the device decreases. On the algebraic level of the system matrix, a down-scaling of the device leads to a weaker coupling between different energy levels. This can be reasoned as follows: Consider a one-dimensional device using spherical energy bands, consisting of two boxes B_1 and B_2 with adjoint box $\tilde{B}_{1,2}$. Now, consider the discretization (5.9) and (5.16). In the following, only the proportionality with respect to the box interface area and the box volume are of interest. Consequently, A

is written for a term that carries a dependence on the interface area $A_{1,2}$, and V is written for a term that depends on the box volumes V_1 or V_2 . Since only the asymptotic behavior is of interest, the signs are always taken positive. The discrete system matrix can then be written according to (5.9) and (5.16) in the form

$$\begin{array}{c}
 \\
 \\
 H_1 \\
 \\
 H_2
 \end{array}
 \begin{array}{c}
 \\
 B_1 \\
 B_2 \\
 \tilde{B}_{1,2} \\
 B_1 \\
 B_2 \\
 \tilde{B}_{1,2}
 \end{array}
 \left(
 \begin{array}{ccc|ccc}
 & B_1 & B_2 & \tilde{B}_{1,2} & B_1 & B_2 & \tilde{B}_{1,2} \\
 & V & 0 & A+V & V & 0 & 0 \\
 & 0 & V & A+V & 0 & V & 0 \\
 & A+V & A+V & V & 0 & 0 & 0 \\
 \hline
 & V & 0 & 0 & V & 0 & A+V \\
 & 0 & V & 0 & 0 & V & A+V \\
 & 0 & 0 & 0 & A+V & A+V & V
 \end{array}
 \right), \quad (7.1)$$

where the three rows and columns in each energy block refer to the assembly of the boxes B_1 , B_2 and $\tilde{B}_{1,2}$. An elimination of the odd-order unknowns, i.e. rows and columns three and six, leads to

$$\begin{array}{c}
 \\
 \\
 H_1 \\
 \\
 H_2
 \end{array}
 \begin{array}{c}
 \\
 B_1 \\
 B_2 \\
 B_1 \\
 B_2
 \end{array}
 \left(
 \begin{array}{cc|cc}
 & B_1 & B_2 & \\
 & V + (A+V)^2/V & (A+V)^2/V & \\
 & (A+V)^2/V & V + (A+V)^2/V & \\
 \hline
 & V & 0 & \\
 & 0 & V & \\
 & V + (A+V)^2/V & (A+V)^2/V & \\
 & (A+V)^2/V & V + (A+V)^2/V &
 \end{array}
 \right), \quad (7.2)$$

where again all signs were taken positive for simplicity, since only the asymptotics are of interest. For characteristic box diameter h in an n -dimensional real space there holds $V \sim h^n$ and $A \sim h^{n-1}$, thus the matrix structure when keeping only the lowest powers of h for each entry is asymptotically given by

$$\begin{array}{c}
 \\
 \\
 H_1 \\
 \\
 H_2
 \end{array}
 \begin{array}{c}
 \\
 B_1 \\
 B_2 \\
 B_1 \\
 B_2
 \end{array}
 \left(
 \begin{array}{cc|cc}
 & B_1 & B_2 & \\
 & h^{n-2} & h^{n-2} & \\
 & h^{n-2} & h^{n-2} & \\
 \hline
 & h^n & 0 & \\
 & 0 & h^n & \\
 & h^{n-2} & h^{n-2} & \\
 & h^{n-2} & h^{n-2} &
 \end{array}
 \right). \quad (7.3)$$

Hence, the off-diagonal blocks coupling different energies become negligible as devices are shrunk. The same asymptotics hold true for an arbitrary number of boxes and energy levels, hence the physical principle of reduced scattering of carriers while travelling through the device is well reflected on the discrete level.

7.2 Symmetrization of the System Matrix

With the enumeration of unknowns as suggested in the previous section and using only a single inelastic phonon energy $\hbar\omega$, the structure of the system matrix consists of three block-diagonals. The location of the off-diagonal blocks depends on the spacing of the discrete

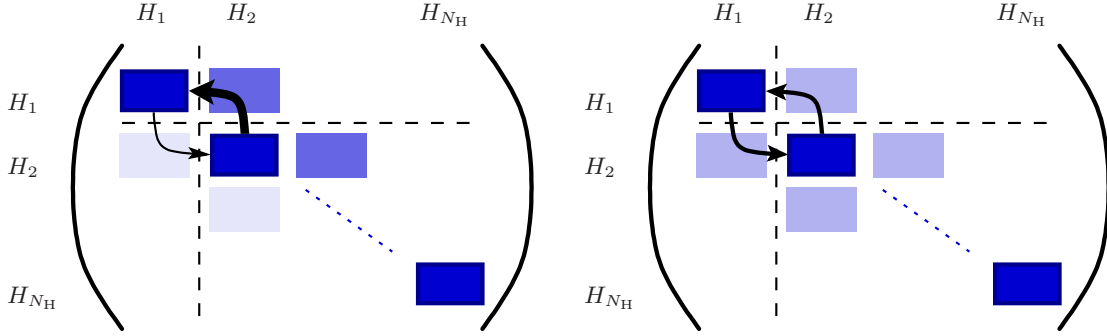


Figure 7.2: Structure of the system matrix for total energy levels $H_1 < H_2 < \dots < H_{N_H}$ with an energy grid spacing equal to the inelastic energy $\hbar\omega$ before (left) and after (right) symmetrization. Unknowns at the same total energy H_n are enumerated consecutively, inducing a block-structure of the system matrix. For simplicity, scattering is depicted between energy levels H_1 and H_2 only, using arrows with thickness proportional to the magnitude of the entries.

energies with respect to $\hbar\omega$. If the energy spacing equals $\hbar\omega$, the matrix is block-tridiagonal, cf. Fig. 7.2.

The asymptotic exponential decay of the distribution function with energy induces a considerable asymmetry of the system matrix when inelastic scattering is considered. This asymmetry, however, is required in order to ensure a Maxwell distribution in equilibrium. Consider the scattering rate (3.25) and the SHE equations for the scattering operator only. The resulting equations for the zeroth-order expansion coefficients using spherical energy bands read

$$\begin{aligned} & -N_{\text{op}}f_{0,0}(\mathbf{x}, H - \hbar\omega)Z(H - \hbar\omega)Z + N_{\text{op}}f_{0,0}ZZ(H + \hbar\omega) \\ & + (N_{\text{op}} + 1)f_{0,0}ZZ(H - \hbar\omega) - (N_{\text{op}} + 1)f_{0,0}(\mathbf{x}, H + \hbar\omega)Z(H + \hbar\omega)Z = 0, \end{aligned} \quad (7.4)$$

where the symmetric scattering rate σ has been cancelled already. The first two terms refer to scattering from lower to higher energy, and the last two terms to scattering from higher energy to lower energy. Substitution of the relation

$$N_{\text{op}} + 1 = \frac{1}{\exp\left(\frac{\hbar\omega}{k_B T}\right) - 1} + 1 = \exp\left(\frac{\hbar\omega}{k_B T}\right)N_{\text{op}}, \quad (7.5)$$

and division by N_{op} leads to

$$\begin{aligned} & -f_{0,0}(\mathbf{x}, H - \hbar\omega)Z(H - \hbar\omega)Z + f_{0,0}ZZ(H + \hbar\omega) \\ & + \exp\left(\frac{\hbar\omega}{k_B T}\right)f_{0,0}ZZ(H - \hbar\omega) - \exp\left(\frac{\hbar\omega}{k_B T}\right)f_{0,0}(\mathbf{x}, H + \hbar\omega)Z(H + \hbar\omega)Z = 0. \end{aligned} \quad (7.6)$$

It can readily be seen that a Maxwell distribution $f(\mathbf{x}, H) = \exp(-\varepsilon(H)/(k_B T))$ fulfills the equation. For the system matrix one consequently finds that the off-diagonal block coupling to higher energy is by a factor of $\exp(\hbar\omega/(k_B T))$ larger than the block coupling to lower energy. For phonon energies of about $\hbar\omega \approx 26$ meV the factor is $\exp(1) \doteq 2.7$, while for phonon energies $\hbar\omega \approx 52$ meV the factor becomes $\exp(2) \doteq 7.4$. The induced asymmetry

of the system matrix is in particular a concern for the convergence of iterative solvers if the off-diagonal block coupling to higher energies dominates the diagonal block, which is typically the case for devices in the micrometer regime.

The asymmetry can be substantially reduced in two ways. The first possibility is to expand the distribution function as

$$f(\mathbf{x}, \mathbf{k}, t) = \sum_{l=0}^{\infty} \sum_{m=-l}^l \exp(-E(\varepsilon)) f_{l,m}(\mathbf{x}, \varepsilon, t) Y_{l,m}(\theta, \varphi), \quad (7.7)$$

where $E(\varepsilon)$ is a reasonable estimate for $\log(f_{0,0})$. A first guess for the first iteration of a self-consistent iteration is a Maxwell distribution,

$$E(\varepsilon) = \frac{\varepsilon}{k_{\text{B}}T}, \quad (7.8)$$

which can be refined in subsequent iterations with the shape of the computed distribution function from the last iterate. A disadvantage of the expansion (7.7) is that the SHE equations need to be slightly adjusted and thus depend on the scaling $E(\varepsilon)$. However, the discrete representations (5.4) and (5.5) approximate the expansion coefficients and hence the distribution function as piecewise constant over the boxes in \mathcal{B} and $\tilde{\mathcal{B}}$. While this is a crude approximation for the exponentially decaying expansion coefficients $f_{l,m}$ of the exponentially decaying distribution function f using the standard expansion $f = f_{l,m} Y^{l,m}$, an expansion of the form (7.7) leads to much smaller variations of the expansion coefficients $f_{l,m}$. Consequently, the exponential decay is basically covered by $E(\varepsilon)$, and a piecewise constant approximation of $f_{l,m}$ is more appropriate.

The second way of reducing asymmetry is based on modifications of the linear system. Denoting again with $E(\varepsilon)$ a reasonable estimate for $\log(f_{0,0})$, the system of linear equations with eliminated odd expansion orders

$$\mathbf{S}_{\text{h}} \mathbf{f}_{\text{h}} = \mathbf{b}_{\text{h}} \quad (7.9)$$

can be rewritten as

$$\mathbf{S}_{\text{h}} \mathbf{E} \mathbf{E}^{-1} \mathbf{f}_{\text{h}} = \mathbf{b}_{\text{h}}, \quad (7.10)$$

where \mathbf{E} is given in block structure as

$$\mathbf{E} = \begin{pmatrix} \exp(-E(\varepsilon(H_1))) \mathbf{I}_1 & 0 & \dots & 0 \\ 0 & \exp(-E(\varepsilon(H_2))) \mathbf{I}_2 & \dots & 0 \\ \vdots & \vdots & \ddots & \vdots \\ 0 & 0 & \dots & \exp(-E(\varepsilon(H_{N_{\text{H}}})) \mathbf{I}_{N_{\text{H}}}) \end{pmatrix} \quad (7.11)$$

with \mathbf{I}_n referring to an identity matrix with dimensions given by the unknowns at energy level H_n . Introducing $\tilde{\mathbf{S}} := \mathbf{S}_{\text{h}} \mathbf{E}$ and $\tilde{\mathbf{f}} := \mathbf{E}^{-1} \mathbf{f}_{\text{h}}$, one arrives at

$$\tilde{\mathbf{S}} \tilde{\mathbf{f}} = \mathbf{b}_{\text{h}}. \quad (7.12)$$

Since \mathbf{E} is a diagonal matrix, the costs of computing $\tilde{\mathbf{S}}$ and $\tilde{\mathbf{f}}$ are comparable to a matrix-vector product and thus negligible. The benefit of this rescaling is that the unknowns

computed in vector $\tilde{\mathbf{f}}$ are roughly of the same magnitude and that the off-diagonal coupling entries in each row of $\tilde{\mathbf{S}}$ are essentially identical. It should be noted that the rescaling on the discrete level is actually a special case of an expansion of the form (7.7), where $E(\varepsilon)$ is taken constant in each box of the simulation domain in (\mathbf{x}, H) -space.

A second look at the rescaled system matrix $\tilde{\mathbf{S}}$ shows that norms of the columns are now exponentially decreasing with energy, while the column norms of \mathbf{S}_h are of about the same order of magnitude. Hence, the rescaling with \mathbf{E} has shifted the exponential decay of the entries in \mathbf{f} to the columns of the system matrix. However, due to the block structure of the system matrix, a normalization of the row-norms by left-multiplication of the linear system with a diagonal matrix \mathbf{D} also rescales the column-norms suitably:

$$\mathbf{D}^{-1}\tilde{\mathbf{S}}\tilde{\mathbf{f}} = \mathbf{D}^{-1}\mathbf{b}_h, \quad (7.13)$$

where

$$\mathbf{D} = \begin{pmatrix} \sqrt{\sum_j S_{0,j}^2} & 0 & \dots & 0 \\ 0 & \sqrt{\sum_j S_{1,j}^2} & \dots & 0 \\ \vdots & \vdots & \ddots & \vdots \\ 0 & 0 & \dots & \sqrt{\sum_j S_{N,j}^2} \end{pmatrix}, \quad (7.14)$$

with N denoting the number of rows in $\tilde{\mathbf{S}}$. Again, the application of \mathbf{D} is computationally cheap and leads with $\hat{\mathbf{S}} := \mathbf{D}^{-1}\tilde{\mathbf{S}}$ and $\hat{\mathbf{b}} = \mathbf{D}^{-1}\mathbf{b}_h$ to the linear system

$$\hat{\mathbf{S}}\tilde{\mathbf{f}} = \hat{\mathbf{b}}. \quad (7.15)$$

It is worthwhile to note that the diagonal entries of \mathbf{D}^{-1} are essentially proportional to $\exp(\varepsilon/(k_B T))$ and thus represent the MEDS factors from Sec. 2.3. In addition, also the exponential decay of values in \mathbf{b} due to Maxwell distributions induced by suitable boundary conditions is automatically rescaled to values in about the same order of magnitude.

7.3 A Parallel Preconditioning Scheme

Due to the large number of unknowns for the discretized SHE equations, the solution of the resulting systems of linear equations is typically achieved by iterative methods. The rate of convergence of these methods can be substantially improved by the use of preconditioners. As already observed by Jungemann *et al.* [53], good preconditioners are actually *required* in most cases to obtain convergence of iterative solvers for the SHE equations. One of the most commonly employed preconditioners is the incomplete LU factorization (ILU), which has been used in recent works on the SHE method [42, 53]. For this reason, a short description of ILU is given in the following.

ILU relies on an approximate factorization of the sparse system matrix \mathbf{A} into $\mathbf{A} \approx \mathbf{LU} =: \mathbf{P}$, where \mathbf{L} is a sparse lower triangular matrix, and \mathbf{U} is a sparse upper triangular matrix. During the iterative solver run, the current residual \mathbf{r}_k is then updated by

$$\mathbf{r}_k \leftarrow \mathbf{P}^{-1}\mathbf{r}_k \quad (7.16)$$

in order to formally solve the system

$$\mathbf{P}^{-1}\mathbf{A}\mathbf{x} = \mathbf{P}^{-1}\mathbf{b} \quad (7.17)$$

rather than $\mathbf{A}\mathbf{x} = \mathbf{b}$. If $\mathbf{P}^{-1} = \mathbf{A}^{-1}$, i.e. the factorization is exact, the solution is obtained in one step. Conversely, if \mathbf{P} is the identity matrix, the linear system is solved as if no preconditioner were employed.

The inverse of \mathbf{P} is never computed explicitly. Instead, a forward substitution $\mathbf{L}\mathbf{y} = \mathbf{r}_k$ followed by a backward substitution $\mathbf{U}\mathbf{r}_k = \mathbf{y}$ is carried out. Since these substitutions are serial operations, the application of the preconditioner to the residual is identified as a bottleneck for parallelism.

In light of the discussion of the block structure of the system matrix \mathbf{S} for SHE, consider a block-diagonal matrix

$$\mathbf{A} = \begin{pmatrix} \mathbf{A}_{1,1} & 0 & \dots & 0 \\ 0 & \mathbf{A}_{2,2} & \dots & 0 \\ \vdots & \vdots & \ddots & \vdots \\ 0 & 0 & \dots & \mathbf{A}_{N_H, N_H} \end{pmatrix}, \quad (7.18)$$

where the N_H square blocks of \mathbf{A} can have arbitrary size. Then, the solution of the system

$$\mathbf{A}\mathbf{x} = \mathbf{b} \quad (7.19)$$

can be obtained by solving each of the systems $\mathbf{A}_{n,n}\mathbf{x}_n = \mathbf{b}_n$ for the respective subvectors \mathbf{x}_n and \mathbf{b}_n separately. Denoting with $\mathbf{P}_{n,n}$ the preconditioner for $\mathbf{A}_{n,n}$, the preconditioner for the full system \mathbf{A} is consequently also given in block diagonal form

$$\mathbf{P} = \begin{pmatrix} \mathbf{P}_{1,1} & 0 & \dots & 0 \\ 0 & \mathbf{P}_{2,2} & \dots & 0 \\ \vdots & \vdots & \ddots & \vdots \\ 0 & 0 & \dots & \mathbf{P}_{N_H, N_H} \end{pmatrix}. \quad (7.20)$$

Since the purpose of a preconditioner is to approximate the inverse of the system matrix, the block-diagonal preconditioner \mathbf{P} will provide a good approximation to the inverse of \mathbf{A} even if \mathbf{A} is not strictly block diagonal, but has small entries in off-diagonal blocks. However, this is exactly the case for the system matrix resulting from the SHE equations discussed in Sec. 7.1. Summing up, the proposed preconditioning scheme reads as follows:

Algorithm 5 (Parallel Preconditioner Scheme for the SHE Method). *Let the number of unknowns at the discrete energies H_n , $n = 1, \dots, N_H$, be given by N_n . Denote the diagonal blocks of the system matrix $\hat{\mathbf{S}}$ with size $N_n \times N_n$ as $\hat{\mathbf{S}}_{n,n}$. Then, a parallel preconditioner for $\hat{\mathbf{S}}$ is given by a block-preconditioner \mathbf{P} , where the preconditioners $\mathbf{P}_{n,n}$ are computed from the diagonal blocks $\hat{\mathbf{S}}_{n,n}$ of $\hat{\mathbf{S}}$ and applied in parallel.*

A physical interpretation of the proposed preconditioner is as follows: Consider the discretization of the SHE equations without inelastic scattering mechanisms. In this case the system matrix $\mathbf{S}_{\text{elastic}}$ after row-normalization is block-diagonal if enumerating the

unknowns as suggested in Sec. 7.1. A preconditioner for $\mathbf{S}_{\text{elastic}}$ is given by a block preconditioner $\mathbf{P}_{\text{elastic}}$ of the form (7.20). Since $\mathbf{S}_{\text{elastic}}$ is an approximation to the SHE equations with inelastic scattering given by $\hat{\mathbf{S}}$, for a preconditioner $\hat{\mathbf{P}}$ for $\hat{\mathbf{S}}$ there holds

$$\hat{\mathbf{P}}^{-1} \stackrel{!}{\approx} \hat{\mathbf{S}}^{-1} \approx \mathbf{S}_{\text{elastic}}^{-1} \approx \mathbf{P}_{\text{elastic}}^{-1}. \quad (7.21)$$

The use of the block diagonals of $\hat{\mathbf{S}}$ rather than the matrix $\mathbf{S}_{\text{elastic}}$ for the setup of the preconditioner $\hat{\mathbf{P}}$ is of advantage because it avoids the setup of the matrix $\mathbf{S}_{\text{elastic}}$.

It should be noted that the use of block preconditioners of the form (7.20) for the parallelization of ILU preconditioners is not new [88]. However, without additional information about the system matrix, the block sizes are usually chosen uniformly and may not be aligned to the block sizes induced by the SHE equations. Consequently, the application of block-diagonal preconditioners to the SHE equations in a black-box manner will show lower computational efficiency.

The proposed scheme in Algorithm 5 allows for the use of arbitrary preconditioners for each of the blocks $\hat{\mathbf{S}}_{n,n}$. Consequently, a preconditioner *scheme* is proposed rather than a single preconditioner, enabling the use of established serial preconditioners in a parallel setting. Since the number of energies N_{H} is in typical situations chosen to be at least 100, the proposed scheme provides a sufficiently high degree of parallelism even for multi-CPU clusters. The situation is slightly different for GPUs, where typically one work group¹ is used for the preconditioner at total energy H_n . Due to the massively parallel architecture of GPUs, an even higher degree of parallelism is desired in order to scale the SHE method well to multi-GPU environments. In such case, parallel preconditioner for each block $\hat{\mathbf{S}}_{n,n}$ should be employed.

7.4 Results

Execution times of the iterative BiCGStab [102] solver are compared for a single CPU core using an incomplete LU factorization with threshold (ILUT) for the full system matrix, and for the proposed parallel scheme using multiple CPU cores of a quad-core Intel Core i7 960 CPU with eight logical cores. In addition, comparisons for a NVIDIA Geforce GTX 580 GPU are found in Figs. 7.3. The parallelization on the CPU is achieved using the Boost.Thread library [6], and the same development time was allotted for developing the OpenCL [57] kernel for ViennaCL [111] on the GPU. This allows for a comparison of the results not only in terms of execution speed, but also in terms of productivity [7].

As can be seen in Figs. 7.3, the performance increase for each linear solver step is more than one order of magnitude compared to the single-core implementation. This super-linear scaling with respect to the number of cores on the CPU is due to the better caching possibilities obtained by the higher data locality within the block-preconditioner.

The required number of iterations using the block-preconditioner decreases with the device size. For an intrinsic region of 25 nm length, the number of iterations is only twice than that of an ILUT preconditioner for the full system. At an intrinsic region of 200 nm, four times the number of iterations are required. This is a very small price to pay for the excellent parallelization possibilities.

¹A work group is a collection of threads that can be synchronized during the execution of a compute kernel. Typically, a work group refers to one of the single-instruction-multiple-data units on the GPU.

Overall, the multi-core implementation is on the test machine by a factor of three to ten faster than the single core-implementation even though a slightly larger number of solver iterations is required. It is reasonable to expect even higher performance gains on multi-socket machines equipped with a higher number of CPU cores. The purely GPU-based solver with hundreds of simultaneous lightweight threads is by up to one order of magnitude faster than the single-core CPU implementation, where it has to be noted that a single GPU thread provides less processing power than a CPU thread.

The comparison in Fig. 7.3 further shows that the SHE order does not have a notable influence on the block-preconditioner efficiency compared to the full preconditioner. The slightly larger number of solver iterations for third-order expansions is due to the higher number of unknowns in the linear system. The performance gain is almost uniform over the length of the intrinsic region and slightly favors shorter devices, thus making the scheme an ideal candidate for current and future scaled-down devices.

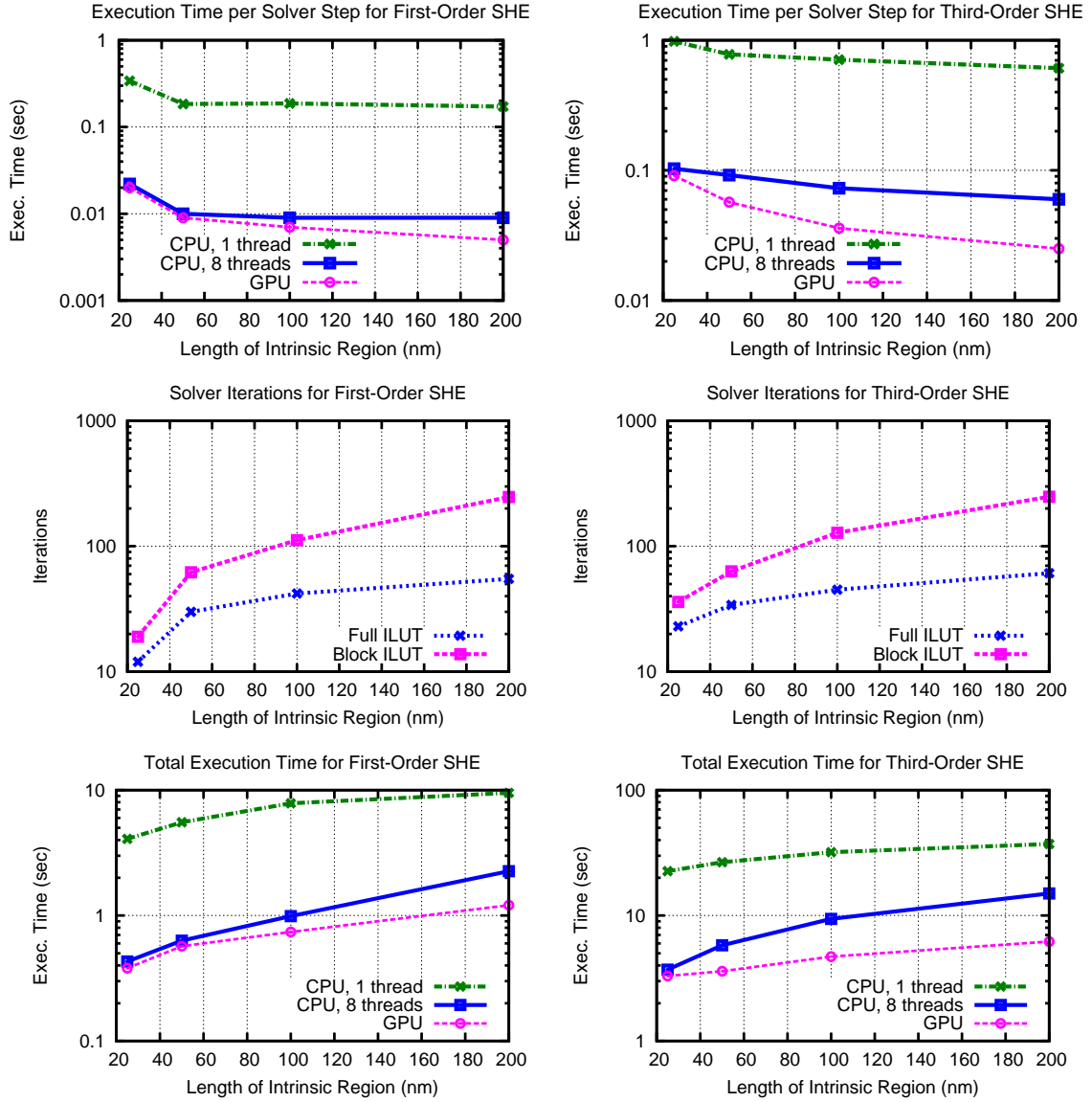


Figure 7.3: Execution times per solver iteration, number of solver iterations and total solver execution time for a first-order (left) and a third-order (right) SHE simulation of n^+nn^+ diodes with different lengths of the intrinsic region. As expected from physical arguments, the parallel preconditioner performs the better the smaller the length of the intrinsic region becomes. The GPU version performs particularly well for the computationally more challenging third-order SHE. A reduction of total execution times compared to a single-threaded implementation by one order of magnitude is obtained.

Chapter 8

Numerical Results

In the previous chapters comparisons for the proposed methods have mostly been given for a n^+nn^+ -diode. The aim of this chapter is to show that the proposed methods blend well and lead to considerable performance improvements for realistic device geometries. First, spatially two-dimensional simulations are presented for a MOSFET-like device. Then, it is shown that the combination of the proposed extensions to the SHE method allow for the simulation of a fully three-dimensional FinFET on an average workstation.

The average workstation is considered to be a machine equipped with a Intel Core i7 960 CPU, 12 GB RAM and a NVIDIA GeForce GTX 580. For simplicity, Dirichlet boundary conditions are used at the contacts and a parabolic energy band model is employed. Self-consistency of the Poisson equation, the SHE equations for electrons, and the drift-diffusion equation for holes is obtained by means of a damped Gummel iteration. The energy spacing is set to 12.5 meV, and acoustical, optical and ionized impurity scattering mechanisms are considered. For simplicity, doping profiles are chosen constant in each segment of the device. Note that doping profiles in realistic devices are smeared out due to unavoidable diffusion, which is beneficial for the numerical stability. Since the more challenging case of constant doping profiles is considered here, the results in this chapter can be transferred to realistic doping profiles.

The meshes used in the next sections are generated with Netgen [91]. Simulator output is written to VTK files [59], which are then processed for visualization by the open-source software ParaView [58].

8.1 MOSFET

The adaptive variable-order scheme presented in Chap. 6 is applied to the simulation of an n -channel MOSFET in unipolar approximation with a channel length of 22 nm. Simulations are carried out using the unstructured triangular mesh depicted in Fig. 5.7. The doping concentration in the source and drain regions are set to 10^{20} cm^{-3} , and to 10^{16} cm^{-3} in the channel and in the bulk regions. A high- k hafnium oxide with a thickness of 3.5 nm is used. Doping profiles change abruptly between the individual regions for simplicity. Note that this is not realistic from a technological point of view, and is usually more challenging for the numerical point of view. The source and the bulk contacts are grounded, while the drain contact is biased at 0.9 Volts. The gate voltage is set to 0.7 Volts. Due to the unipolar approximation with rather high doping in the channel region, there is a spurious current

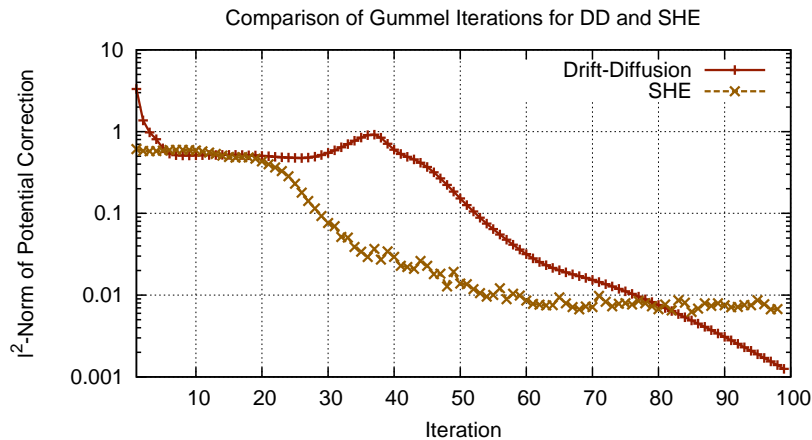


Figure 8.1: Comparison of the convergence of a drift-diffusion simulation and the SHE simulation. The iteration for the SHE method saturates because of the discretization error of the potential-dependent grid in the total energy variable.

flow between the drain and the body contact. Nevertheless, the characteristic behavior in the channel is observed and is used for an evaluation.

To obtain self-consistency with the Poisson equation, a damped Gummel iteration of a first-order SHE with 100 iterations and a damping coefficient of 0.6 is carried out. The discrete l^2 -norm of the potential update vector in each iteration is depicted in Fig. 8.1. Comparable convergence behavior is obtained for both the drift-diffusion and the SHE approach. Note that the SHE simulation starts with a lower, yet significant initial update, because the result of the drift-diffusion simulation is used as initial guess for the SHE simulation. As the iteration progresses, the SHE method saturates, which stems from the discretization error with respect to the potential-dependent band edge influencing the simulation domain in (\mathbf{x}, H) -space, cf. Sec. 2.3. In any case, the potential update is essentially homogeneous over the device, hence the infinity norm of the potential update is around 10^{-5} .

Simulated carrier concentrations are depicted in Fig. 8.2. Densities have been computed from a uniform fifth-order SHE, while Gummel iterations for self-consistency have been carried out for a first-order SHE only. The inconsistencies near the source and drain contacts are due to the lack of full self-consistency of the fifth-order SHE with the Poisson equation, which is amplified by the use of Dirichlet boundary conditions. Consequently, it is concluded that it is insufficient to ensure self-consistency with a first-order SHE only.

Inside the channel a pinch-off can readily be observed. Furthermore, the plot of the carrier density above one electron Volt shows the exponential increase of carriers with high energy along the channel. It has to be emphasized that such an information cannot be obtained from macroscopic transport models such as the drift-diffusion model. For the unipolar simulation of a MOSFET considered here, a high population of heated electrons is obtained all over the drain region, which is about ten orders of magnitude higher than in the source region.

Fig. 8.3 shows a plot of the electrostatic potential and the energy distribution function. Due to the small device dimensions, carriers are injected quasi-ballistically into the drain region. This leads to high values of the distribution function at kinetic energies around 0.9 eV, which is the cause of the high concentration of electrons above 1 eV shown in

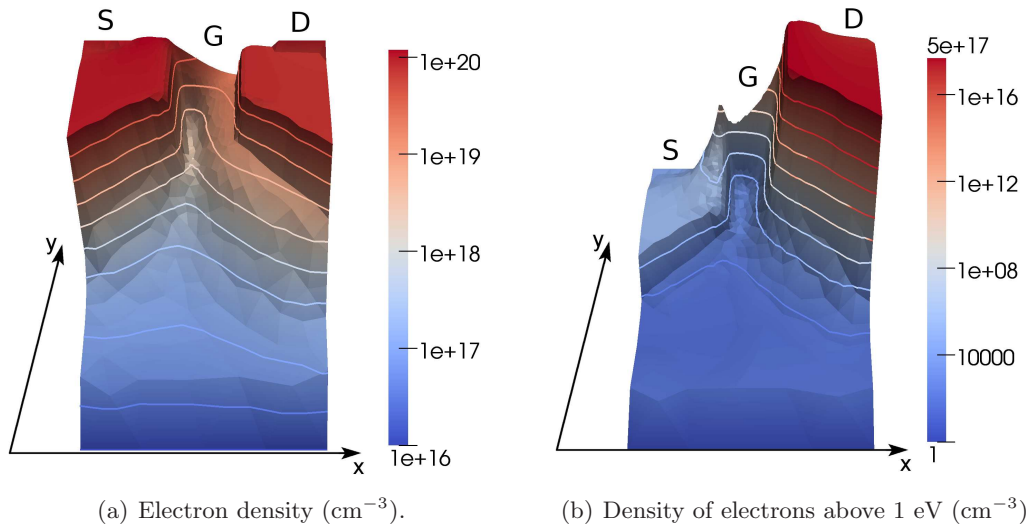


Figure 8.2: Macroscopic quantities obtained from a SHE simulation of the MOSFET. Densities are computed from a fifth-order SHE, while self-consistency is ensured for a first-order SHE only.

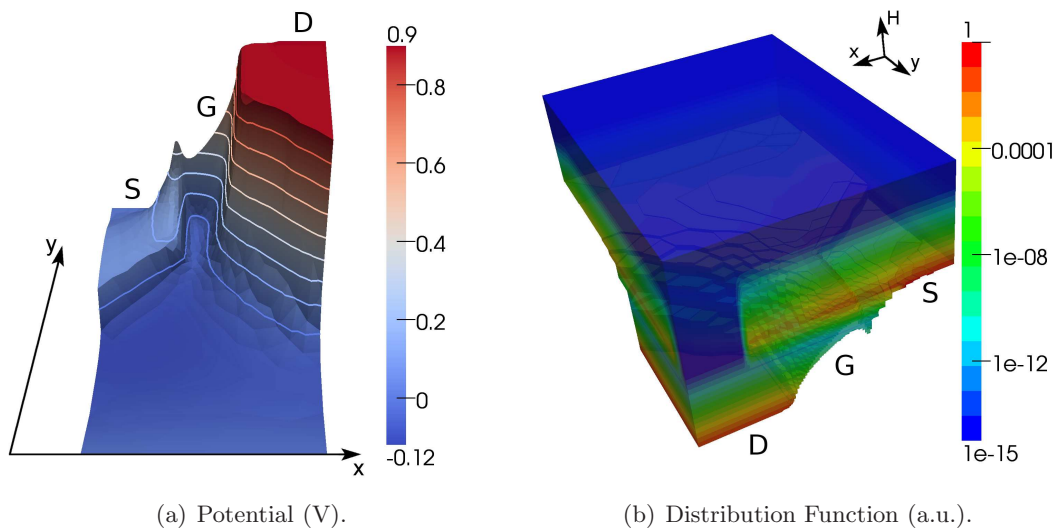


Figure 8.3: Plot of the electrostatic potential and the normalized isotropic part $f_{0,0}$ of the distribution function.

Fig. 8.2. Furthermore, the Dirichlet boundary conditions at the drain contact lead to a boundary layer of the distribution function, which is a purely numerical effect. Therefore, other boundary conditions such as those proposed by Hong *et al.* [42] should be used for predictive device simulation.

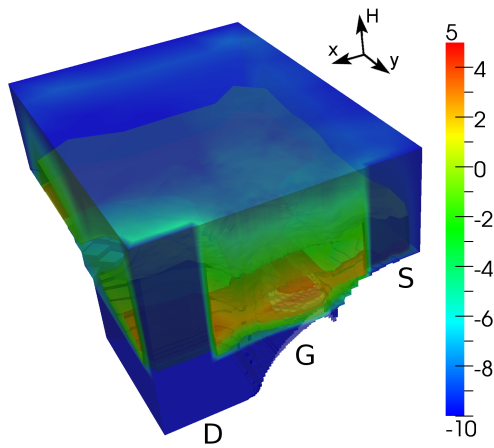
The decay-based strategy as discussed in Chap. 6 is applied for an adaptive variable-order SHE using the same parameters as for the simulation of the n^+nn^+ diode to the MOSFET. Clearly, the obtained results are not the best possible, yet they allow for judging the need for parameter adjustments over a wider range of devices. Fig. 8.4 shows the expansion order indicators obtained from a uniform first-order SHE and from the subsequent variable-order simulation. The expansion orders after the first and the second adaption step are particularly increased near the band-edge and around the channel. In the drain region, a hot energy tail of the distribution function leads to an increase of the expansion order above 0.8 eV only. At very high energies, a first-order expansion is preserved. It is worthwhile to note that almost all third-order expansion nodes become fifth-order expansion nodes after the second adaption step. Additional savings from a better parametrized error indicator are therefore expected. Nevertheless, the number of unknowns in Fig. 8.5 is reduced by a factor of up to two for fifth-order expansions, and execution times are reduced by a factor of almost five due to the sparser population of the system matrix at lower expansion orders, cf. Fig. 8.6. The high gain in execution time may also be due to better caching possibilities on the CPU, because data operations are more localized and thus less cache misses occur. Performance gains from a parallelization are comparable to the results in Sec. 7.4. It has to be mentioned that a uniform fifth-order SHE of the MOSFET leads to a linear system and a preconditioner which is too large in order to fit into GPU RAM. Therefore, additional fallback-mechanisms are required when using GPU acceleration with SHE.

A comparison of the average carrier energy in Fig. 8.7 again confirms convergence of the SHE method and further shows that adaptive expansion orders lead to accuracy comparable to uniform expansions. The kinks in the error function are due to the interpolation of the solution quantities along a line passing through the mesh at a depth of 2 nm below the gate oxide. It is crucial to note that unlike in the case of the n^+nn^+ diode simulated in Sec. 6.3, a first-order SHE leads to a significant error in the average carrier energy, thus confirming that higher-order SHE is indeed required for modern scaled-down devices.

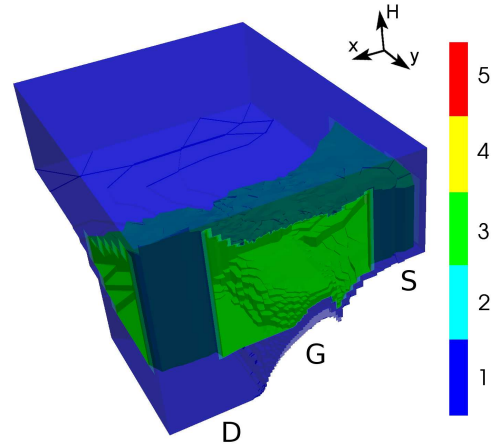
8.2 FinFET

While transistors have been fabricated as planar devices over decades, the small feature sizes of modern devices leads to the undesired effect that the gate loses control over the current flow. One of the possible remedies currently employed is the use of fully three-dimensional device layouts, such that the channel is fabricated as a fin, and the gate is wrapped around the fin in order to have better control over the current flow. A schematic view of such a so-called FinFET is given in Fig. 8.8 and investigated in the following. Since three faces of the channel are used to control current flow, the device is sometimes also referred to as *trigate transistor*.

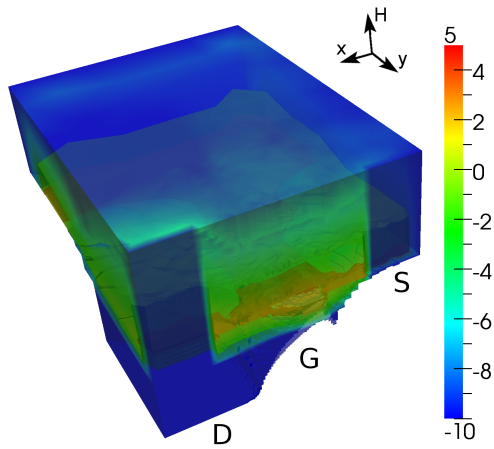
Due to symmetry considerations along the fin, it is sufficient to simulate only one half of the device. The simulated device has a channel length of 18 nm and the mesh used for the simulation is depicted in Fig. 5.8. A constant doping of 10^{20} cm^{-3} is applied in the source and drain contacts, while a doping of 10^{12} cm^{-3} is applied in the channel and in the



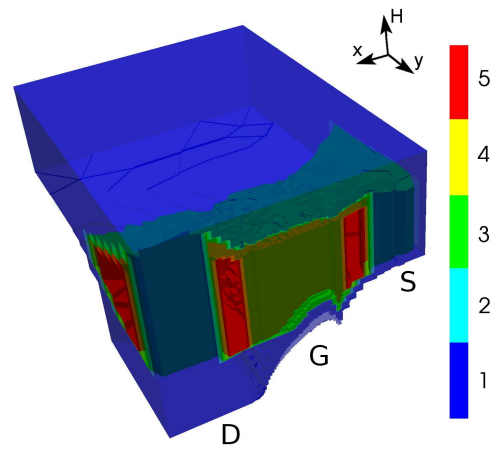
(a) Error indicator computed for the first adaption step.



(b) Expansion orders after the first adaption step.



(c) Error indicator computed for the second adaption step.



(d) Expansion orders after the second adaption step.

Figure 8.4: Error indicator and expansion order distribution after the first and second adaption step. At the contacts, the error indicator is set to -10 and a first-order expansion is preserved. Here, the bulk is kept at a fixed first order, since the contribution to transport is negligible. The vertical axis denotes total energy.

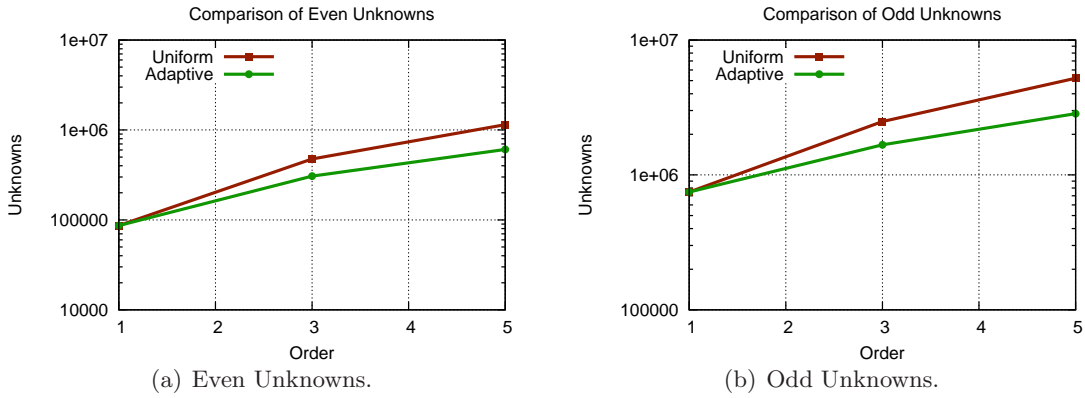


Figure 8.5: Comparison of the number of unknowns of the linear system. The use of adaptive expansion orders leads to a reduction of unknowns by about a factor 1.5 for a third-order expansion, and a factor of 2 for a fifth-order expansion.

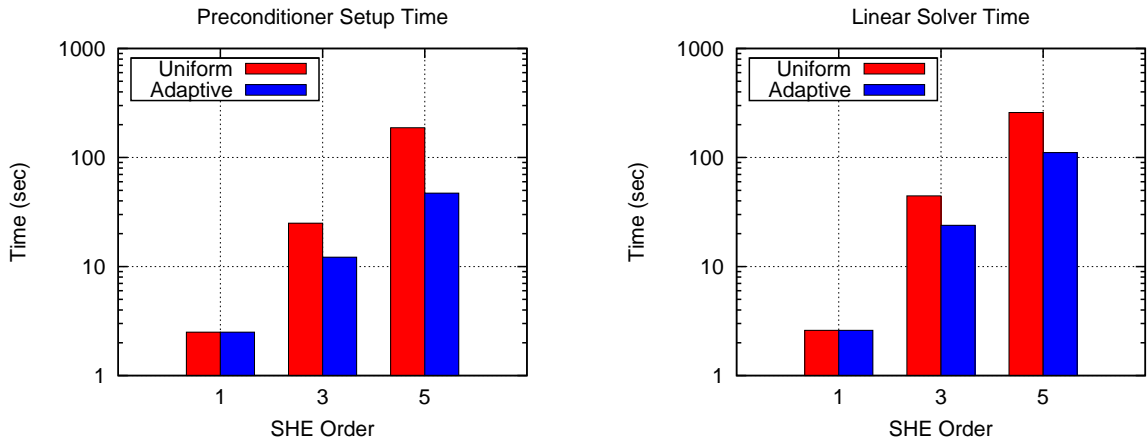
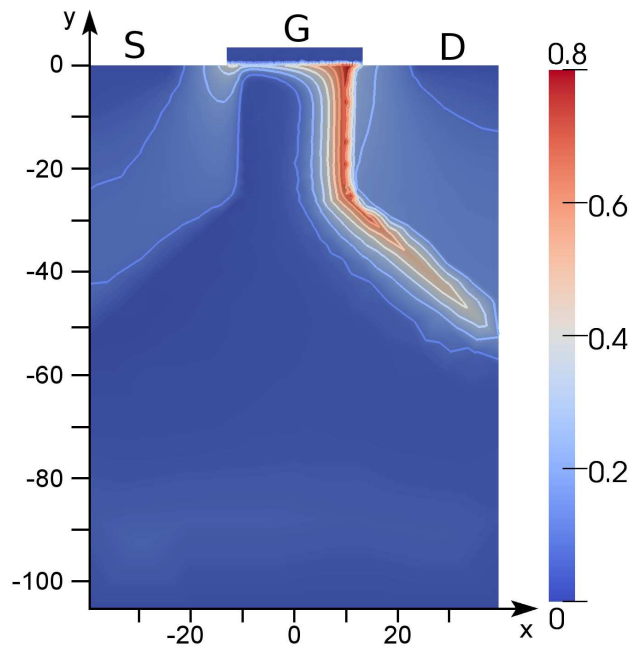
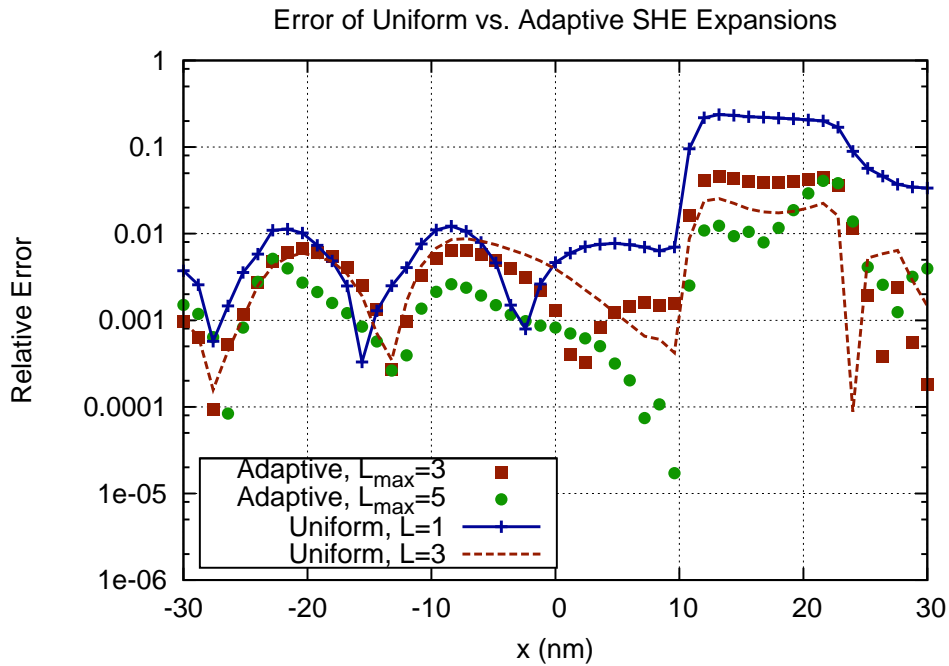


Figure 8.6: Comparison of execution times for the preconditioner setup and the linear solver run using eight CPU threads. The sparser structure of the system matrix leads to a reduction of execution times by a factor of up to four.



(a) Average carrier energies (energy in eV, scale in nm).



(b) Comparison of the relative error of carrier energies.

Figure 8.7: Average carrier energy in the simulated MOSFET. A fifth-order uniform expansion is taken as reference for the comparison of the errors along a line 2 nm below the gate oxide, with $x = 0$ corresponding to the center of the channel. The convergence of the SHE method can readily be seen and adaptive expansions essentially agree with corresponding uniform expansions.

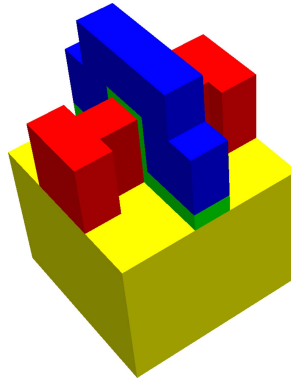


Figure 8.8: Schematic view of the simulated FinFET geometry. The gate is shown in blue, the gate oxide in green, the fin in red and the substrate in yellow.

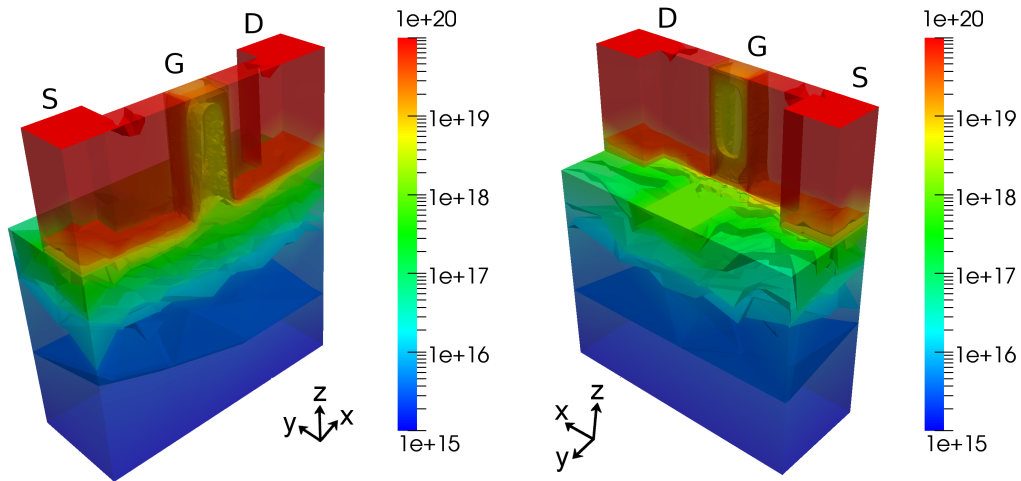


Figure 8.9: Carrier density (in cm^{-3}) in the simulated FinFET. The color scale is truncated below 10^{15} cm^{-3} in order to have a higher resolution in the channel.

bulk. Again, the device is simulated in an unipolar approximation. The source contact is grounded, the drain contact is biased by 0.3 Volt, a gate voltage of 0.8 Volt is applied, and the bulk contact is grounded. Due to the difference in the built-in potential, the Dirichlet boundary conditions for the potential at the bulk contact are set to -0.5 Volt. The results presented in the following are obtained from a uniform first-order SHE, and at the end of this section an adaptive SHE up to third order is discussed.

Fig. 8.9 shows the carrier density inside the device. The accumulation of carriers near the gate oxide is clearly visible, especially along the oxide on top. In the center of the channel, a region of lower carrier density is obtained.

The density of carriers above 1 eV shown in Fig. 8.10 shows a high concentration of hot carriers in the source and drain region towards the channel. The peak concentration is obtained at the beginning of the gate oxide in the source region.

The potential distribution inside the device is depicted in Fig. 8.11, which also depicts the potential inside the oxide. Note that the oxide also extends towards the bulk, where three times the thickness around the fin is chosen. However, the oxide grown on the bulk

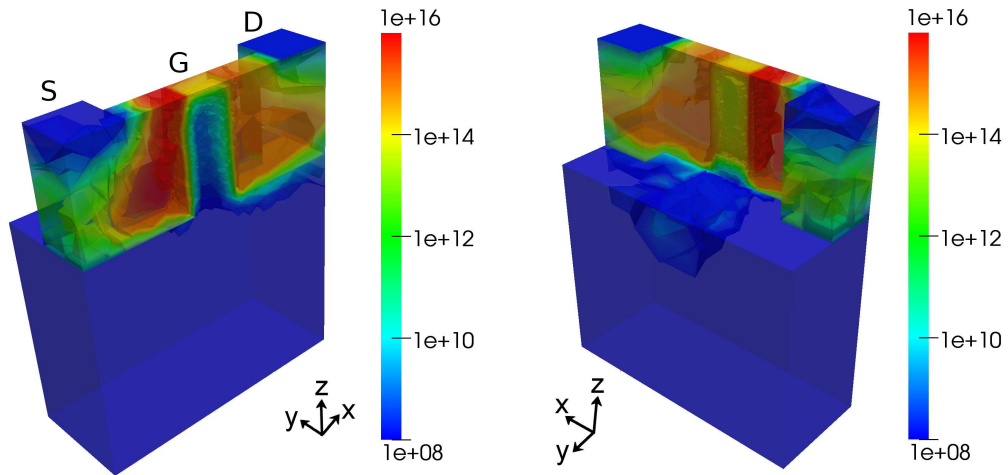


Figure 8.10: Density of carriers with energy above 1 eV (in cm^{-3}) in the simulated FinFET.

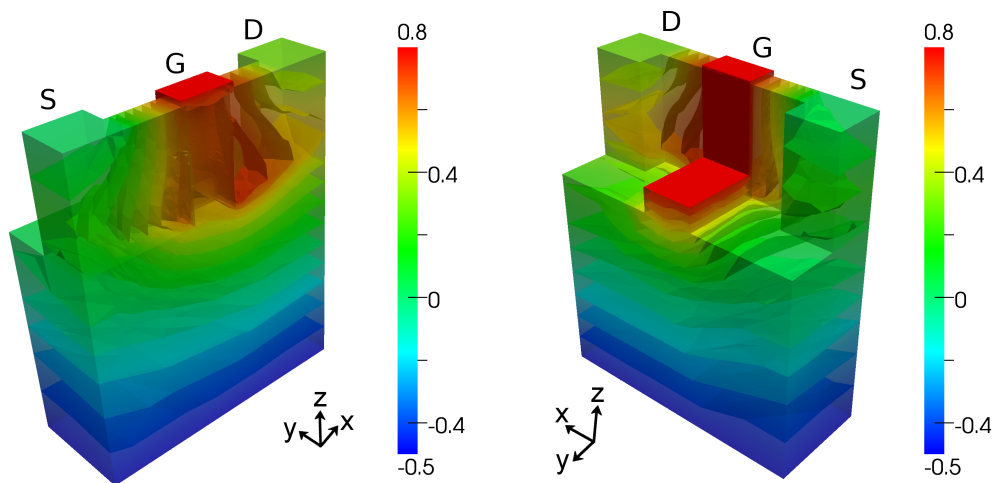


Figure 8.11: Potential in the simulated FinFET. The reference potential is the built-in potential in the source and drain region.

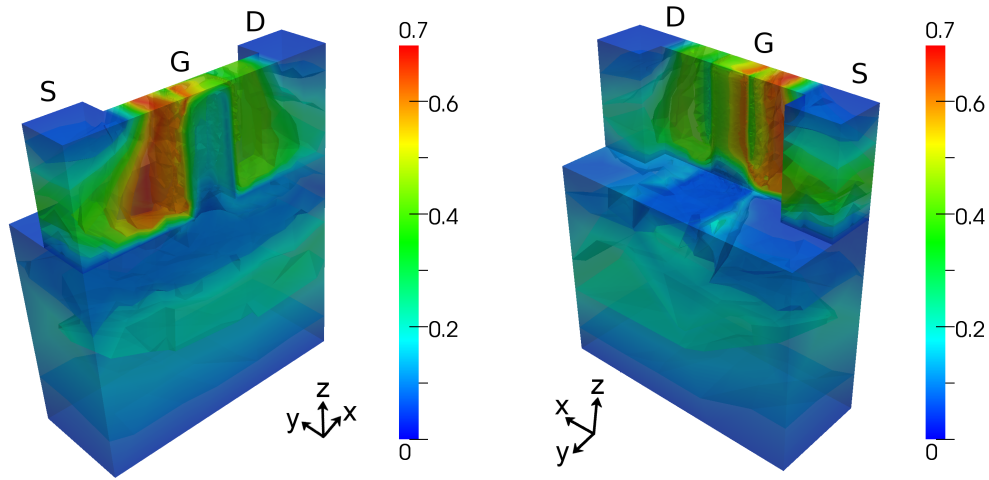


Figure 8.12: Average carrier energy (in eV) in the simulated FinFET.

does not contribute to carrier transport significantly.

Average carrier energies are shown in Fig. 8.12. In contrast to the MOSFET with a high drain-source bias, the low drain-source bias for the FinFET leads to high average carrier energies mostly in the source close to the gate oxide. The elevated carrier energies deeper in the source are due to the high bulk bias.

While the uniform first-order SHE has led to 443 500 even-order unknowns leading to a memory consumption of 5 GB, a uniform third-order expansion results in 3 976 475 even-order unknowns and a memory consumption beyond 20 GB. Since this is beyond the memory provided by the workstation, only an adaptive SHE up to third-order is carried out. Using the same adaptive strategy based on the rate of decay of the expansion coefficients as for the MOSFET, 2 242 040 even-order unknowns are obtained, which is still too large for the workstation. Reducing the threshold value from -6.0 to -1.0 and clamping the bulk and the interior of the channel to first-order results in 860 145 unknowns, which just fits into the 12 GB budget. The expansion order averaged over the full energy range is depicted in Fig. 8.13. The adaptive strategy readily resolves the crucial regions underneath the gate oxide, even though a rather high threshold is chosen.

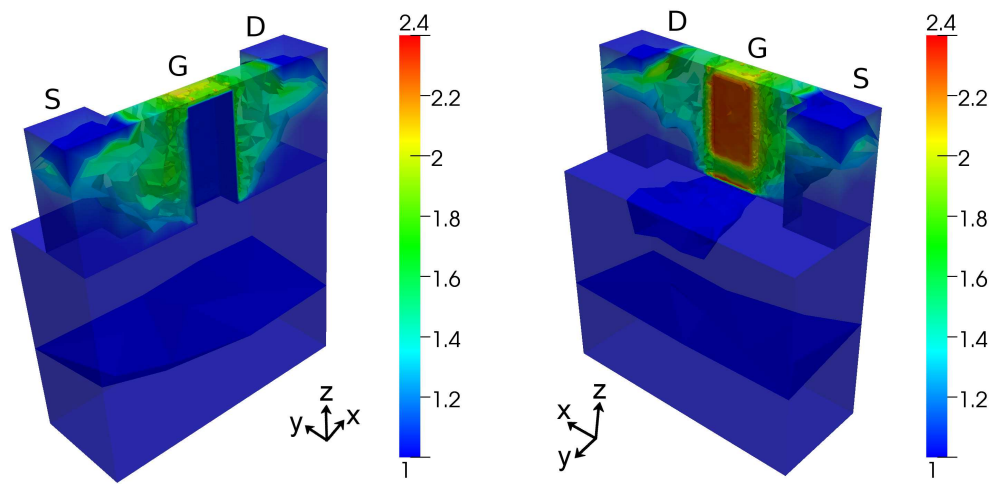


Figure 8.13: Average expansion order after the first adaption step in the simulated FinFET.

Chapter 9

Outlook and Conclusion

Even though several improvements of the SHE method are presented throughout this thesis, many possible further directions remain. In fact, the suggested improvements have led to a number of direct follow-up research topics. Consequently, a discussion of possible further improvements on the SHE method is given in the next section. Finally, a conclusion is drawn.

9.1 Possible Further Improvements of the SHE Method

A lexicographically ordered list of possible improvements is briefly discussed in the following. The selection of topics is mostly based on an improvement of the method from the numerics point of view, because the author considers the method to be more mature from the physics point of view than from the numerics point of view.

9.1.1 Bipolar SHE

The SHE method has so far been applied to either electrons or holes, but not both. The other carrier type has either been modelled by a continuity equation, or has been neglected. However, a distribution function for both carrier polarities is of interest for the investigation of high energy effects such as impact ionization feedback [12, 54], where highly energetic carriers interact with the crystal lattice and generate electron-hole pairs.

A challenging question is in the modeling of generation and recombination of carriers. While for a unipolar SHE the scattering operator $Q\{f\}$ acts on a single distribution function, a bipolar SHE requires the consideration of the distribution functions f^n and f^p for electrons and holes respectively, leading to a scattering operator of the form $Q\{f^n, f^p\}$. A Shockley-Read-Hall-like relaxation-time approach for the generation and regeneration of carriers can serve as a first approach to modelling the interactions of electrons and holes, but higher sophistication is expected to be required for modelling high-energy effects accurately.

9.1.2 Energy Grid with Hanging Nodes

Due to the numerical stabilization using the H -transform discussed in Sec. 2.3, a tensor-prolongation of the mesh in \mathbf{x} -space to the (\mathbf{x}, H) -space is attractive for the discretization presented in Chap. 5. This prolongation for discrete total energies H_1, \dots, H_{N_H} is not fully satisfactory from the numerics point of view: The range of kinetic energies over the

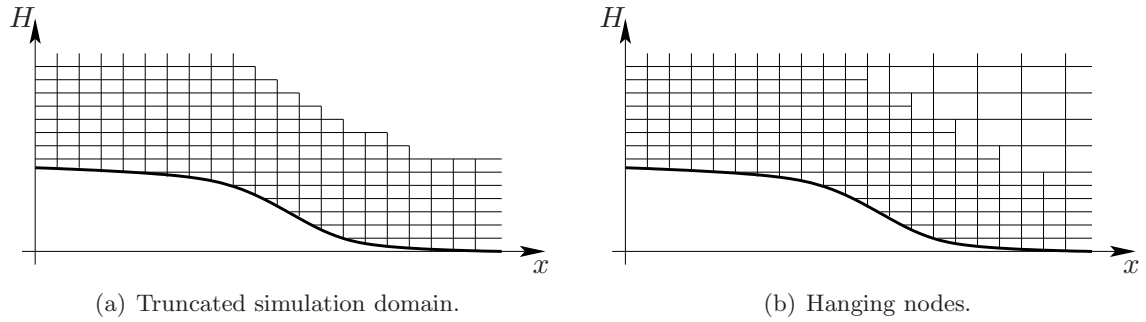


Figure 9.1: Two possibilities for increasing the numerical efficiency of the SHE method by reducing the resolution in low-probability regions in (\mathbf{x}, H) -space.

device varies by an amount of $q\psi_{\max} - q\psi_{\min}$ over the device, where ψ_{\max} and ψ_{\min} denote the maximum and minimum of the electrostatic potential over the device. At low applied voltages, the difference in kinetic energy ranges is about 1 eV, which is certainly acceptable. However, for higher voltages above ten Volts, as it is common for high-power devices, the kinetic energy range consequently varies by more than ten electron volts. This can lead to a resolution of regions of the distribution function with extremely low probabilities of more than 100 orders of magnitude below the probability near the band edge. A resolution of these areas of extremely low probabilities is typically not required, hence computational resources should be focused on regions with higher importance.

Two possible remedies for the reduction of an unnecessary high resolution at high kinetic energies are depicted in Fig. 9.1. The first possibility is to simply truncate the simulation domain above a certain kinetic energy and impose homogeneous Neumann boundary conditions at the new boundaries. The truncation errors are certainly negligible if there is no significant high-energy tail of the distribution function extending into the truncated region. Consequently, such a truncation is particularly interesting for larger devices, where the mean free path of carriers is much smaller than the device dimensions. However, for the case of small devices in the deca-nanometer regime, the high energy tail cannot be neglected and thus a truncation of the simulation domain is inappropriate. Nevertheless, the resolution at higher energies can be reduced by allowing so-called *hanging nodes* inside the mesh. In such an approach, the energy spacing is locally increased from $H_n^+ - H_n^-$ to, say, $H_{n+1}^+ - H_{n-1}^-$. Hanging nodes can also be introduced by the use of nested grids, for which one may in addition decrease the spatial resolution, cf. Fig. 9.1(b). This would further lead to the use of multigrid methods [100] for the SHE method.

The difficulty of a mesh with hanging nodes is in the conservation of current. While the box integration scheme in Chap. 5 asserts current conservation for sufficiently regular Delaunay meshes by construction, it is not directly applicable for meshes with hanging nodes in (\mathbf{x}, H) -space. On the other hand, a violation of the conservation property in low-probability regions may be acceptable, because the error will be in the range of the machine precision due to a violation in low-probability regions only.

9.1.3 Fast Self-Consistency with Poisson's Equation

The nonlinear coupling of the BTE with the Poisson equation requires the use of iteration schemes as discussed in Sec. 2.4. Clearly, it is desirable to keep additional computational

costs due to these nonlinear iterations as small as possible. For simplicity, the discussion is mostly based on uniform expansion orders, but equally applies to adaptive expansion orders presented in Chap. 6 as well.

For a SHE method with order L , a considerable reduction of the total simulation time can be achieved by first computing a self-consistent solution of a first-order expansion, possibly using a coarser grid in \mathbf{x} -space, larger energy spacings in H -space, or both. Since the BTE is coupled with the Poisson equation by the carrier densities only, which in turn depend on the zeroth-order SHE coefficient $f_{0,0}$ only, a first-order SHE provides a very good initial guess for the SHE method of order L . In particular, due to the quadratic convergence of the Newton method it is expected that a single Newton correction step for order L when using first-order SHE as initial guess is sufficient in most cases. While the savings are expected to be a factor of two to three for a third-order SHE, the savings for higher-order expansions will be roughly proportional to the number of nonlinear iterations required for a SHE of order L without improved initial guess for the potential.

The necessity for a nonlinear iteration scheme can directly be linked with adaptive expansion orders: As soon as the potential correction is sufficiently small, expansion orders can be increased. This procedure can be repeated until convergence and a prescribed accuracy is obtained. Even though the required adaptive expansion orders as well as error indicators and adaption strategies have been proposed in this thesis, a systematic study of the use within a nonlinear self-consistency iteration has not been carried out yet.

9.1.4 More Flexible Discretization on Unstructured Grids

The discretization of the SHE equations on Delaunay triangulations as presented in Chap. 5 allows for a considerably better control of the local mesh size. However, the Delaunay criterion is hard or even impossible to fulfill for mesh hierarchies often used within multilevel and multigrid methods. As a consequence, it is desirable to employ discretization schemes suitable for arbitrary unstructured grids.

A possible replacement for the currently employed scheme based on Voronoi diagrams is the use of the barycenter method briefly outlined in Sec. 5.2. The discretization in Sec. 5.3 then needs to be adjusted for the surface integral over the generalized current density $\mathbf{j}_{l,m}$. While each of the facets of a Voronoi box is perpendicular to the respective edge connecting two vertices, this is not the case for the barycenter method. This leads to additional effort, because the normal components of the fluxes with respect to the boxes are not directly available any longer.

An alternative to box integration schemes are mixed finite element schemes as well as discontinuous Galerkin methods, which have gained a lot of popularity recently [39, 49, 85]. Unlike the use of the barycenter method instead of Voronoi diagrams, a discretization for such a case still needs to be derived. Due to the complexity of the BTE, the derivation of a suitable formulation is expected to be considerably more involved than for well-behaved elliptic or parabolic equations.

9.1.5 Preconditioner for the Compressed Matrix Scheme

In Chap. 4 it has been shown that the system matrix for the SHE equations can be written in the form

$$\mathbf{S}_h = \sum_{i=1}^p \mathbf{Q}_i \otimes \mathbf{R}_i, \quad (9.1)$$

where the number of terms p depends on the band structure model employed. The attractiveness of this representation not only stems from the reduction of memory requirements from $\mathcal{O}(NL^2)$ to $\mathcal{O}(N+L^2)$, where N denotes the number of nodes in the (\mathbf{x}, H) simulation domain, but also from the ability to conveniently switch between different expansion orders. Denoting with $\mathbf{S}_{h,L}$ the system matrix resulting from a SHE of the BTE of order L , the system matrices for e.g. $L \in \{1, 3, 5, 7\}$ would have to be set up separately each time. With (9.1), these system matrices are given by replacing \mathbf{R}_i with the respective expansion order.

The main disadvantage of (9.1) are the structural restrictions during the solution phase. Since preconditioners are required to obtain convergence of the iterative solvers, a suitable preconditioner still needs to be found for the representation (9.1). With the availability of adaptive expansion orders and the fact that the SHE method is basically limited by its memory requirements rather than its computational costs, the use of uniform expansion orders with a representation of the form (9.1) makes sense only if the preconditioner requires memory of order $\mathcal{O}(N+L^2)$ or at most $\mathcal{O}(NL^2)$ with a small factor of proportionality in order to be comparable to the memory requirements of the $N(L+1)^2$ unknowns. Otherwise, the use of adaptive expansion orders is likely to be the better choice.

The preconditioner scheme discussed in Chap. 7 requires $\mathcal{O}(NL^2)$ memory with a considerably large constant of proportionality in front, which undermines the advantage of the compressed storage of \mathbf{S}_h . A possibility to reduce memory requirements to $\mathcal{O}(N+L^2)$ is to compute the preconditioner for first-order SHE as usual, and to define in similarity to algebraic multigrid methods suitable transfer operators for the restriction of the residual of the $(L+1)^2$ expansion coefficients to the zeroth-order expansion coefficient, and the prolongation from the zeroth-order coefficient to the $(L+1)^2$ expansion coefficients. However, it is not clear whether suitable transfer operators can be defined.

A different approach is based on an approximation on the algebraic level. Approximating first the the system matrix \mathbf{S}_h by

$$\mathbf{U} = \mathbf{V} \otimes \mathbf{W} \approx \mathbf{S}_h, \quad (9.2)$$

the preconditioner can be computed from \mathbf{U} by the use of the identity $\mathbf{U}^{-1} = \mathbf{V}^{-1} \otimes \mathbf{W}^{-1}$. Consequently, only a preconditioner for \mathbf{V} and one for \mathbf{W} needs to be computed, which then serves as a preconditioner for \mathbf{U} and thus for \mathbf{S}_h . Still, the question of whether such suitable approximations \mathbf{U} to \mathbf{S}_h exist, is still open.

9.2 Conclusion

Throughout this thesis a number of extensions to the SHE method are proposed in order to reduce the computational effort and consequently increase the attractiveness of the method for every-day TCAD purposes. The suggestions enable the simulation of semiconductor devices in the deca-nanometer regime at an unprecedented accuracy for a given time budget.

The increased importance of hot carrier degradation in modern scaled-down devices is addressed by proposing a scheme for the inclusion of carrier-carrier scattering for the SHE method. Unfortunately, the scheme leads to nonlocal coupling of the equations with energy, such that additional computational effort is required. In addition, the SHE equations become nonlinear, which is less a concern since the SHE equations are already nonlinearly coupled with the Poisson equation. Nevertheless, similar complications arise when considering carrier-carrier scattering with the Monte Carlo method.

A thorough investigation of the coupling structure of the SHE equations leads to a matrix compression scheme, which allows for storing the system matrix of the linear system of equations after discretization in a very efficient manner. Even though the method greatly reduces memory requirements, its use is so far hampered by the need for a suitable preconditioner for the iterative solvers. Nevertheless, the method can already be employed in the cases where convergence is obtained without preconditioner, and for the evaluation of residuals for adaptive expansion order strategies.

The formulation and implementation of a higher-order discretization scheme for unstructured grids enables the use of the SHE method as a direct replacement for established macroscopic transport models such as the drift-diffusion model or the hydrodynamic model without changing the underlying mesh. Moreover, the number of unknowns compared to structured grids is reduced considerably, because refinement in unstructured grids leads to a much more localized reduction of the mesh size than for structured grids, especially in three spatial dimensions.

Variable-order expansions achieve the accuracy of uniform expansions at considerably lower computational cost. The extraction of macroscopic quantities such as the carrier velocity or the average carrier energy are shown to require only locally increased expansion orders in the high-probability regions of the distribution function. Three different types of adaptive strategies for the automatic choice of the expansion order are proposed.

To address the shift towards parallel computing architectures, a parallel preconditioner scheme for the SHE method is derived based on physical principles. The resulting block-preconditioner scheme is shown to be able to use modern multi- and many-core computing architectures such as CPUs and GPUs efficiently. Performance gains of up to one order of magnitude compared to single-threaded executions are obtained.

On the overall, the novel methods presented in this thesis allow for a reduction of execution times for device simulations employing the SHE method by up to two orders of magnitude compared to existing approaches. In addition, memory requirements are reduced by about one order of magnitude, thus allowing for higher accuracy for a given amount of memory. The proposed algorithms are implemented in the freely available open source device simulator `ViennaSHE`.

Appendix A

Mathematical Tools

A.1 The Kronecker Product

For matrices $\mathbf{Q} = (Q_{i,j})_{i,j=1}^{n,m} \in \mathbb{R}^{n \times m}$ and $\mathbf{R} \in \mathbb{R}^{p \times q}$, the Kronecker product is defined as the block matrix

$$\mathbf{Q} \otimes \mathbf{R} = \begin{pmatrix} Q_{1,1}\mathbf{R} & Q_{1,2}\mathbf{R} & \cdots & Q_{1,m-1}\mathbf{R} & Q_{1,m}\mathbf{R} \\ Q_{2,1}\mathbf{R} & Q_{2,2}\mathbf{R} & \cdots & Q_{2,m-1}\mathbf{R} & Q_{2,m}\mathbf{R} \\ \vdots & \vdots & \ddots & \vdots & \vdots \\ Q_{n-1,1}\mathbf{R} & Q_{n-1,2}\mathbf{R} & \cdots & Q_{n-1,m-1}\mathbf{R} & Q_{n-1,m}\mathbf{R} \\ Q_{n,1}\mathbf{R} & Q_{n,2}\mathbf{R} & \cdots & Q_{n,m-1}\mathbf{R} & Q_{n,m}\mathbf{R} \end{pmatrix} \in \mathbb{R}^{np \times mq} .$$

The Kronecker product is bilinear and associative, but not commutative. Moreover, if the matrices \mathbf{Q} , \mathbf{R} , \mathbf{S} and \mathbf{T} are such that the products \mathbf{QS} and \mathbf{RT} can be formed, there holds

$$(\mathbf{Q} \otimes \mathbf{R})(\mathbf{S} \otimes \mathbf{T}) = (\mathbf{QS}) \otimes (\mathbf{RT}) .$$

A direct consequence is that $\mathbf{Q} \otimes \mathbf{R}$ is invertible if and only if \mathbf{Q} and \mathbf{R} are invertible. In this case, the inverse is given by

$$(\mathbf{Q} \otimes \mathbf{R})^{-1} = \mathbf{Q}^{-1} \otimes \mathbf{R}^{-1} .$$

Suppose now that $n = m$ and $p = q$, i.e. \mathbf{Q} and \mathbf{R} are square matrices. Let $\lambda_1, \dots, \lambda_n$ denote the eigenvalues of \mathbf{Q} , and μ_1, \dots, μ_p denote the eigenvalues of \mathbf{R} . Then the eigenvalues of $\mathbf{Q} \otimes \mathbf{R}$ are given by

$$\lambda_i \mu_j, \quad i = 1, \dots, n, j = 1, \dots, p .$$

A similar statement holds true for the singular values of general rectangular matrices \mathbf{Q} and \mathbf{R} . In particular, there holds

$$\text{rank}(\mathbf{Q} \otimes \mathbf{R}) = \text{rank } \mathbf{Q} \times \text{rank } \mathbf{R} .$$

A.2 Wigner 3jm Symbols

The symbol

$$\begin{pmatrix} j_1 & j_2 & j_3 \\ m_1 & m_2 & m_3 \end{pmatrix} \quad (\text{A.1})$$

with parameters being either integers or half-integers is called a *Wigner 3jm symbol* arising in coupled angular momenta between two quantum systems. It is zero unless all of the following selection rules apply:

- (i) $m_1 \in \{-|j_1|, \dots, |j_1|\}$, $m_2 \in \{-|j_2|, \dots, |j_2|\}$ and $m_3 \in \{-|j_3|, \dots, |j_3|\}$,
- (ii) $m_1 + m_2 + m_3 = 0$,
- (iii) $|j_1 - j_2| \leq j_3 \leq j_1 + j_2$.

The connection with spherical harmonics is the following:

$$\int_{\Omega} Y_{l_1, m_1} Y_{l_2, m_2} Y_{l_3, m_3} \, d\Omega = \sqrt{\frac{(2l_1 + 1)(2l_2 + 1)(2l_3 + 1)}{4\pi}} \times \begin{pmatrix} l_1 & l_2 & l_3 \\ 0 & 0 & 0 \end{pmatrix} \times \begin{pmatrix} l_1 & l_2 & l_3 \\ m_1 & m_2 & m_3 \end{pmatrix},$$

where the left hand side is often termed *Slater integral*.

Bibliography

- [1] I. Babuška and T. Strouboulis. *The Finite Element Method and its Reliability*. Numerical Mathematics and Scientific Computation. Oxford University Press, 2001.
- [2] N. Ben Abdallah and P. Degond. On a Hierarchy of Macroscopic Models for Semiconductors. *Journal of Mathematical Physics*, 37:3306–3333, 1996.
- [3] N. Ben Abdallah, P. Degond, P. Markowich, and C. Schmeiser. High Field Approximations of the Spherical Harmonics Expansion Model for Semiconductors. *Zeitschrift für angewandte Mathematik und Physik*, 52(2):201–230, 2001.
- [4] J. Bey. *Finite-Volumen- und Mehrgitter-Verfahren für elliptische Randwertprobleme*. B. G. Teubner, 1998.
- [5] K. Blotekjaer. Transport Equations for Electrons in Two-Valley Semiconductors. *IEEE Transactions on Electron Devices*, 17(1):38–47, 1970.
- [6] Boost C++ Libraries. <http://www.boost.org/>.
- [7] R. Bordawekar, U. Bondhugula, and R. Rao. Can CPUs Match GPUs on Performance with Productivity? Experiences with Optimizing a FLOP-intensive Application on CPUs and GPU. Technical report, IBM T. J. Watson Research Center, 2010.
- [8] D. Braess. *Finite Elements. Theory, Fast Solvers and Applications in Solid Mechanics*. Cambridge University Press, 1997.
- [9] A. Bravaix, C. Guerin, V. Huard, D. Roy, J.M. Roux, and E. Vincent. Hot-Carrier Acceleration Factors for Low Power Management in DC-AC Stressed 40nm NMOS Node at High Temperature. In *IEEE International Reliability Physics Symposium*, pages 531–548, 2009.
- [10] H. Brooks. Scattering by Ionized Impurities in Semiconductors. *Physical Review*, 83:879–887, 1951.
- [11] R. Brunetti. A Many-Band Silicon Model for Hot-Electron Transport at High Energies. *Solid State Electronics*, 32:1663–1667, 1989.
- [12] J. D. Bude. Gate Current by Impact Ionization Feedback in Sub-Micron MOSFET Technologies. *IEEE Symposium on VLSI Technology*, pages 101–102, 1995.
- [13] C. Canuto, M. Y. Hussaini, A. Quarteroni, and T. A. Zang. *Spectral Methods*. Springer, 2006.

- [14] J. A. Carrillo, I. M. Gamba, A. Majorana, and C. W. Shu. 2D Semiconductor Device Simulations by WENO-Boltzmann Schemes: Efficiency, Boundary Conditions and Comparison to Monte Carlo Methods. *Journal of Computational Physics*, 214(1):55–80, 2006.
- [15] D. M. Caughey and R. E. Thomas. Carrier Mobilities in Silicon Empirically Related to Doping and Field. In *Proceedings of the IEEE*, volume 55, pages 2192–2193, 1967.
- [16] C. Fischer. *Bauelementsimulation in einer computergestützten Entwurfsumgebung*. PhD thesis, Institute for Microelectronics, TU Wien, 1994.
- [17] P. Fleischmann. *Mesh Generation for Technology CAD in Three Dimensions*. PhD thesis, Institute for Microelectronics, TU Wien, 1999.
- [18] W. Freeden, T. Gervens, and M. Schreiner. *Constructive Approximation on the Sphere*. Numerical Mathematics and Scientific Computation. Clarendon Press, Oxford, 1998.
- [19] M. Galler. *Multigroup Equations for the Description of the Particle Transport in Semiconductors*. Series on Advances in Mathematics for Applied Sciences. World Scientific, 2005.
- [20] W. Gautschi. *Orthogonal Polynomials*. Numerical Mathematics and Scientific Computation. Oxford University Press, Oxford, 2004.
- [21] A. Gnudi, D. Ventura, and G. Baccarani. One-Dimensional Simulation of a Bipolar Transistor by means of Spherical Harmonics Expansion of the Boltzmann Transport Equation. In *Proceedings of SISDEP*, volume 4, pages 205–213, 1991.
- [22] A. Gnudi, D. Ventura, and G. Baccarani. Modeling Impact Ionization in a BJT by Means of Spherical Harmonics Expansion of the Boltzmann Transport Equation. *IEEE Transactions on Computer-Aided Design of Integrated Circuits and Systems*, 12(11):1706–1713, 1993.
- [23] A. Gnudi, D. Ventura, G. Baccarani, and F. Odeh. Two-Dimensional MOSFET Simulation by Means of a Multidimensional Spherical Harmonics Expansion of the Boltzmann Transport Equation. *Solid-State Electronics*, 36(4):575–581, 1993.
- [24] N. Goldsman. *Modeling Electron Transport and Degradation Mechanisms in Semiconductor Submicron Devices*. PhD thesis, Cornell University, 1989.
- [25] N. Goldsman, L. Hendrickson, and J. Frey. A Physics-Based Analytical/Numerical Solution to the Boltzmann Transport Equation for the Use in Device Simulation. *Solid-State Electronics*, 34:389–396, 1991.
- [26] N. Goldsman, C.-K. Lin, Z. Han, and C.-K. Huang. Advances in the Spherical Harmonic–Boltzmann–Wigner Approach to Device Simulation. *Superlattices and Microstructures*, 27(2-3):159–175, 2000.
- [27] G. H. Golub and C. F. Van Loan. *Matrix Computations*. John Hopkins University Press, 1996.

- [28] L. Grafakos. *Classical-Fourier-Analysis*. Springer, 2008.
- [29] T. Grasser, H. Kosina, M. Gritsch, and S. Selberherr. Using Six Moments of Boltzmann's Transport Equation for Device Simulation. *Journal of Applied Physics*, 90(5):2389–2396, 2001.
- [30] T. Grasser, Tang T. W., H. Kosina, and S. Selberherr. A Review of Hydrodynamic and Energy-Transport Models for Semiconductor Device Simulation. *Proceedings of the IEEE*, 91(2):251–274, 2003.
- [31] H. Groemer. *Geometric Applications of Fourier Series and Spherical Harmonics*. Encyclopedia of Mathematics and its Applications. Cambridge University Press, Cambridge, 1996.
- [32] H.K. Gummel. A Self-Consistent Iterative Scheme for One-Dimensional Steady State Transistor Calculations. *IEEE Transactions on Electron Devices*, 11(10):455–465, 1964.
- [33] G. Haase, M. Liebmann, C. Douglas, and G. Plank. A Parallel Algebraic Multigrid Solver on Graphics Processing Units. In *High Performance Computing Applications*, volume 5938 of *LNCS*, pages 38–47. Springer, 2009.
- [34] R. N. Hall. Electron-Hole Recombination in Germanium. *Physical Review*, 87(2):387, 1952.
- [35] Z. Han, N. Goldsman, and C.-K. Lin. Incorporation of Quantum Corrections to Semi-classical Two-Dimensional Device Modeling with the Wigner–Boltzmann Equation. *Solid-State Electronics*, 49(2):145–154, 2005.
- [36] O. Hansen and A. Jüngel. Analysis of a Spherical Harmonics Expansion Model of Plasma Physics. *Mathematical Models and Methods in Applied Sciences*, 14:759–774, 2004.
- [37] K. A. Hennacy, N. Goldsman, and I. D. Mayergoyz. 2-Dimensional Solution to the Boltzmann Transport Equation to Arbitrarily High-Order Accuracy. In *Proceedings of IWCE*, pages 118–122, 1993.
- [38] K. A. Hennacy, Y. J. Wu, N. Goldsman, and I. D. Mayergoyz. Deterministic MOSFET Simulation Using a Generalized Spherical Harmonic Expansion of the Boltzmann Equation. *Solid-State Electronics*, 38(8):1485–1495, 1995.
- [39] J. S. Hesthaven and T. Warburton. *Nodal Discontinuous Galerkin Methods*. Springer, 2008.
- [40] V. Heuveline, D. Lukarski, and J. P. Weiss. Enhanced Parallel ILU(p)-based Preconditioners for Multi-core CPUs and GPUs – The Power(q)-pattern Method. EMCL Preprint 2011-08, EMCL, 2011.
- [41] E. W. Hobson. *The Theory of Spherical and Ellipsoidal Harmonics*. Cambridge University Press, 1955.

- [42] S.-M. Hong and C. Jungemann. A Fully Coupled Scheme for a Boltzmann-Poisson Equation Solver Based on a Spherical Harmonics Expansion. *Journal of Computational Electronics*, 8:225–241, 2009.
- [43] S.-M. Hong and C. Jungemann. Inclusion of the Pauli Principle in a Deterministic Boltzmann Equation Solver for Semiconductor Devices. In *Proceedings of SISPAD*, pages 135–138, 2010.
- [44] S.-M. Hong, C. Jungemann, and M. Bollhofer. A Deterministic Boltzmann Equation Solver for Two-Dimensional Semiconductor Devices. In *Proceedings of SISPAD*, pages 293–296, 2008.
- [45] S.-M. Hong, G. Matz, and C. Jungemann. A Deterministic Boltzmann Equation Solver Based on a Higher Order Spherical Harmonics Expansion With Full-Band Effects. *IEEE Transactions on Electron Devices*, 57(10):2390–2397, 2010.
- [46] S.-M. Hong, A.-T. Pham, and C. Jungemann. *Deterministic Solvers for the Boltzmann Transport Equation*. Springer, 2011.
- [47] C. Jacoboni and P. Lugli. *The Monte Carlo Method for Semiconductor Device Simulation*. Springer, 1989.
- [48] S. Jin, S.-M. Hong, and C. Jungemann. An Efficient Approach to Include Full-Band Effects in Deterministic Boltzmann Equation Solver Based on High-Order Spherical Harmonics Expansion. *IEEE Transactions on Electron Devices*, 58(5):1287–1294, 2011.
- [49] A. Jünger. *Quasi-hydrodynamic Semiconductor Equations*. Birkhäuser, 2001.
- [50] A. Jünger. *Transport Equations for Semiconductors*. Lecture Notes in Physics No. 773. Springer, Berlin, 2009.
- [51] C. Jungemann, T. Grasser, B. Neinhüs, and B. Meinerzhagen. Failure of Moments-Based Transport Models in Nanoscale Devices Near Equilibrium. *IEEE Transactions on Electron Devices*, 52:2404–2408, 2005.
- [52] C. Jungemann and B. Meinerzhagen. *Hierarchical Device Simulation*. Computational Microelectronics. Springer, 2003.
- [53] C. Jungemann, A.-T. Pham, B. Meinerzhagen, C. Ringhofer, and M. Bollhöfer. Stable Discretization of the Boltzmann Equation based on Spherical Harmonics, Box Integration, and a Maximum Entropy Dissipation Principle. *Journal of Applied Physics*, 100(2):024502, 2006.
- [54] C. Jungemann, S. Yamaguchi, and H. Goto. Investigation of the Influence of Impact Ionization Feedback on Spatial Distribution of Hot Carriers in an NMOSFET. In *Proceedings of ESSDERC*, pages 336–339, 1997.
- [55] E. O. Kane. Band Structure of Indium Antimonide. *Journal of Physics and Chemistry of Solids*, 1(4):249–261, 1957.

- [56] G. E. Karniadakis and S. Sherwin. *Spectral/hp Element Methods for Computational Fluid Dynamics*. Oxford University Press, 2005.
- [57] Khronos Group: OpenCL. <http://www.khronos.org/opencv/>.
- [58] Kitware Inc. ParaView. <http://www.paraview.org/>.
- [59] Kitware Inc. Visualization Toolkit (VTK). <http://www.vtk.org/>.
- [60] H. Kosina, M. Harrer, P. Vogl, and S. Selberherr. A Monte Carlo Transport Model Based on Spherical Harmonics Expansion of the Valence Bands. In *Proceedings of SISDEP*, pages 396–399, 1995.
- [61] T. Kurosawa. Monte Carlo Calculation of Hot Electron Problems. *Journal of the Physical Society of Japan*, 21:424–426, 1966.
- [62] P. W. Lagger. Scattering Operators for the Spherical Harmonics Expansion of the Boltzmann Transport Equation. Master’s thesis, Institute for Microelectronics, TU Wien, 2011.
- [63] S.-C. Lee and T.-W Tang. Transport Coefficients for a Silicon Hydrodynamic Model extracted from Inhomogeneous Monte-Carlo Calculations. *Solid-State Electronics*, 35(4):561 – 569, 1992.
- [64] R. J. LeVeque. *Finite Volume Methods for Hyperbolic Problems*. Cambridge University Press, 2002.
- [65] H. Lin, N. Goldsman, and I. D. Mayergoyz. Improved Self-Consistent Device Modeling by Direct Solution to Boltzmann and Poisson Equations. In *Proceedings of IWCE*, pages 143–146, 1992.
- [66] H. Lin, N. Goldsman, and I. D. Mayergoyz. Deterministic BJT Modeling by Self-Consistent Solution to the Boltzmann, Poisson and Hole-Continuity Equations. In *Proceedings of IWCE*, pages 55–59, 1993.
- [67] M. Lundstrom. *Fundamentals of Carrier Transport*. Cambridge University Press, 2000.
- [68] P. A. Markowich, C. A. Ringhofer, and C. Schmeiser. *Semiconductor Equations*. Springer, Wien, New York, 1990.
- [69] G. Matz, S.-M. Hong, and C. Jungemann. Spherical Harmonics Expansion of the Conduction Band for Deterministic Simulation of SiGe HBTs with Full Band Effects. In *Proceedings of SISPAD*, pages 167–170, 2010.
- [70] Nath, R. and Tomov, S. and Dongarra, J. An Improved MAGMA GEMM For Fermi Graphics Processing Units. *International Journal of High Performance Computing Applications*, 24(4):511–515, 2010.
- [71] A. Okabe, B. Boots, and K. Sugihara. *Spatial Tessellations: Concepts and Applications of Voronoi Diagrams*. Wiley, 1992.

- [72] V. Peikert and A. Schenk. A Wavelet Method to Solve High-dimensional Transport Equations in Semiconductor Devices. In *Proceedings of SISPAD*, pages 299–302, 2011.
- [73] A.-T. Pham, C. Jungemann, and B. Meinerzhagen. A Full-Band Spherical Harmonics Expansion of the Valence Bands up to High Energies. In *Proceedings of SISPAD*, pages 361–364, 2006.
- [74] A.-T. Pham, C. Jungemann, and B. Meinerzhagen. Deterministic Multisubband Device Simulations for Strained Double Gate PMOSFETs including Magnetotransport. In *IEDM 2008*, pages 1–4, 2008.
- [75] A.-T. Pham, C. Jungemann, and B. Meinerzhagen. A Convergence Enhancement Method for Deterministic Multisubband Device Simulations of Double Gate PMOSFET. In *Proceedings of SISPAD*, pages 115–118, 2009.
- [76] A.-T. Pham, C. Jungemann, and B. Meinerzhagen. On the Numerical Aspects of Deterministic Multisubband Device Simulations for Strained Double Gate PMOSFETs. *Journal of Computational Electronics*, 8:242–266, 2009.
- [77] A. Pierantoni, A. Gnudi, and G. Baccarani. Hot-electron Injection in MOS Devices by Means of the Spherical Harmonics Expansion of the Boltzmann Equation. In *Proceeding of ESSDERC*, pages 320–323, 1998.
- [78] K. Rahmat, J. White, and D. A. Antoniadis. Simulation of Semiconductor Devices Using a Galerkin/Spherical Harmonic Expansion Approach to Solving the Coupled Poisson-Boltzmann System. *IEEE Transactions on Computer-Aided Design of Integrated Circuits and Systems*, 15(10):1181–1195, 1996.
- [79] S. E. Rauch, G. La Rosa, and F. J. Guarin. Role of E-E Scattering in the Enhancement of Channel Hot Carrier Degradation of Deep-Submicron NMOSFETs at High VGS Conditions. *IEEE Transactions on Device and Materials Reliability*, 1(2):113–119, 2001.
- [80] C. Ringhofer. Space-Time Discretization of Series Expansion Methods for the Boltzmann Transport Equation. *SIAM Journal of Numerical Analysis*, 38(2):442–465, 2000.
- [81] C. Ringhofer. Dissipative Discretization Methods for Approximations to the Boltzmann Equation. *Mathematical Models and Methods in Applied Sciences*, 11:133–149, 2001.
- [82] C. Ringhofer. Numerical Methods for the Semiconductor Boltzmann Equation Based on Spherical Harmonics Expansions and Entropy Discretizations. *Transport Theory and Statistical Physics*, 31:431–452, 2002.
- [83] C. Ringhofer. A Mixed Spectral-Difference Method for the Steady State Boltzmann-Poisson System. *SIAM Journal of Numerical Analysis*, 41(1):64–89, 2003.
- [84] C. Ringhofer, C. Schmeiser, and A. Zwirchmayr. Moment Methods for the Semiconductor Boltzmann Equation on Bounded Position Domains. *SIAM Journal of Numerical Analysis*, 39(3):1078–1095, 2001.

- [85] B. Rivière. *Discontinuous Galerkin Methods for Solving Elliptic and Parabolic Equations*. SIAM, 2008.
- [86] K. Rupp. Numerical Solution of the Boltzmann Transport Equation using Spherical Harmonics Expansions. Master's thesis, Institute for Analysis and Scientific Computing, TU Wien, 2009.
- [87] K. Rupp, A. Jüngel, and T. Grasser. Matrix Compression for Spherical Harmonics Expansions of the Boltzmann Transport Equation for Semiconductors. *Journal of Computational Physics*, 229(23):8750–8765, 2010.
- [88] Y. Saad. *Iterative Methods for Sparse Linear Systems, Second Edition*. SIAM, 2003.
- [89] Y. Saad and M. H. Schultz. GMRES: A Generalized Minimal Residual Algorithm for Solving Nonsymmetric Linear Systems. *SIAM Journal on Scientific and Statistical Computing*, 7(3):856–869, 1986.
- [90] D. L. Scharfetter and H. K. Gummel. Large-Signal Analysis of a Silicon Read Diode Oscillator. *IEEE Transactions on Electron Devices*, 16:64–77, 1969.
- [91] J. Schöberl. Netgen Mesh Generator. <http://sourceforge.net/projects/netgen-mesher/>.
- [92] D. Schroeder, D. Ventura, A. Gnudi, and G. Baccarani. Boundary Conditions for Spherical Harmonics Expansion of Boltzmann Equation. *Electronics Letters*, 28(11):995–996, 1992.
- [93] S. Selberherr. *Analysis and Simulation of Semiconductor Devices*. Springer, 1984.
- [94] J. R. Shewchuk. *Delaunay Refinement Mesh Generation*. PhD thesis, School of Computer Science, Carnegie Mellon University, 1997.
- [95] W. Shockley and W. T. Read. Statistics of the Recombinations of Holes and Electrons. *Physical Review*, 87(5):835–842, 1952.
- [96] J. Singh. *Electronic and Optoelectronic Properties of Semiconductor Structures*. Cambridge University Press, 2003.
- [97] S. P. Singh. *Modeling Multi-Band Effects of Hot-Electron Transport in Simulation of Small Silicon Devices by a Deterministic Solution of the Boltzmann Transport Equation Using Spherical Harmonic Expansion*. PhD thesis, Department of Electrical Engineering, University of Maryland, 1998.
- [98] K. Sonoda, M. Yamaji, K. Taniguchi, C. Hamaguchi, and S. T. Dunham. Moment Expansion Approach to Calculate Impact Ionization Rate in Submicron Silicon Devices. *Journal of Applied Physics*, 80(9):5444–5448, 1996.
- [99] K. Tomizawa. *Numerical Simulation of Submicron Semiconductor Devices*. Artech House Inc, 1993.
- [100] U. Trottenberg, C. W. Oosterlee, and A. Schuller. *Multigrid*. Academic Press, 2000.

- [101] S.E. Tyaginov, I.A. Starkov, O. Triebel, J. Cervenka, C. Jungemann, S. Carniello, J.M. Park, H. Enichlmair, M. Karner, C. Kernstock, E. Seebacher, R. Minixhofer, H. Ceric, and T. Grasser. Hot-carrier Degradation Modeling Using Full-Band Monte-Carlo Simulations. In *Proceedings of IPFA*, pages 1–5, 2010.
- [102] H. A. van der Vorst. Bi-CGSTAB: A Fast and Smoothly Converging Variant of Bi-CG for the Solution of Non-Symmetric Linear Systems. *SIAM Journal on Scientific and Statistical Computing*, 12:631–644, 1992.
- [103] W. V. Van Roosbroeck. Theory of Flow of Electrons and Holes in Germanium and other Semiconductors. *Bell System Technical Journal*, 29:560–607, 1950.
- [104] P. S. Vassilevski. *Multilevel Block Factorization Preconditioners*. Springer, 2008.
- [105] M. C. Vecchi, J. Mohring, and M. Rudan. An Efficient Solution Scheme for the Spherical-Harmonics Expansion of the Boltzmann Transport Equation. *IEEE Transactions on Computer-Aided Design of Integrated Circuits and Systems*, 16(4):353–361, 1997.
- [106] M. C. Vecchi and M. Rudan. Modeling Electron and Hole Transport with Full-Band Structure Effects by Means of the Spherical-Harmonics Expansion of the BTE. *IEEE Transactions on Electron Devices*, 45:230–238, 1998.
- [107] M. C. Vecchi, D. Ventura, A. Gnudi, and G. Baccarani. Incorporating Full Band-Structure Effects in the Spherical Harmonics Expansion of the Boltzmann Transport Equation. In *Proceedings of NUPAD*, pages 55–58, 1994.
- [108] A. Ventura, D. Gnudi, , and G. Baccarani. Inclusion of Electron-Electron Scattering in the Spherical Harmonics Expansion Treatment of the Boltzmann Transport Equation. In *Proceedings of SISDEP*, pages 161–164, 1993.
- [109] D. Ventura, A. Gnudi, and G. Baccarani. A Deterministic Approach to the Solution of the BTE in Semiconductors. *La Rivista del Nuovo Cimento*, 18:1–33, 1995.
- [110] D. Ventura, A. Gnudi, G. Baccarani, and F. Odeh. Multidimensional Spherical Harmonics Expansion of Boltzmann Equation for Transport in Semiconductors. *Applied Mathematics Letters*, 5(3):85–90, 1992.
- [111] Vienna Computing Library (ViennaCL). <http://viennacl.sourceforge.net/>.
- [112] H. F. Walker and L. Zhou. A Simpler GMRES. *Numerical Linear Algebra with Applications*, 1(6):571–581, 1994.
- [113] W. Wessner. *Mesh Refinement Techniques for TCAD Tools*. PhD thesis, Institute for Microelectronics, TU Wien, 2006.
- [114] W. Zhang, G. Du, Q. Li, A. Zhang, Z. Mo, X. Liu, and P. Zhang. A 3D Parallel Monte Carlo Simulator for Semiconductor Devices. In *Proceedings of IWCE*, pages 1–4, 2009.

Own Publications

Journal Articles

- [1] K. Rupp, A. Jüngel, and T. Grasser. Matrix Compression for Spherical Harmonics Expansions of the Boltzmann Transport Equation for Semiconductors. *Journal of Computational Physics*, 229(23):8750–8765, 2010.
- [2] K. Rupp and S. Selberherr. The Economic Limit to Moore’s Law. *Proceedings of the IEEE*, 98(3):351–353, 2010.
- [3] K. Rupp and S. Selberherr. The Economic Limit to Moore’s Law. *IEEE Transactions on Semiconductor Manufacturing*, 24(1):1–4, 2011.

Contributions to Books

- [1] K. Rupp, A. Jüngel, and T. Grasser. Matrix Compression for Spherical Harmonics Expansions of the Boltzmann Transport Equation for Semiconductors. *ASC Report 10/2010*, pages 1–32, 2010.

Conference Contributions

- [1] K. Rupp, T. Grasser, and A. Jüngel. A Matrix Compression Scheme for Spherical Harmonics Expansions of the Boltzmann Transport Equation. In *Proceedings of the Junior Scientist Conference 2010*, pages 7–8, 2010.
- [2] K. Rupp. Increased Efficiency in Finite Element Computations through Template Metaprogramming. In *Proceedings of the Spring Simulation Multiconference 2010*, pages 135–142, 2010.
- [3] J. Weinbub, K. Rupp, and S. Selberherr. ViennaIPD - An Input Control Language for Scientific Computing. In *Proceedings of the Industrial Simulation Conference*, pages 34–38, 2010.
- [4] K. Rupp and H. Ceric. Analytical and Numerical Investigation of the Segregation Problem. In *4th International Conference Computational Methods in Applied Mathematics (CMAM-4)*, 2010.
- [5] K. Rupp, T. Grasser, and A. Jüngel. Deterministic Numerical Solution of the Boltzmann Transport Equation. In *Progress in Industrial Mathematics at ECMI 2010*, 2012. To appear.

-
- [6] K. Rupp. Symbolic Integration at Compile Time in Finite Element Methods. In *Proceedings of the 2010 International Symposium on Symbolic and Algebraic Computation*, pages 347–354, 2010.
- [7] K. Rupp, T. Grasser, and A. Jüngel. System Matrix Compression for Spherical Harmonics Expansions of the Boltzmann Transport Equation. In *Proceedings of the 15th International Conference on Simulation of Semiconductor Processes and Devices*, pages 159–162, 2010.
- [8] K. Rupp, F. Rudolf, and J. Weinbub. ViennaCL - A High Level Linear Algebra Library for GPUs and Multi-Core CPUs. In *Intl. Workshop on GPUs and Scientific Applications*, pages 51–56, 2010.
- [9] K. Rupp, J. Weinbub, and F. Rudolf. Automatic Performance Optimization in ViennaCL for GPUs. In *Proceedings of the 9th Workshop on Parallel/High-Performance Object-Oriented Scientific Computing*, pages 6:1–6:6, 2010.
- [10] K. Rupp. Deterministic Numerical Solution of the Boltzmann Transport Equation. In *Proceedings of the Austrian-Chinese Workshop on Dissipative Systems: Kinetic Theory and Semiconductor Applications*, pages 7–8, 2010.
- [11] J. Weinbub, K. Rupp, and S. Selberherr. Distributed Heterogenous High-Performance Computing with ViennaCL. In *Abstracts Intl. Conf. on Large-Scale Scientific Computations*, pages 88–90, 2011.
- [12] J. Weinbub, J. Cervenka, K. Rupp, and S. Selberherr. A Generic High-Quality Meshing Framework. In *Proceedings of the 11th US National Congress on Computational Mechanics*, 2011.
- [13] J. Weinbub, J. Cervenka, K. Rupp, and S. Selberherr. High-Quality Mesh Generation Based on Orthogonal Software Modules. In *Proceedings of the 16th International Conference on Simulation of Semiconductor Processes and Devices*, pages 139–142, 2011.
- [14] K. Rupp, T. Grasser, and A. Jüngel. Parallel Preconditioning for Spherical Harmonics Expansions of the Boltzmann Transport Equation. In *Proceedings of the 16th International Conference on Simulation of Semiconductor Processes and Devices*, pages 147–150, 2011.
- [15] K. Rupp, T. Grasser, and A. Jüngel. Adaptive Variable-Order Spherical Harmonics Expansion of the Boltzmann Transport Equation. In *Proceedings of the 16th International Conference on Simulation of Semiconductor Processes and Devices*, pages 151–155, 2011.
- [16] K. Rupp, A. Jüngel, and T. Grasser. A GPU-Accelerated Parallel Preconditioner for the Solution of the Boltzmann Transport Equation for Semiconductors. In *Proceedings of Facing the Multicore-Challenge II*, 2011.
- [17] K. Rupp, T. Grasser, and A. Jüngel. On the Feasibility of Spherical Harmonics Expansions of the Boltzmann Transport Equation for Three-Dimensional Device Geometries. In *IEDM Technical Digest*, 2011.

Software

- [1] Vienna Computing Library (ViennaCL). <http://viennacl.sourceforge.net/>.
- [2] ViennaData Library. <http://viennadata.sourceforge.net/>.
- [3] ViennaGrid Library. <http://viennagrid.sourceforge.net/>.
- [4] ViennaSHE Device Simulator. <http://viennashe.sourceforge.net/>.

Curriculum Vitae

1984

- Born on June 12th in Bad Radkersburg, Austria.

2001

- Fourth price at the *Austrian-Polish Math Competition (ÖPMW)*.

2002

- Winner of the *Steirischer Landeswettbewerb* (Styrian regional competition) of the *Österreichische Physik Olympiade* (Austrian Physics Olympiad).
- Winner of the *Gebietswettbewerb* (qualification competition for advanced students) of the *Österreichische Mathematik Olympiade* (Austrian Mathematical Olympiad).
- Ranked 5th at the *Bundeswettbewerb* (federal competition for advanced students) of the *Österreichische Mathematik Olympiade*.
- Winner of the *Känguru der Mathematik* (Austrian Kangaroo Math Competition).
- High school graduation (*Matura*) at the BG/BRG Leibnitz (with distinction).
- Honourable Mention at the *International Mathematical Olympiad* in Glasgow.
- Start of compulsory military service.

2003

- Completed military service.
- Enrolled *Technische Mathematik* (technical mathematics) and *Elektrotechnik* (electrical engineering) at TU Wien.

2006

- Received Bachelor degree in *Elektrotechnik* from TU Wien (with distinction).
- Enrolled *Computational Mathematics with Modelling* at Brunel University, West London, UK.
- Awarded *Leistungsstipendium* (distinguished fellowship) from the *Fakultät für Elektrotechnik und Informationstechnik*, TU Wien.

2007

- Received Master (MSc.) degree in *Computational Mathematics with Modelling* from Brunel University, West London, UK (with distinction).
- Enrolled *Mikroelektronik* (microelectronics) Master's course at TU Wien.

2008

- Awarded *Leistungsstipendium* (distinguished fellowship) from the *Fakultät für Elektrotechnik und Informationstechnik*, TU Wien.

2009

- Entered doctoral program at the Institute for Microelectronics, TU Wien.
- Received degree of *Diplomingenieur* in *Mikroelektronik* from TU Wien (with distinction).
- Award from the City of Vienna for an excellent master's thesis at TU Wien.
- Received degree of *Diplomingenieur* in *Technische Mathematik* from TU Wien (with distinction).

2010

- Entered doctoral program at the Institute for Analysis and Scientific Computing, TU Wien.

2011

- Initiator and head of the *Computational Science and Engineering at TU Wien* project at the Google Summer of Code 2011.